PHYSICS-AIDED DATA-DRIVEN UNDERWATER ACOUSTIC PROPAGATION MODELING

LI KEXIN

(B.Eng.(Hons), NUS)

A THESIS SUBMITTED FOR THE DEGREE OF DOCTOR OF PHILOSOPHY

DEPARTMENT OF ELECTRICAL AND COMPUTER ENGINEERING

NATIONAL UNIVERSITY OF SINGAPORE

2022

Supervisor:
Associate Professor Mandar Chitre

Examiners:
Associate Professor Arthur Tay Ee Beng
Associate Professor Abdullah Al Mamun

DECLARATION

I hereby declare that this thesis is my original work and it has been written by me in its entirety. I have duly acknowledged all the sources of information which have been used in the thesis.

This thesis has also not been submitted for any degree in any university previously.

Li Kexin

8th August 2022

ACKNOWLEDGEMENTS

This thesis would not be possible without the kind help of many wonderful people. I would like to take this opportunity to express my sincere gratitude to them in this acknowledgment.

First and foremost, words cannot convey my immense gratitude to my thesis advisor, A/Prof. Mandar Chitre, for his support, guidance, encouragement, patience and empathy. I am so proud of and incredibly grateful to have the opportunity to work with such a knowledgable and professional researcher. He is not only my academic mentor, but also a true friend. I am not able to go through this journey without him.

I would like to thank my amazing colleagues at ARL* for their kind support and valuable advice on my research work. It is my great pleasure to work at such a lovely research lab. Special thanks go to my seniors in ARL: Dr. Too Yuen Min, Dr. Hari Vishnu, Dr. Bharath Kalyan, Dr. Gabriel Chua, Dr. Rajat Mishra and Dr. Gao Rui for their precious advice. I would like to thank my peers: Ms. Wu Shuangshuang and Ms. Peng Luyuan who always accompany and encourage me throughout my study. The assistance provided by Mr. Alex Kee is greatly appreciated. I want to thank Ms. Ong Lee Lin for her help in my academic writing. I would also like to thank A/Prof. Abdullah Al Mamun and A/Prof. Arthur Tay for providing valuable feedback on my research proposal and thesis during the qualification examination and oral examination.

Very special thanks go to my major project supervisor Mr. Lim Hock

---

Contents

Abstract

___

Electromagnetic waves suffer from severe attenuations in water. Acoustics is the most feasible alternative for reliable underwater sensing and communication. Rich multipath propagation in underwater environments leads to complicated interference patterns, making underwater environments acoustically complicated. The ability to effectively model acoustic propagation is vital for numerous underwater applications, such as underwater source localization for search & rescue, path planning for autonomous underwater vehicles, remote sensing of underwater environments and underwater communication channel estimation. Implementing such underwater applications using conventional acoustic propagation models is theoretically feasible, but practically challenging.

Conventional propagation models numerically solve the acoustic wave equation with various simplifying approximations. They require full and accurate environmental knowledge beforehand. Environmental parameters, such as bathymetry, sound speed profile and boundary conditions, may not always be easily or accurately measurable. Modeling underwater acoustic propagation under partial environmental knowledge is inevitable in practice, but cannot be addressed by conventional models. While classical data-driven machine learning (ML) techniques allow us to predict acoustic fields from data, they are data-hungry and lack extrapolability and interpretability. Large-scale

iv

acoustic data acquisition in underwater environments is difficult and expensive. Developing data-driven models that are trained to learn from scientific data while respecting certain constraints informed by domain knowledge yields an emerging technique called *scientific machine learning* (SciML). SciML leverages complementary strengths of underlying physics and data-driven ML to tackle a wide range of engineering and scientific problems.

Motivated by the idea of SciML, this thesis focuses on developing a hybrid underwater acoustic propagation modeling recipe that not only learns from data, but also utilizes the physics of underwater acoustic propagation. We design a class of ML algorithms that the physics of acoustic propagation is encoded in the structures of the algorithms. The functions these algorithms learn are automatically solutions to the acoustic wave equation. We give up the universal approximation property of neural networks, and constrain our algorithms to only learn physically realistic functions instead. The underlying physical constraint not only enables a data-efficient model, but also offers flexibilities to combine classical ML models and incorporate varying degrees of environmental knowledge, brings interpretability to trained model parameters and generalizes well to permit extrapolation beyond the area where data are collected. We illustrate the proposed modeling recipe based on the ray theory and the normal mode theory. We demonstrate the flexibility and superiority of the proposed modeling frameworks through various numerical case studies while benchmarking against classical data-driven ML techniques. We also show their applicability in solving practical problems that cannot be handled by state-of-the-art modeling techniques through a real-world controlled experiment.

List of Tables

List of Figures

viii

List of Abbreviations

TPL	Towed Pinger Locator
AUV	Autonomous Underwater Vehicle
MFP	Matched Field Processing
SSP	Sound Speed Profile
ML	Machine Learning
GPR	Gaussian Process Regression
NN	Neural Network
DNN	Deep Neural Network
TOA	Time of Arrival
TDOA	Time Difference of Arrival
RMSE	Root Mean Square Error
MAE	Mean Absolute Error
MATE	Mean Absolute Test Error
dB	Decibel
Pa	Pascal
μPa	Micropascal
CTD	Conductivity-Temperature-Depth
SciML	Scientific Machine Learning
PINN	Physics-Informed Neural Network
PDE	Partial Differential Equation
CW	Continuous Wave
AOI	Area Of Interest
RBNN	Ray Basis Neural Network
RCNN	Reflection Coefficient Neural Network
ISM	Image Source Method
ReLU	Rectified Linear Unit
NI-DAQ	National Instruments Data Acquisition
AOM	Area of Measurement
MBNN	Mode Basis Neural Network
WKB	Wentzel–Kramers–Brillouin
SSNN	Sound Speed Neural Network

List of Symbols and Notations

$\boldsymbol{r}_\mathrm{s}$	Source location
i	Time step
$\boldsymbol{r}$	Measurement location
y	Measured field
$\mathcal{Z}_i$	A collection of measured information up to step i
$\boldsymbol{\tau}$	Uncertain environmental parameter sets
η	Convergence threshold of source location entropy
$\mathcal{A}(\boldsymbol{r})$	All feasible moves at location $\boldsymbol{r}$
$M(\boldsymbol{\tau}, \boldsymbol{r}, \boldsymbol{r}_\mathrm{s})$	Modeled replica field at location $\boldsymbol{r}$ using environmental parameters $\boldsymbol{\tau}$
$\bar{M}(\boldsymbol{r}_\mathrm{s}, \mathcal{Z}, \boldsymbol{r})$	Expected modeled replica field at location $\boldsymbol{r}$ over all candidate environmental parameter sets
$\mu(\mathcal{Z}, \boldsymbol{r})$	Expected modeled replica field at location $\boldsymbol{r}$ over all candidate environmental parameter sets and source locations
I	Intensity
λ	Wavelength
f	Frequency
c	Sound speed
ω	Angular velocity
p	Pressure
$\bar{p}(\boldsymbol{r})$	Complex pressure amplitude at location $\boldsymbol{r}$
$\hat{p}(\boldsymbol{r})$	Absolute pressure amplitude at location $\boldsymbol{r}$
k	Wavenumber
$\boldsymbol{k}$	Wave propagation vector
A	Amplitude of a ray
ϕ	Phase of a ray
θ	Azimuthal angle
ψ	Elevation angle
$\bar{d}(\boldsymbol{r}_\mathrm{s}, \boldsymbol{r})$	Euclidean distance between $\boldsymbol{r}_\mathrm{s}$ and $\boldsymbol{r}$
$\boldsymbol{r}_o$	Reference location
$\boldsymbol{s}$	Image source location
d	Distance between $\boldsymbol{s}$ and $\boldsymbol{r}_o$ of a ray
L	Loss function
n_ray	Number of arrival rays

n_{b}	Number of bottom reflections
n_{s}	Number of surface reflections
θ'	Nominal azimuthal angle
ψ'	Nominal elevation angle
d'	Nominal distance
e_{θ}	Error to pre-calculated θ'
e_{ψ}	Error to pre-calculated ψ'
e_d	Error to pre-calculated d'
$\boldsymbol{r}_{\mathrm{train}}$	Measurement locations in training dataset
$\boldsymbol{y}_{\mathrm{train}}$	Acoustic measurements in training dataset
α	Regularization coefficient of arrival ray amplitude
$\boldsymbol{\zeta}$	Penalty coefficient of angular error
β	Penalty coefficient of distance error
χ	Penalty coefficient of reflection energy
$\mathcal{T}$	Trainable parameters in the proposed frameworks
$\mathcal{T}^*$	Optimal trainable parameters in the proposed frameworks
$\boldsymbol{R}$	Trainable parameters in RCNN model
ϵ	Reflection coefficient
κ	Reflection phase shift
γ	Incident angle of a reflection
Γ	Complex reflection coefficient
l_{a}	Volume absorption loss term
l_{rc}	Reflection loss term
l_{g}	Geometric spreading loss term
$\mathcal{A}'$	Full action space in localization validation experiment
$\boldsymbol{r}'$	Corrected measurement location
$\boldsymbol{r}_{\mathrm{error}}$	Trained location error
r	Range
z	Depth
D	Water depth
$\boldsymbol{S}$	Trainable parameters in SSNN model
k_{r}	Horizontal wavenumber
k_{z}	Vertical wavenumber
n_{mode}	Number of contributing modes considered
$\Psi(z)$	Vertical term in normal mode theory
$\Phi(r)$	Horizontal term in normal mode theory
$\bar{A}$	Amplitude of downward $\Psi(z)$

$\bar{B}$	Amplitude of upward $\Psi(z)$
$\bar{\alpha}$	Regularization coefficient of $\bar{\boldsymbol{A}}$
$\bar{\beta}$	Regularization coefficient of $\bar{\boldsymbol{B}}$

Notation: Bold symbols and $[\cdot]$ denote vectors. Symbols in calligraphic font and $(\cdot)$ represent tuples. Sets are written as $\{\cdot\}$. We use the interval notation: $[a,b) = \{x \in \mathbb{R} | a \leqslant x < b\}$. $|c|$ denotes the magnitude of a complex number c. For vectors $\boldsymbol{a}$ and $\boldsymbol{b}$, $\boldsymbol{a} \cdot \boldsymbol{b}$ is the dot product. $\|\boldsymbol{a}\|_1$ and $\|\boldsymbol{a}\|_2$ denote L_1-norm and L_2-norm of vector $\boldsymbol{a}$ respectively. The symbol $\equiv$ denotes equivalence, and the symbol ∇^2 is the Laplace operator.

List of Publications

Publications arising out of the thesis:

1. K. Li and M. Chitre, "Informative path planning for source localization," in *ICRA Workshop on Sound Source Localization and Its Applications for Robots*, Montreal, Canada, pp. 1-3, 2019.

2. K. Li and M. Chitre, "Informative path planning for acoustic source localization with environmental uncertainties," in *MTS/IEEE OCEANS*, Singapore-US Gulf Coast, pp. 1-5, 2020.

3. K. Li and M. Chitre, "Ocean acoustic propagation modeling using scientific machine learning" in *MTS/IEEE OCEANS*, San Diego-Porto, pp. 1-5, 2021.

4. K. Li and M. Chitre, "Physics-aided data-driven modal ocean acoustic propagation modeling," in *24th International Congress of Acoustics*, Gyeongju, Korea, pp. 1-9, 2022.

5. K. Li and M. Chitre, "Data-aided underwater acoustic ray propagation modeling," in *IEEE Journal of Oceanic Engineering.* (submitted)

Other related publication:

1. M. Chitre and K. Li, "Physics-informed data-driven communication performance prediction for underwater vehicles," in *Underwater Communications and Networking (Ucomms)*, Lerici, Italy, pp. 1-5, 2022.

Chapter 1

Introduction

1.1 Motivation

Despite the fact that water covers approximately 71% of the Earth's surface, our understanding of what happens beneath the water surface remains limited. A variety of underwater activities, such as ocean exploration [1], surveillance [2], search & rescue [3], geological survey [4] and environmental monitoring [5], have emerged in recent decades. All these require reliable underwater communication. Electromagnetic waves are severely attenuated in underwater environments due to the high permittivity and conductivity of water [6]. Acoustics is a feasible alternative for reliable underwater communication. The ability to effectively model underwater acoustic propagation is vital in many underwater applications, and therefore necessary although often challenging. In a typical underwater environment, acoustic propagation exhibits strong spatial variability. Multipath structure leads to complicated constructive and destructive interference patterns, with details that are strongly dependent on environmental parameters. Given detailed knowledge of an acoustic source and an underwater environment, many popular ocean acoustic propagation models are able to predict spatial variability of the acoustic fields in oceans [7]. Fig. 1.1 shows a complicated acoustic interference pattern in a typical ocean waveguide generated by Bellhop
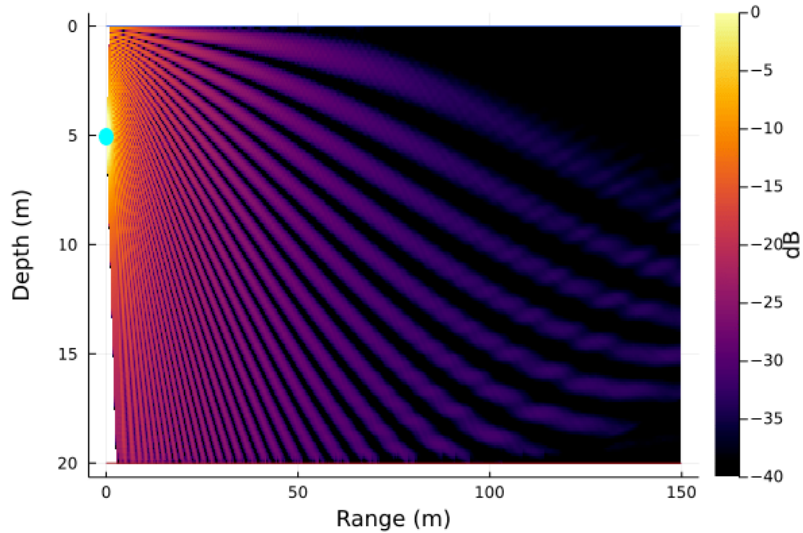
Figure 1.1: An example of acoustic field interference pattern in a non-isovelocity two-dimensional (2D) ocean environment due to a 5 kHz acoustic source. The source location is labelled as the coral blue dot.

propagation model [8].

1.1.1 Applications of acoustic propagation models

Applications related to acoustic propagation modeling in underwater environments can be broadly categorized into two main classes: *forward* problems and *inverse* problems. The forward problems seek to estimate the acoustic fields at various receiver locations assuming all required environmental parameters are known [9]–[11]. On the other hand, inferring unknown environmental parameters from acoustic measurements is of interest to the inverse problems [12]–[15]. Common inverse problems mainly focus on source localization and remote sensing of ocean environments [16].

For example, a deep ocean search for an aircraft black box is a typical inverse problem associated with underwater source localization. Consider a black box search task for Malaysia Airlines Flight 370 (MH370) which crashed

into the Indian Ocean in 2014. A saltwater-activated pinger mounted on the aircraft black box transmits acoustic pings at 37.5 kHz periodically for a month, after which the black box would lie on the seabed silently. Therefore, timely and accurate localization of the black box is extremely important for airplane crash investigations. A state-of-the-art black box retrieval strategy employs a two-phase search scheme [17]. The initial phase surveys the bathymetry in a search space using surface vessels with multi-beam sonars to understand the detailed seabed terrain. This is to ensure underwater search devices (e.g., towed pinger locator (TPL), tow-fish or autonomous underwater vehicle (AUV) with multi-beam sonars and side-scan sonars) can operate effectively and safely. Guided by the surveyed bathymetry, the search area is then divided into subdomains in the second phase and the search devices are deployed to sweep through each subdomain to listen for the pinger. Once the ping is detected, resources are focused on searching in the direction where the measured acoustic intensity increases. Fig. 1.2 illustrates a typical setup that US Navy used to search for the MH370 black box. However, the conventional search strategy that deploys sizable surface vessels to tow the search devices incurs high operational costs and furthermore a lot of time may be expended, especially if the search area is immense*.

A few possible pings in the same vicinity were reported during the initial search. Unfortunately, the investigators were unsuccessful in locating the black box until all search systems stopped detecting any acoustic pings a few days later [17]. Eight years on, MH370 is still an unsolved mystery. The pings

---

*The primary search area of the MH370 was about 60,000 km^2 and the deepest part was approximately 6,000 m [17].
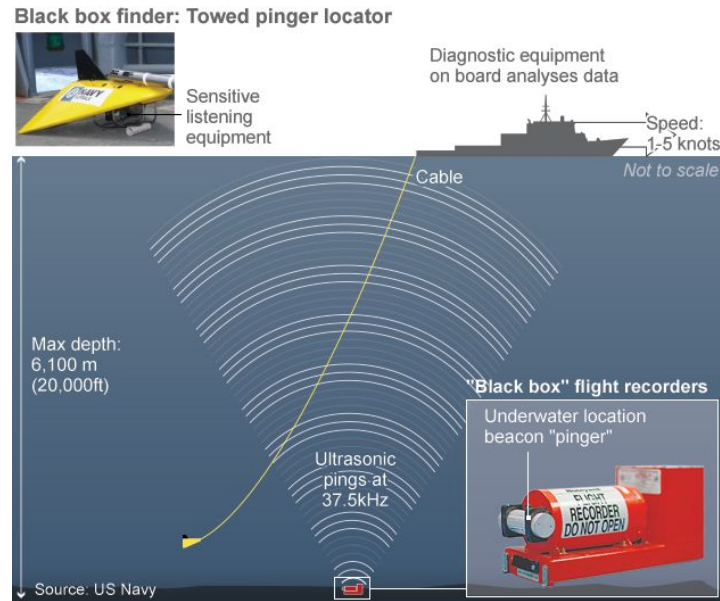
Figure 1.2: A state-of-the-art setup used in MH370 deep sea black box search by US Navy [18].

detected over that few days might be the closest moments to the truth. Why is it so hard to locate the black box even though pings are already detected? As shown in Fig. 1.1, the ocean is a rich multipath environment, leading to complicated interference patterns. A location with weak signal strength does not necessarily mean it is further away from the source than a location with strong signal strength. Searching the source based on the received signal strength in such an acoustically complicated environment is not effective.

If we have an underwater propagation model that can accurately model the multipath acoustic propagation of the signal from the black box in the search area, a few measurements at different locations may be sufficient to locate the black box once pings are detected. This basic idea has been explored in matched field processing (MFP) [19]. We can reduce implementation complexity and cost in subdomain searches by using AUVs, each fitted with a low-fidelity acoustic

sensor. In this way, we can deploy multiple AUVs to survey the subdomains concurrently and avoid the use of several surface vessels to tow the devices. Once the pings worth investigating have been detected, the AUV can adaptively plan its path to maximize information gain of the pinger location by incorporating the measurement history. This ensures that we can effectively locate the black box using the MFP within the shortest possible time.

Additionally, the multiple AUVs deployed for subdomain searches need to communicate with a master surface vessel, so that personnel on board the vessel can analyze the measured data and send commands in real time. However, the received acoustic intensities exhibit significant spatial fluctuations in underwater environments. The communication and navigation performance of a moving AUV through acoustics is highly variable and strongly depends on its spatial location with respect to the master vessel. If the environment is well understood, we can use conventional propagation models to predict AUV's nearby acoustic field patterns while it executing the mission. The AUV can then plan its path to maintain reliable navigation and communication performance with the master vessel throughout the mission. This is a typical forward problem that uses acoustic propagation models to predict acoustic fields for path planning given environmental knowledge.

Remote sensing of underwater environments, also called geo-acoustic inversion in literature, is a popular inverse problem. Characterizing geo-acoustic parameters, such as physical properties of seafloors, through direct measurements is often hard and infeasible in practice. Geo-acoustic inversion techniques estimate environmental characteristics through acoustic field data with the aid of

acoustic propagation models [20]. Geo-acoustic inversions are potentially faster and less expensive than direct measurements without disturbing geo-acoustic properties [21]. Moreover, effectively estimating channel state information in underwater environments is a key step in underwater communication system design and validation. This is a typical forward problem and can be readily done using acoustic propagation models if environments are well understood [22].

1.1.2 Limitations of conventional propagation models

Underwater acoustic propagation models play a key role in many underwater applications, including but not limited to the aforementioned applications. Conventional models require accurate environmental knowledge to make good predictions of acoustic fields. Accurate measurements of environmental parameters, such as sediment properties, sound speed profile (SSP), bathymetry, internal waves, suspended bubbles, may be difficult or expensive in practice. Even in cases where such information is available, it may not always be straightforward to incorporate the knowledge into models. In addition, there are two more limitations of conventional models–high computational complexity for three-dimensional (3D) underwater environments and poor generalization for confined water environments, such as tanks, pools, estuaries and artificial lakes. The limitations of conventional propagation models make numerous underwater applications that heavily rely on acoustic propagation models practically infeasible.

1.1.3 Data-driven alternatives

The availability of datasets has driven rapid growth in the development of data-driven machine learning (ML) algorithms over the past years [23]. ML algorithms allow computers to automatically learn from data and perform certain tasks that were previously considered difficult [24]. Although accurately measuring all environmental parameters required by conventional models can be hard and costly, collecting a small number of acoustic measurements may not be. A mobile underwater platform, such as an AUV or a profiling float, equipped with a low-fidelity acoustic transducer can do the job. Many underwater applications benefit from the use of ML [25]. For example, acoustic fields may be modeled using classical data-driven ML techniques such as Gaussian process regression (GPR) [26] or deep neural networks (DNN) [27], assuming sufficient training data and network capacity are provided. Since data-driven approaches only require acoustic measurements for training, they eliminate the need of having full and accurate prior environmental knowledge, and can work in any underwater environment. However, two key problems that limit their use in acoustic propagation modeling are the necessity of a large training dataset, and the inability to extrapolate well [28]. The cost of large-scale acoustic data acquisition is inevitably high, as underwater environments are expensive to operate in.

1.1.4 Research question

Conventional acoustic propagation models solve the acoustic wave equation [29] with approximations. They do not need training data, but require accurate

environmental knowledge. Predicting acoustic fields through the data-driven ML techniques eliminates the necessity of having prior environmental knowledge at the cost of using extensive acoustic data. This dichotomy naturally leads us to a research question in the field of underwater acoustics: how to effectively model acoustic propagation in any underwater environment using a small amount of acoustic data and limited environmental knowledge? Viable solutions to this research question benefit a wide range of underwater applications which used to be considered practically infeasible in partially unknown underwater environments using conventional propagation models. Underlying domain knowledge can constrain a data-driven algorithm to only learn physically realistic functions, enabling a data-efficient algorithm. Developing a hybrid propagation model that not only learns from data, but also utilizes the knowledge of the physics of acoustic propagation, appears to be a promising direction. Therefore, this thesis focuses on exploring physics-aided data-driven solutions to the stated research question.

1.2 Objective

The main objective of this thesis is to explore physics-based data-efficient underwater acoustic propagation modeling frameworks that are capable of modeling any underwater environment. The modeling frameworks offer flexibility to incorporate varying degrees of environmental knowledge and generalize well to permit extrapolation beyond the area where data are collected.

1.3 Contributions

The followings are the main contributions of this thesis:

1. We develop a recipe to generate physics-aided data-driven acoustic propagation frameworks that efficiently solve the acoustic wave equation. The proposed recipe is able to utilize any available environmental knowledge to solve the acoustic wave equation in a desired number of dimensions (typically one-dimensional (1D), 2D or 3D). It does not require a large amount of training data, and has the ability to extrapolate beyond the region where data are collected.

2. The proposed modeling recipe supports composition, thus enabling us to combine purely data-driven ML models and physics-aided ML models into a single propagation model.

3. The proposed modeling recipe brings interpretability to the trained model parameters, which is particularly useful for geo-acoustic inversion problems.

4. We demonstrate a ray-based data-driven acoustic propagation modeling framework for high-frequency underwater applications based on the ray theory.

5. We demonstrate a mode-based data-driven acoustic propagation modeling framework for low-frequency oceanic applications based on the normal mode theory.

6. We model 3D acoustic propagation in a highly reverberant water tank with an unknown sidewall reflection model. Modeling such an acoustically complicated confined water environment under partial environmental knowledge is practically infeasible using conventional modeling techniques.

7. We propose a robust time-efficient single-hydrophone underwater acoustic source localization algorithm with an informative path planning policy. With the aid of our modeling framework, we can experimentally validate the proposed source localization algorithm in a partially unknown environment. This used to be extremely challenging using conventional propagation models.

1.4 Thesis organization

To highlight key limitations in conventional underwater acoustic propagation models that motivate us to bridge the gap in the following chapters, Chapter 2 dives into the application of deep sea black box search by proposing an informative path planning policy for single-hydrophone underwater acoustic source localization. Chapter 3 presents a brief review of preliminary concepts in underwater acoustics, and works related to underwater acoustic propagation modeling and acoustic path planning.

In Chapter 4, we propose a hybrid high-frequency data-efficient underwater acoustic propagation modeling framework based on the ray theory [30] and demonstrate its uses in both forward and inverse problems through four numerical experiments. With the aid of the proposed hybrid modeling framework, we experimentally model 3D acoustic propagation in a highly

reverberant water tank using partial environmental knowledge in Chapter 5.

The high-frequency approximation in the ray theory breaks down at low frequencies. The normal mode theory [31] is often used in such cases. In Chapter 6, we tailor the proposed acoustic propagation modeling recipe based on the normal mode theory to benefit low-frequency oceanic applications. We demonstrate its capabilities through field prediction and SSP inversion problems in simulation.

It is infeasible to practically implement applications that heavily rely on conventional acoustic propagation models in largely unknown underwater environments. This practical problem in acoustic modeling motivates our research. With the aid of our proposed modeling framework, in Chapter 7, we experimentally validate the path planning policy proposed in Chapter 2 to locate an acoustic source in the partially unknown water tank to close the loop. Finally, Chapter 8 summarizes the key results of the thesis and outlines the directions of future work.

Chapter 2

Single-hydrophone Underwater Source Localization

In Chapter 1, we touched upon the deep sea black box search problem that motivates our research. In this chapter, we dive into it by exploring a time-efficient single-hydrophone underwater source localization algorithm. Conventional underwater source localization strategies are either costly or time inefficient. An alternative approach needs to be explored to overcome such limitations. If an underwater source could be located using a single low-fidelity acoustic sensor, the cost and complexity of source localization applications could be greatly reduced. The key idea is to mount the sensor on an AUV and use the motion of the AUV to spatially sample acoustic fields produced by the source, and then apply the MFP technique to locate the source. The natural next question is: how should the AUV move in order to get the best localization performance in the shortest possible time? This important question is the focus of this chapter. The hurdle we encountered while practically demonstrating the localization algorithm in a partially unknown environment leads us to a research question in underwater acoustics and is addressed in this thesis. The work presented in this chapter is published in [32] and [33].

2.1 Conventional underwater source localization

Conventionally, an underwater acoustic source can be located using a hydrophone array or a single hydrophone. The hydrophone arrays used in such applications are normally bulky. For example, in [34], a 16-element vertical line array with a 3.75 m inter-element spacing is deployed to locate a source 3,000 m away from the array. A sizable surface vessel is required to tow such an array. The implementation complexity and cost are thus high. Taking full use of arrival structures of acoustic signals measured by a hydrophone is a popular strategy used in single-hydrophone source localization. While the implementation complexity and cost are lower in comparison with the hydrophone array methods, the poor spatial diversity that a single hydrophone offers limits its localization performance.

2.1.1 Source localization using a hydrophone array

Majority of commonly used techniques for underwater source localization using a hydrophone array can be generally classified into beamforming [35], MFP [36], time of arrival (TOA) [37], time difference of arrival (TDOA) [38] and data-driven ML [39].

Beamforming is a space-time signal processing technique that fuses the signals received at each element of a hydrophone array to estimate a source. The classical beamformers perform poorly in terms of model robustness and angular resolution [40]. Later research improves them using techniques such as compressive sensing [41] and iterative beamforming [42]. However, the angular resolution of such a spatial filtering approach is limited by the aperture of the

hydrophone array deployed [40]. The beamwidth decreases as the number of array elements and the inter-element spacing increase. The large inter-element spacing creates non-desired lobes in other directions. The number of array elements is inevitably large in order to achieve a good angular resolution.

MFP can be seen as a generalized beamformer that uses spatial variability of acoustic fields to localize a source or infer unknown environmental parameters [36]. This idea dates back to 1976 when authors first propose a quadratic detector to match measured cross-spectral matrix with modeled matrixes [43]. In MFP, the requirement of having a completed and accurate set of environmental parameters is necessary but often impractical. While later research builds upon this pioneering work to improve the algorithm robustness to combat the effects of environmental mismatch [44], [45], MFP models have limited performance in largely unknown underwater environments.

TOA and TDOA are two commonly used source localization approaches based on time measurements. In order to translate arrival time measurements into range information using TOA and TDOA, having a constant SSP across the medium is a critical assumption. This assumption is often not strictly valid in oceans due to the inhomogeneity of seawater [46]. Solutions proposed in [47], [48] relax such an assumption by compensating for stratification effects in inhomogeneous mediums. As TOA and TDOA methods require multiple spatially separated acoustic sensors with accurate time synchronization, they are not extensively used in practice for reliable underwater source localization.

Since the 1990s, ML techniques have been successfully applied in the context of source localization in ocean waveguides [39], [49]–[53]. Despite that

advances in ML improve computational efficiency, localization accuracy and model robustness as compared to classical MFP and beamformer, having a sufficient amount of training data is a must [39]. Using a conventional acoustic propagation model as a surrogate to the actual operating environment is an efficient way to generate any required amount of training data in one go. The environment has to be well understood in the first place. While directly collecting acoustic measurements from the environment eliminates such a requirement, large-scale acoustic data acquisition in oceans is expensive and time-consuming.

2.1.2 Source localization using a single hydrophone

An early experimental attempt at single-hydrophone source localization is carried out in an ideal air-filled wedge waveguide for a broadband source [54]. It matched filters received impulse responses with modeled replicas and cross correlates the matched output with the known input signal. In [55], the authors demonstrate the feasibility of single-hydrophone source localization in an isovelocity ocean environment. In [56], the authors opt to estimate the subspace spanned by delayed arrival paths, instead of estimating time-delayed arrivals. In [57], the authors utilize frequency-range interference patterns collected by a single hydrophone in a deep ocean to locate a source near the surface.

The classical MFP uses measured acoustic signals from a hydrophone array, preferably with a significant aperture, to achieve good spatial discrimination of source location. The information provided by a single hydrophone is not sufficient to locate the source using classical MFP techniques. Matched feature localization is used as an alternative to exploiting multipath arrival structures

received by a single hydrophone. In [58], the authors construct a peak extraction localization algorithm based on the match feature localization using the auto-correction function in shallow waters. The environmental mismatches degenerate localization accuracy of physics-based single hydrophone source localization algorithms. The use of data-driven ML in single-hydrophone source localization has also been actively explored recently [59], [60]. However, the limitations of ML-based methods discussed in Section 2.1.1 are not well tackled in these works neither.

The past works in literature have demonstrated the feasibility of single-hydrophone source localization. Unfortunately, it has limited performance due to a lack of spatial diversity and is sensitive to environmental mismatch. Achieving comparable localization time efficiency and accuracy as the hydrophone array methods are challenging.

2.2 Source localization with accurate environmental knowledge

To overcome the limitations of the existing localization strategies, a simple and time-efficient localization alternative needs to be explored. Intuitively, avoiding the use of a large hydrophone array and an expensive ship could help us significantly reduce the implementation complexity and cost. If we have accurate environmental knowledge, we can collect acoustic measurements spatially using an AUV, fitted with a low-fidelity hydrophone, to replace the towed hydrophone array. This helps to maintain a balance between implementation complexity and time efficiency.

2.2.1 Problem formulation

We aim to locate a black box using a single hydrophone within the shortest possible time. We assume an AUV equipped with an acoustic intensity sensor operating in an underwater environment. We use the MFP as the fundamental localization technique. The conventional MFP technique locates a static source by matching the modeled replica fields with the measurements made at individual receiver positions of a hydrophone array, and finding the candidate source location that gives the best match. We assume that the environment is quasi-static. In order to localize an acoustic source through a single moving hydrophone, we essentially need to spatially sample acoustic fields at different locations such that multiple sets of representative and unique field information can be captured as a replacement for the information acquired by a hydrophone array.

Incorporating the modeled replica fields with the acoustic measurements made at multiple receiver locations is an effective way to reduce the ambiguity of source location. The knowledge of acoustic propagation in the region of interest also gives us information about the locations of the most informative measurement sites. In this manner, we can adaptively plan the AUV's path to maximize information gain of the source location and reduce the time taken to locate the source.

2.2.2 Adaptive path planning policy

The AUV uses prior knowledge (e.g., source is within a specific area of interest, source is on the seabed) to estimate an initial probability distribution for the

source location. The AUV starts at a known location and measures the acoustic

intensity. It compares the measured intensity value against modeled values for

potential source locations, and updates the probability distribution. The AUV

then moves and makes a measurement at another nearby location and repeats

the process. We want to help the AUV plan its move in such a way as to make the

probability distribution of source location as compact as possible, i.e., eliminate

ambiguities in our knowledge of source location, in a short period of time.

At time step i, the probability of the source at a location $\boldsymbol{r}_\mathrm{s}$ based on a set

of measurements and corresponding AUV's positions can be written as:

$$f(\boldsymbol{r}_\mathrm{s}|\{(\boldsymbol{r}_j, y_j)\}\forall j \in [1, i]), \tag{2.1}$$

where $\boldsymbol{r}_j$ is the AUV's position when measurement y_j is made. We henceforth

use set $\mathcal{Z}_i \equiv (\{(\boldsymbol{r}_j, y_j)\}\forall j \in [1, i])$ for a more compact notation. By making the

i^{th} measurement at location $\boldsymbol{r}_i$, the probability distribution of source location

can be updated using Baye's Theorem:

$$
\begin{aligned}
f(\boldsymbol{r}_\mathrm{s}|\mathcal{Z}_i) &= f(\boldsymbol{r}_\mathrm{s}|\mathcal{Z}_{i-1} \cup (\boldsymbol{r}_i, y_i)) \\
&= \frac{f((\boldsymbol{r}_i, y_i)|\mathcal{Z}_{i-1}, \boldsymbol{r}_\mathrm{s})f(\boldsymbol{r}_\mathrm{s}|\mathcal{Z}_{i-1})}{f((\boldsymbol{r}_i, y_i)|\mathcal{Z}_{i-1})} \\
&= \frac{f((\boldsymbol{r}_i, y_i)|\mathcal{Z}_{i-1}, \boldsymbol{r}_\mathrm{s})f(\boldsymbol{r}_\mathrm{s}|\mathcal{Z}_{i-1})}{\int f((\boldsymbol{r}_i, y_i)|\mathcal{Z}_{i-1}, \boldsymbol{r}_\mathrm{s})f(\boldsymbol{r}_\mathrm{s}|\mathcal{Z}_{i-1})d\boldsymbol{r}_\mathrm{s}}.
\end{aligned}
\tag{2.2}
$$

We discretize the candidate source locations to reduce computation complexity.

Equation (2.2) is re-written as:

$$f(\boldsymbol{r}_\mathrm{s}|\mathcal{Z}_i) = \frac{f((\boldsymbol{r}_i, y_i)|\mathcal{Z}_{i-1}, \boldsymbol{r}_\mathrm{s})f(\boldsymbol{r}_\mathrm{s}|\mathcal{Z}_{i-1})}{\sum_{\boldsymbol{r}_\mathrm{s}} f((\boldsymbol{r}_i, y_i)|\mathcal{Z}_{i-1}, \boldsymbol{r}_\mathrm{s})f(\boldsymbol{r}_\mathrm{s}|\mathcal{Z}_{i-1})}. \tag{2.3}$$

We want the probability distribution $f(\boldsymbol{r}_\mathrm{s}|\mathcal{Z}_i)$ to be as compact as possible, such that the uncertainty is minimal. We therefore wish to minimize the entropy of the distribution at each time step i, by selecting the next location for the AUV to move to, essentially yielding an adaptively planned path. Do note that this approach is *greedy* and does not generate a globally optimal path, but still yields good results as shown in the simulation studies in Section 2.2.3.

Minimizing the entropy of the posterior distribution of source location is equivalent to maximizing the information gain in the Bayesian update. We therefore plan our path by choosing an action (direction for the AUV to move) that leads to maximal information gain at each step. Before an AUV makes a measurement at a given location, there is some prior uncertainty about the sound intensity at that location. Once the measurement is made, the uncertainty reduces to the measurement uncertainty (entropy of the measurement noise). Hence the information gained closely follows the prior uncertainty of modeled sound intensity, given $f(\boldsymbol{r}_\mathrm{s}|\mathcal{Z}_i)$. We use weighted variance as a measure of prior uncertainty and choose an action at each time step to yield the next waypoint:

$$\boldsymbol{r}_{i+1} = \arg \max_{\boldsymbol{r}\in\mathcal{A}(\boldsymbol{r}_i)} \sum_{\boldsymbol{r}_\mathrm{s}} f(\boldsymbol{r}_\mathrm{s}|\mathcal{Z}_i)(M(\boldsymbol{r}, \boldsymbol{r}_\mathrm{s}) - \mu)^2, \tag{2.4}$$

where

$$\mu = \sum_{\boldsymbol{r}_\mathrm{s}} f(\boldsymbol{r}_\mathrm{s}|\mathcal{Z}_i) M(\boldsymbol{r}, \boldsymbol{r}_\mathrm{s}), \qquad (2.5)$$

where $M(\boldsymbol{r}, \boldsymbol{r}_\mathrm{s})$ is the modeled acoustic intensity at location $\boldsymbol{r}$ if the source is assumed to be at location $\boldsymbol{r}_\mathrm{s}$, and $\mathcal{A}(\boldsymbol{r}_i)$ is the set of feasible moves for the AUV at location $\boldsymbol{r}_i$.

The essential idea is to let the AUV move in a direction where there is more uncertainty in modeled sound intensity values based on the probability distribution of source location, so as to maximize the reduction of overall entropy. Our algorithm iterates over two steps until the source location is confirmed to a required level of accuracy. Fig. 2.1 summarizes key steps of our proposed algorithm. The first step is to take a measurement at the current AUV's location and update the probability distribution of the source location using (2.3). The second step is to determine the optimal direction for the AUV to move based on the weighted variance using (2.4) and (2.5).

2.2.3 Simulation studies

The proposed source localization method is theoretically feasible with the aid of conventional propagation models. However, accurately measuring all environmental parameters required in the propagation models is challenging. We demonstrate the effectiveness of the proposed algorithm by simulating a well-understood underwater environment first. We improve our model robustness to handle uncertainties in environmental parameters in Section 2.3.
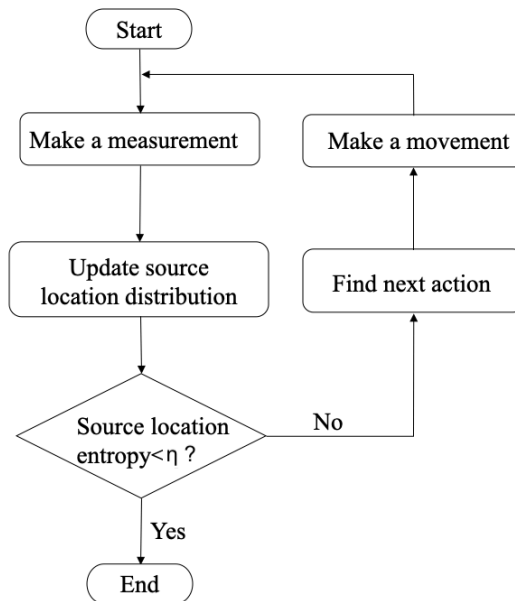
Figure 2.1: Flow chart of the proposed adaptive path planning algorithm for single-hydrophone underwater source localization.

2.2.3.1 Simulation setup

We illustrate the localization performance of our proposed path planning algorithm by simulating a 2D range-independent underwater environment with 1 km range, sandy seabed and constant SSP. We aim to localize a 1 kHz acoustic pinger lying on the seabed. The source location is set to the center of the search space. Fig. 2.2 depicts the ground truth field pattern of the simulated environment. We make use of a holonomic AUV equipped with a single hydrophone to provide the mobility of the receiver. We adopt Bellhop propagation model [61] to generate modeled replica fields. The measurement is simulated by adding random Gaussian instrument noise with a standard deviation of 5.6 μPa to the modeled fields to simulate low-fidelity acoustic measurements. We also consider ambient noise with a spectral level of
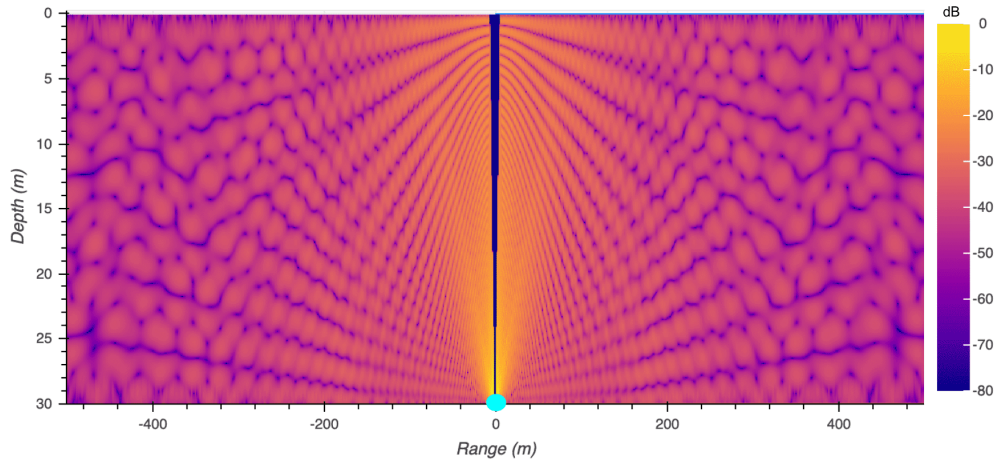
Figure 2.2: Modeled field pattern over the simulated environment. The source location is indicated as the coral blue dot on the center of the seabed.

50 dB re μPa^2/Hz for 1 kHz source with 100 Hz bandwidth based on Wenz curve [62].

The AUV initially starts at a depth of 15 m and a range of 200 m from the source. We compare the localization performance of our proposed *adaptive* path planning policy with four naive path planning policies, which we term as *straight* policy, *random* policy, *lawnmower* policy and *zig-zag* policy, over 100 Monte Carlo runs. The straight policy moves the AUV in a straight horizontal direction at a constant depth. The random policy allows the AUV to move in a random direction at each step. The lawnmower and zig-zag policies move AUV along the lawnmower and zig-zag shape paths from its initial position towards the center of the search space. The lawnmower policy horizontally shifts the AUV for 1 m when the AUV reaches the bottom or surface of the sea. The zig-zag policy moves AUV along the path with a slope of 45 °. We assume that in adaptive and random policies, the AUV moves in a specific direction, defined within the motion set, which contains discretized bearings of 45 ° apart, and the
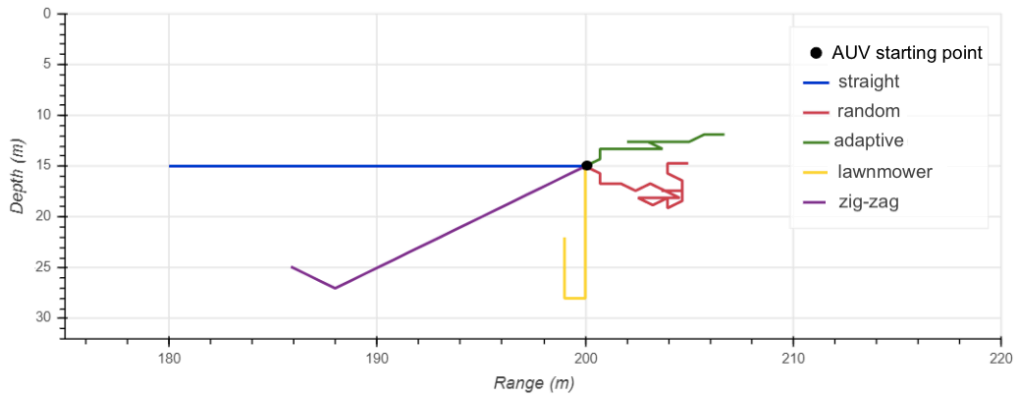
Figure 2.3: An example of 20 m paths planned by the five path planning policies.

AUV moves 1 m at each time step for all policies. Fig. 2.3 shows 20 steps of sample paths planned by the five path planning policies. The source location is finalized when its entropy falls below a threshold η and is determined based on the maximum a posteriori rule.

2.2.3.2 Localization time efficiency

Time used to locate the source is a key metric to evaluate the localization performance of the proposed adaptive policy. We use trimmed mean* of steps required to make the source location entropy converge below η over 100 Monte Carlo runs as a measure of localization time efficiency. In Fig. 2.4, we show the entropy history of the five policies from one Monte Carlo run as an example. Table 2.1 shows that the adaptive policy can locate the source in 7 steps on average, which is the fastest among all policies.

---

*The trimmed mean is defined as the mean calculated by excluding the data that deviate more than three times of the standard deviation from the sample mean of the original full dataset. The data excluded from the trimmed mean calculation is marked as the outliers.
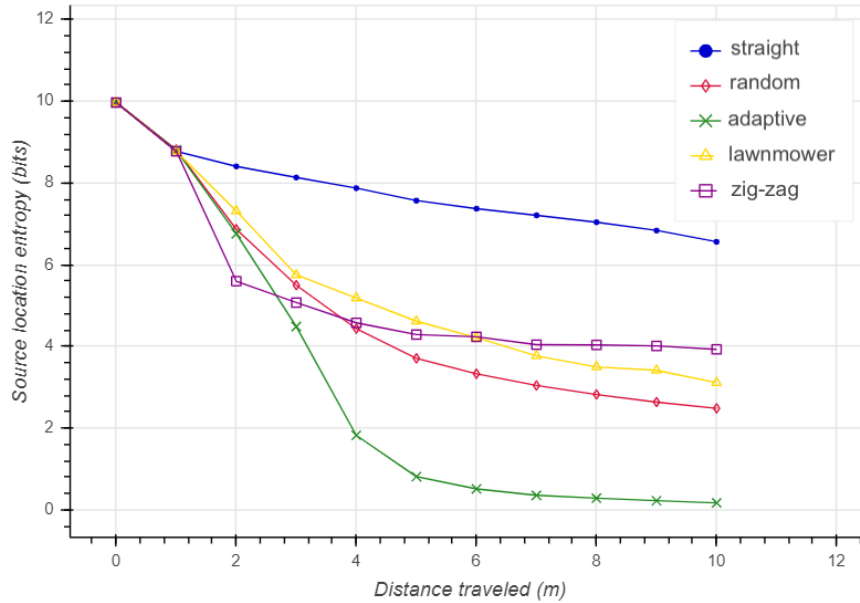
Figure 2.4: Source location entropy history up to 10 steps for the five policies when environmental knowledge is accurately known.

2.2.3.3   Localization accuracy

Having a small entropy of source location distribution does not necessarily imply that it can locate the source accurately. It is also important to make sure that our proposed localization approach can converge to the right source location by the end of the search. We use the same set of localization results presented in Section 2.2.3.2 to calculate root-mean-square error (RMSE) and mean absolute error (MAE) of the located source from the 100 Monte Carlo runs. The results obtained in Section 2.2.3.2 produce zero RMSE and MAE for all five policies.

The two sets of results demonstrate that locating an underwater source using a single hydrophone is feasible. The adaptive path planning policy can locate the source in a shorter time as compared to the naive policies.

TABLE 2.1: Average number of steps required to make source location entropy converged for all policies when environmental knowledge is accurately known.

Policy	Average steps of convergence	No. of outliers
Straight	50.6	1/100
Random	37.9	10/100
Adaptive	6.9	11/100
Lawnmower	79.2	5/100
Zig-zag	19.9	0/100

2.2.3.4 Effects of environmental mismatch in localization

In practice, we often face a situation where we know little about the environment or the actual environment deviates from our understanding. Being sensitive to environmental mismatch is recognized as the main limitation in MFP models. How the mismatch affects localization performance for various path planning policies is yet to be investigated.

We set the water depth and sound speed to generate the modeled replicas as 28 m and 1533 m/s, whereas the ground truth values used to generate synthetic acoustic measurements are 30 m and 1542 m/s. In Table 2.2, we list down the average number of steps required to make source location entropy converged and the corresponding localization errors. The environmental mismatch does not necessarily lead to slower convergence, but it does confuse the processor where the correct source is for most of the policies. While all policies have perfect localization accuracy once the source location distribution is converged in well understood environments, the environmental mismatch presented significantly worsens localization accuracy as shown in Table 2.2. It is worth noting that

TABLE 2.2: The average number of steps required to make source location entropy converged when environmental mismatch occurred.

Policy	Average steps of convergence	RMSE (m)	MAE (m)	No. of outliers
Straight	56.1	58.2	41.0	7/100
Random	29.4	195.3	192.6	8/100
Adaptive	8.3	191.8	182.0	12/100
Lawnmower	109.0	0.6	6.9	9/100
Zig-zag	17.3	168.9	140.7	2/100

although the localization error for lawnmower policy is very small, it takes a much longer path on average to reduce the uncertainty of source location distribution to the desired level when environmental mismatches occur.

2.3 Source localization with environmental mismatch

As illustrated in Section 2.2.3.4, implementing the proposed source localization algorithm using conventional propagation models is theoretically feasible if the environment is accurately known. If any environmental parameter in the propagation model is uncertain, the modeled replica fields would be inaccurate, causing significant degradation in localization performance.

2.3.1 Robust MFP-based source localization

To handle the environmental uncertainties in the MFP, we add the uncertain environment parameters $\boldsymbol{\tau}$ into the Bayesian update process in (2.2). Unlike the case where the environment is accurately known, now we need to generate the replica fields corresponding to all possible environment parameter combinations for each candidate source location at each time step i, and apply the MFP technique to the entire set of replica fields. The distribution of source location

is inferred by finding the marginal distribution over all uncertain environmental parameter combinations $\boldsymbol{\tau}$. And (2.2) then becomes:

$$
\begin{aligned}
f(\boldsymbol{r}_\mathrm{s}|\mathcal{Z}_i) &= \int f(\boldsymbol{r}_\mathrm{s}, \boldsymbol{\tau}|\mathcal{Z}_i) d\boldsymbol{\tau} \\
&= \int f(\boldsymbol{r}_\mathrm{s}, \boldsymbol{\tau}|\mathcal{Z}_{i-1} \cup (\boldsymbol{r}_i, y_i)) d\boldsymbol{\tau} \\
&= \int \frac{f((\boldsymbol{r}_i, y_i)|\mathcal{Z}_{i-1}, \boldsymbol{r}_\mathrm{s}, \boldsymbol{\tau}) f(\boldsymbol{r}_\mathrm{s}, \boldsymbol{\tau}|\mathcal{Z}_{i-1})}{\int \int f((\boldsymbol{r}_i, y_i)|\mathcal{Z}_{i-1}, \boldsymbol{r}_\mathrm{s}, \boldsymbol{\tau}) f(\boldsymbol{r}_\mathrm{s}, \boldsymbol{\tau}|\mathcal{Z}_{i-1}) d\boldsymbol{\tau} d\boldsymbol{r}_\mathrm{s}} d\boldsymbol{\tau}.
\end{aligned} \tag{2.6}
$$

The derivation in (2.6) is analytically complicated. We discretize the uncertain parameters and candidate source positions for simplification in simulation. Equation (2.6) becomes:

$$
f(\boldsymbol{r}_\mathrm{s}|\mathcal{Z}_i) = \sum_{\boldsymbol{\tau}} \frac{f((\boldsymbol{r}_i, y_i)|\mathcal{Z}_{i-1}, \boldsymbol{r}_\mathrm{s}, \boldsymbol{\tau}) f(\boldsymbol{r}_\mathrm{s}, \boldsymbol{\tau}|\mathcal{Z}_{i-1})}{\sum_{\boldsymbol{r}_\mathrm{s}} \sum_{\boldsymbol{\tau}} f((\boldsymbol{r}_i, y_i)|\mathcal{Z}_{i-1}, \boldsymbol{r}_\mathrm{s}, \boldsymbol{\tau}) f(\boldsymbol{r}_\mathrm{s}, \boldsymbol{\tau}|\mathcal{Z}_{i-1})}. \tag{2.7}
$$

The policy to determine the optimal next direction in (2.4) is modified to:

$$
\boldsymbol{r}_{i+1} = \arg \max_{\boldsymbol{r} \in \mathcal{A}(\boldsymbol{r}_i)} \sum_{\boldsymbol{r}_\mathrm{s}} f(\boldsymbol{r}_\mathrm{s}|\mathcal{Z}_i)(\bar{M}(\boldsymbol{r}_\mathrm{s}, \mathcal{Z}_i, \boldsymbol{r}) - \mu(\mathcal{Z}_i, \boldsymbol{r}))^2, \tag{2.8}
$$

where

$$
\bar{M}(\boldsymbol{r}_\mathrm{s}, \mathcal{Z}_i, \boldsymbol{r}) = \sum_{\boldsymbol{\tau}} f(\boldsymbol{\tau}|\boldsymbol{r}_\mathrm{s}, \mathcal{Z}_i) M(\boldsymbol{\tau}, \boldsymbol{r}, \boldsymbol{r}_\mathrm{s}), \tag{2.9a}
$$

$$
\mu(\mathcal{Z}_i, \boldsymbol{r}) = \sum_{\boldsymbol{r}_\mathrm{s}} f(\boldsymbol{r}_\mathrm{s}|\mathcal{Z}_i) \bar{M}(\boldsymbol{r}_\mathrm{s}, \mathcal{Z}_i, \boldsymbol{r}), \tag{2.9b}
$$

where $M(\boldsymbol{\tau}, \boldsymbol{r}, \boldsymbol{r}_\mathrm{s})$ is the modeled replica field at location $\boldsymbol{r}$ by assuming the source is at location $\boldsymbol{r}_\mathrm{s}$ and environment parameter set used in propagation model is $\boldsymbol{\tau}$. $\bar{M}(\boldsymbol{r}_\mathrm{s}, \mathcal{Z}_i, \boldsymbol{r})$ denotes the expected modeled replica field over all uncertain

environmental parameters $\boldsymbol{\tau}$ when source is at location $\boldsymbol{r}_s$ and receiver is at location $\boldsymbol{r}$ based on all collected data $\mathcal{Z}_i$. $\mu(\mathcal{Z}_i, \boldsymbol{r})$ is the expected modeled replica field at receiver location $\boldsymbol{r}$ over all candidate source locations and environmental parameter sets by considering the collected information $\mathcal{Z}_i$.

2.3.2 Simulation studies

2.3.2.1 Simulation setup

Typically, water depth and sound speed may vary over time. In the underwater environment described in Section 2.2.3.1, we consider a scenario that the average water depth is 30 m with a rough tide variation of maximal 2 m, water temperature varies within the range of 26 °C to 31 °C and salinity of seawater ranges from 3.2 % to 3.75 %. Based on THEMackenzie empirical equation for sound speed in ocean [63], the resultant sound speed varies from 1533 m/s to 1551 m/s. To simulate the environmental mismatch, we assume that the water depth and sound speed are uncertain. We set the water depth and sound speed in the Bellhop propagation model to 28 m and 1533 m/s to generate the modeled replica fields. The ground truth values used to generate synthetic measurements are 30 m and 1542 m/s. We assume that they are uniformly distributed from 28 m to 32 m and 1533 m/s to 1551 m/s respectively if no prior information is available.

2.3.2.2 Localization performance

We assume that the acoustic source is lying on the seabed and the water depth of the environment is uncertain. In this way, we need to search for both source depth and range. To reduce the computational complexity in simulation, we
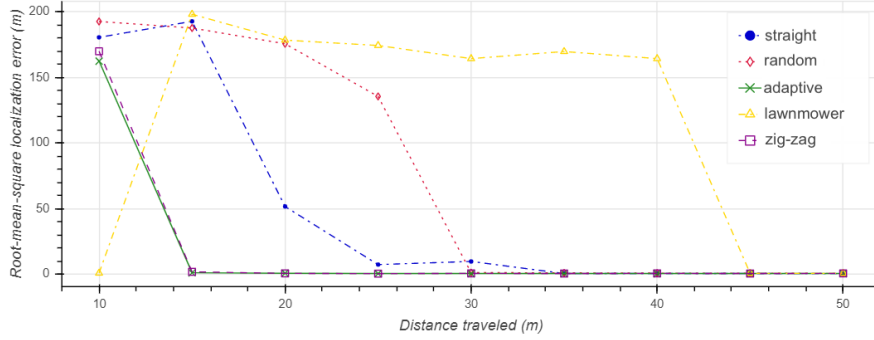
(a) RMSE history
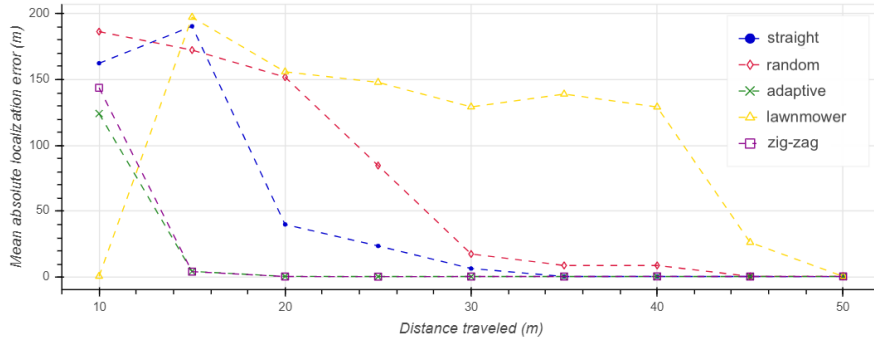
(b) MAE history
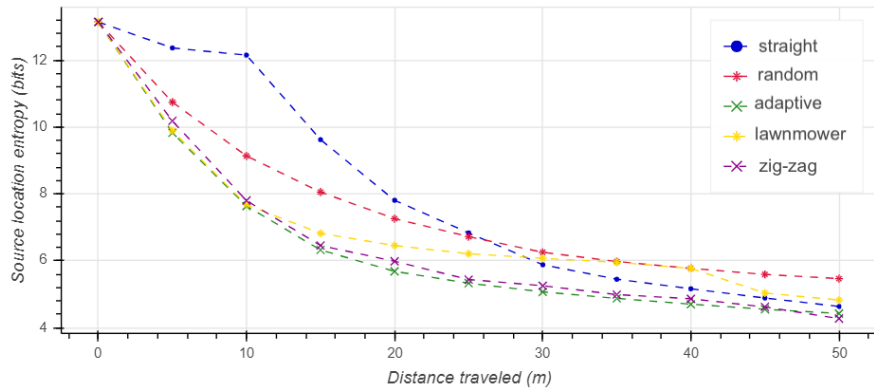
(c) Entropy history

Figure 2.5: Average localization performance of the five policies after moving different path lengths by applying the robust localization approach in the environmental mismatch scenario.

discretize the candidate source locations by a step size of 0.5 m in range and depth. As expected, all policies take longer steps to locate the source as the number of candidate source locations increases and the environment is uncertain. In Fig. 2.5, we present the RMSE, MAE and source location entropy history for all policies by moving AUV along paths ranging from 10 m to 50 m with a step size of 5 m.

We demonstrate effectiveness of our robust localization algorithm as all policies can locate the source location correctly. Meanwhile, the adaptive policy and zig-zag policy outperform other naive policies in terms of localization accuracy and time efficiency. The differences in localization performance between adaptive policy and zig-zag policy in the simulated scenario are not obvious. One of the main reasons could be the current adaptive policy is greedy. The zig-zag policy has a higher chance to move across a wide horizon where the acoustic field variation is stronger than the acoustic fields sampled by the adaptive policy. Considering a few steps look-ahead while planning AUV's next waypoint can effectively improve the localization performance of the adaptive policy.

2.4 Summary

In this chapter, we presented an adaptive path planning policy for robust single-hydrophone underwater acoustic source localization. The proposed method spatially samples the acoustic fields using a single hydrophone in the search area to form a dynamic beamformer. It allows the AUV to move on the most informative path to enhance localization time efficiency, instead of following

the naive paths. By incorporating the uncertain environmental parameters into the update process of the source location distribution, it assures that the MFP performs well with the presence of minor environmental uncertainties. Simulation studies showed the superiority of the proposed adaptive path planning policy over the naive policies in terms of time efficiency. While we specifically focus on the acoustic signal in this chapter, the algorithm we proposed is general and may be used with any kind of signal.

We intend to validate the proposed algorithm in a real world experiment. It is difficult to implement the proposed robust source localization algorithm in a partially unknown practical underwater environment, for the reason that popular propagation models require full and accurate environmental and physical knowledge to generate modeled replicas. Such a practical hurdle motivates us to explore other propagation modeling alternatives to tackle largely unknown environments in later chapters. We will briefly review works related to underwater acoustic propagation modeling to justify the research gap in the next chapter. We will also practically validate the proposed MFP-based localization algorithm using our proposed hybrid modeling recipes under partial environmental knowledge in Chapters 7 to close the loop.

Chapter 3

Background

We explain some basic concepts in underwater acoustics to readers who are not familiar with the terminologies. We review the state of the arts in underwater acoustic propagation modeling to show current techniques and their limitations, highlighting the research gap that is worth being addressed in the remaining chapters. The underwater applications we demonstrate in Chapter 2 and Chapter 7 heavily involve underwater path planning of AUVs with the aid of acoustic propagation models. We also briefly review acoustic-based path planning techniques to provide necessary background information.

3.1 Preliminary concepts

The use of electromagnetic waves in underwater environments is very limited as they are severely attenuated in water. Acoustic waves propagate well in water, making them a feasible choice for underwater applications. The propagation of acoustic waves in underwater environments is complicated by the fact of unique environmental characteristics and propagation phenomena (Fig. 3.1). For example, sounds are reflected by sea surfaces and seabeds, with reflective characteristics highly depending on geo-acoustic structures of boundaries. Bathymetric fluctuations geometrically complicate bottom reflected waves. Sound speed in water typically varies with depth, causing sounds to propagate
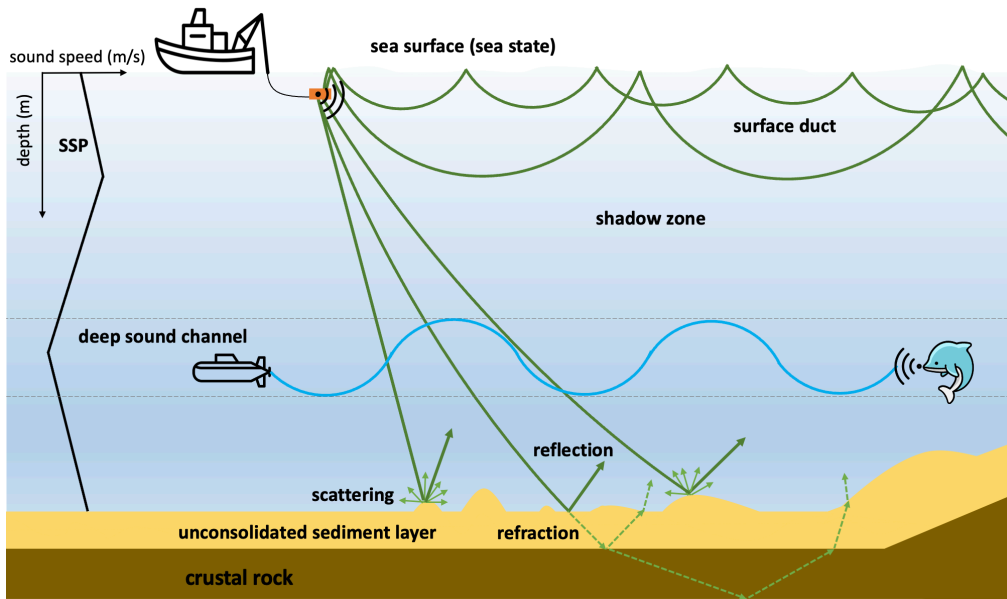
Figure 3.1: An illustration of some key acoustic propagation phenomena in a typical ocean waveguide.

in bent paths due to refraction. The variability of SSP also leads phenomena such as surface ducts [64], shadow zones [64], convergence zones [64] and deep sound channels [64]. The refracted, reflected and scattered waves interfere with each other, making underwater environments acoustically complicated and challenging to model.

We explain some key effects in detail to improve the readability of the thesis, at the same time, allowing readers to have a better understanding of challenges in acoustic propagation modeling. The reviews presented in this section are not exhaustive. Detailed information involved in underwater acoustic propagation can be found in [64]. Those who are familiar with underwater acoustics can safely skip this section.
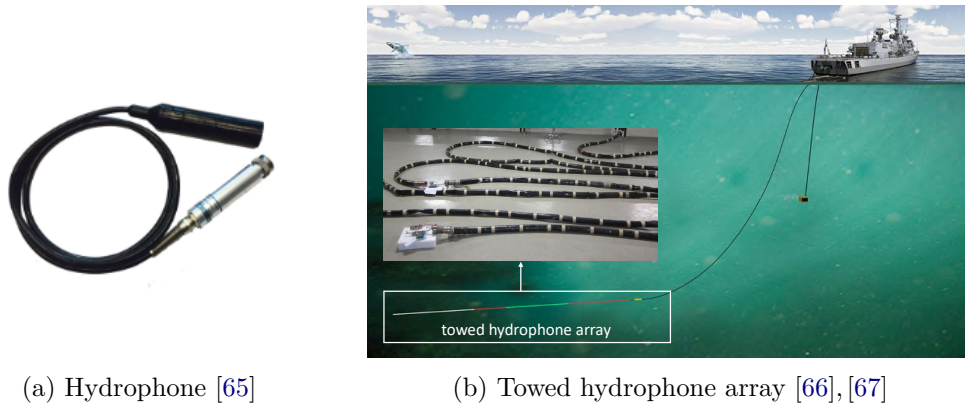
(a) Hydrophone [65]   (b) Towed hydrophone array [66], [67]

Figure 3.2: Examples of a hydrophone and a towed hydrophone array.

3.1.1   Intensity and decibel

In underwater environments, we use a hydrophone (an underwater microphone as shown in Fig. 3.2a) or a hydrophone array (an array of hydrophones as shown in Fig. 3.2b) to measure acoustic pressure p at a location or multiple locations. The intensity I of an acoustic signal is proportional to the square of the pressure p:

$$I = \frac{p^2}{\rho c},$$

(3.1)

where ρ denotes density and c represents sound speed in the water.

Decibel (dB) is a commonly used unit in underwater acoustics and denotes the ratio of intensities I_1 and I_2 in logarithmic scale [29]:

$$10 \log \frac{I_1}{I_2} \text{ (dB)}.$$

(3.2)

An absolute intensity can be expressed by referring to a reference intensity. The standard reference intensity used in underwater acoustics is the intensity

of a plane wave with the RMS pressure of 10^{-6} pascals (Pa) or equivalently 1 micropascal (μPa). For example, $10 \log(10) = 10$ dB re 1 μPa represents an acoustic wave with an intensity 10 times of the reference plane wave with RMS pressure of 1 μPa [64].

3.1.2 Geometric spreading loss

Technically, the geometric spreading loss is not a loss. It is due to the fact that the energy of an acoustic wave spreads over a larger surface as the wave propagates away from a source, leading to an intensity drop [64]. The spreading loss depends on the propagation distance. The acoustic energy can spread spherically or cylindrically depending on channel geometry.

3.1.3 Volume absorption loss

As an acoustic wave propagates away from a source, part of its energy is absorbed (e.g., transformed into heat) [68]. The absorption coefficient per unit propagation distance rapidly increases with frequency, making acoustic communication best supported at low frequencies and bandwidth-limited [69]. The absorption coefficient in seawater can be calculated using empirical formulas [70], [71].

3.1.4 Boundary interactions

Acoustic waves in water reflect, refract and/or scatter when they hit boundaries such as seabed, sea surface and objects. Acoustic waves that are incident on flat sea surfaces (water-air interfaces) undergo a phase inversion with negligible reflection losses. Swells and winds make sea surfaces rough, leading to extra losses in surface reflected waves and may result in strong reverberations

because of frequency-dependent scattering effects. *Sea state* [72] characterizes the roughness of the sea surface and is useful to estimate surface reflective characteristics.

Structures and geo-acoustic properties of ocean bottoms vary from place to place, but they are important to acoustic waves that interact with seabeds. There are various types of compositions in ocean bottoms, including sandy clay, coarse silt, rock, fine sand and mud. Each of them has different geo-acoustic properties, such as density, sound speed and absorption coefficient. Some oceans have multiple layers below marine sediments. The detailed reflective characteristics of ocean bottoms are complicated and hard to be directly measured. *Boundary conditions* of ocean waveguides specify the reflective characteristics at the water-seabed and water-air interfaces.

In *shallow water* channels where horizontal propagation ranges are much larger than water depths, acoustic waves experience multiple boundary interactions. The properties of the surface, bottom and volume are all important to characterize shallow water channels. On contrary, in *deep waters*, lossy seabeds usually allow higher penetration of sounds as acoustic waves are incident at deeper angles, leading to higher reflection losses and making boundary interactions less frequent [64].

3.1.5 Transmission loss

Transmission loss denotes overall signal attenuation as waves propagate in mediums. It is a net effect of geometric spreading loss, absorption loss and reflection loss. It is defined as the ratio in decibels of measured intensity I at
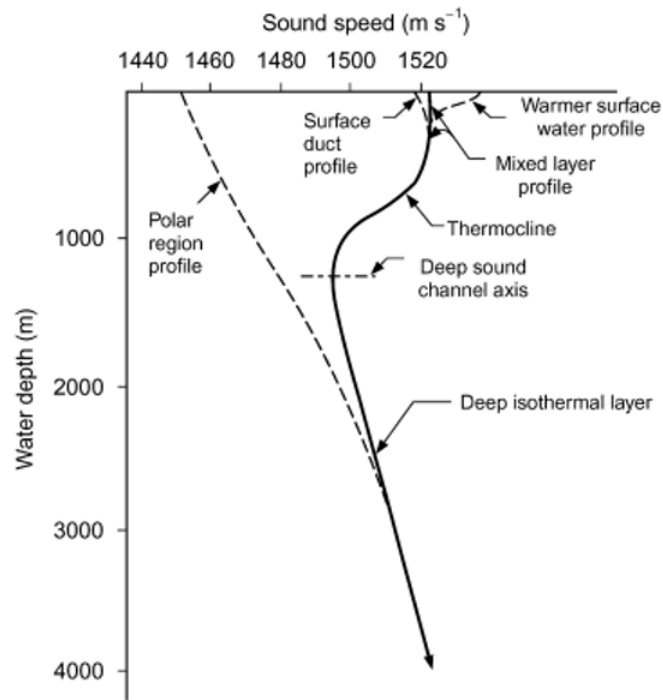
Figure 3.3: A generic SSP in a typical deep ocean waveguide [73].

a location $\boldsymbol{r}$ and reference intensity I_{ref} measured at the location 1 m from the source [64]:

$$
\begin{aligned}
\text{TL} &= -10 \log \frac{I(\boldsymbol{r})}{I_{\text{ref}}} \\
&= -20 \log \frac{p(\boldsymbol{r})}{p_{\text{ref}}} \quad (\text{dB re 1 m}).
\end{aligned}
\tag{3.3}
$$

3.1.6 Sound speed profiles

Speed of sound is a major factor that affects acoustic propagation in water. Sounds propagate in water with a nominal speed of 1,500 m/s. Due to the inhomogeneity of underwater environments, sound speed deviates from the nominal value and increases with water temperature, salinity and hydrostatic pressure. Speed of sound can be determined by various empirical formulas [74]
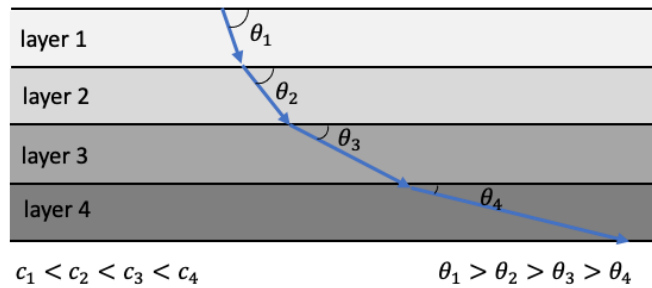
Figure 3.4:   Acoustic propagation in water with multiple sound speed layers. The path of acoustic energy bends towards the layer with lower sound speed c.

and measured through conductivity-temperature-depth (CTD) sensors.

In the domain of ocean acoustics, we are more interested in SSP, which describes variation of sound speed with respect to water depth. In general, the pressure increases with water depth. The salinity might increase or decrease with water depth and varies within a small range. The temperature profile varies from ocean to ocean and season to season. The temperature is a dominating factor that affects the sound speed in the water. Fig. 3.3 depicts a generic SSP in a typical deep ocean waveguide.

The variability of SSP not only makes paths of acoustic energy bend towards regions with lower sound speed (Fig. 3.4), but also leads to some unique propagation phenomena. For instance, mix layers near sea surfaces may have slightly increasing sound speed, forming natural waveguides that trap acoustic energy and result in the surface ducts. Acoustic waves left at steeper angles can escape from surface ducts. Regions where acoustic waves do not reach are shadow zones. Sound waves are focused in convergence zones. Depth with minimal sound speed is referred to as deep sound channel axis. A deep sound channel, which is a region around the deep sound channel axis, permits long-range propagation

without bottom interactions. These phenomena further complicate acoustic propagation in oceans.

3.1.7 Multipath propagation

Underwater environments exhibit rich multipath propagation due to reflections of surrounding boundaries and objects, and refractions of spatial varying sound speed [75]. The trajectory of a particular arrival is determined by channel geometry and SSP structure [76]. Multipath arrivals with different amplitudes and phases interfere, leading to complicated interference patterns of acoustic fields. Fig. 3.5 shows an example of multipath propagation at a location in the ocean waveguide that generates the acoustic field patterns of Fig. 1.1.

(a) Multipath trajectories (b) Impulse response
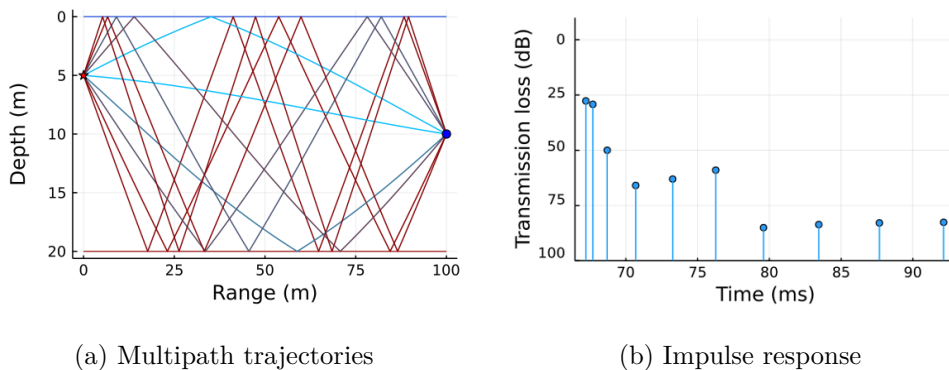
Figure 3.5: Multipath propagation in the ocean waveguide simulated in Fig. 1.1.

3.1.8 Range dependence

Propagation models can be categorized into *range-dependent* and *range-independent* models based on environmental dependence. Range-dependent models deal with underwater environments whose input parameters, such as bathymetry and SSP, vary with ranges. Range-independent

models are used when environmental parameters are constant with respect to ranges [7].

3.1.9 Plane waves and spherical waves

Surfaces of constant phases in spherical waves form spheres, whereas wavefronts of plane waves are parallel planes. The spherical waves due to an omnidirectional point source can be locally approximated as plane waves in far-field where ranges are more than 10 times of wavelength λ (Fig. 3.6). Such an approximation allows us to ignore detailed geometric spreading loss and absorption loss to simplify modeling problems in far-field regions.
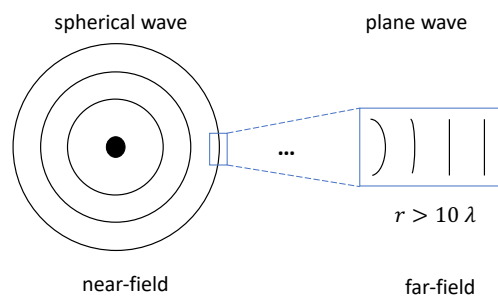
Figure 3.6: Spherical waves in near-field and plane waves in far-field.

3.1.10 Propagation modeling

We briefly explain some dominating effects that govern acoustic propagation in water. Accurately modeling acoustic propagation in underwater environments is challenging but important. Conventional underwater acoustic propagation models consider key propagation phenomena to predict acoustic signals (e.g., impulse responses, transmission losses, pressure amplitudes) received at locations of interest.

3.2 Underwater acoustic propagation modeling

As technology has advanced over the years, there are various techniques can be used to model underwater acoustic propagation. Fig. 3.7 summarizes the hierarchy of three state-of-the-art modeling techniques that are discussed in this section.
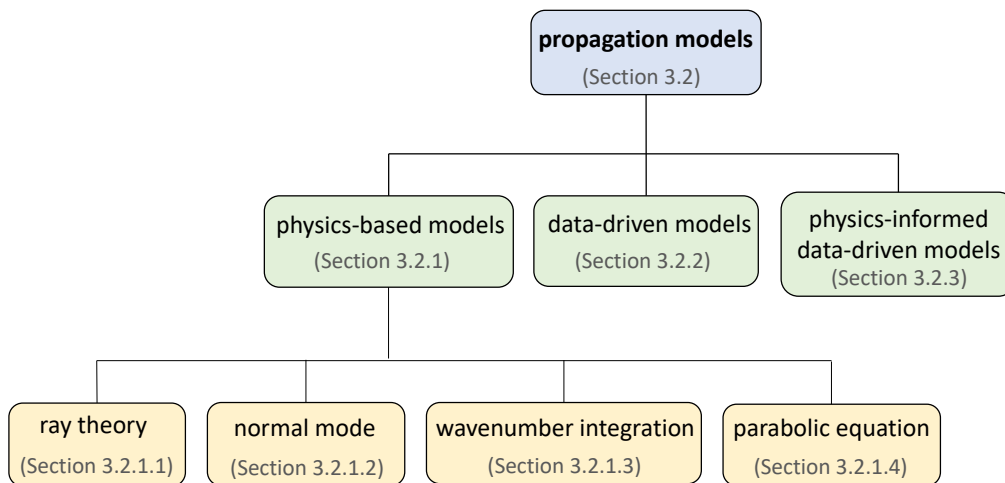
Figure 3.7: Hierarchy of state-of-the-art underwater acoustic propagation modeling techniques.

3.2.1 Physics-based models

Conventional physics-based propagation models translate our physical understanding of acoustic propagation into mathematics. They are derived from the acoustic wave equation [29]. Closed-form solutions to the acoustic wave equation with boundary conditions are analytically intractable. There are various approximations and techniques used to solve the acoustic wave equation, most of which can be seen as variants of the following four groups: ray methods [30], normal mode methods [31], wavenumber integration methods [77] and parabolic equation methods [78]. Other modeling techniques, such as

TABLE 3.1:   Applicability of popular conventional propagation modeling methods [7].

Method	Model[1][81]	Applicability			
		Shallow water		Deep water	
		LF[2]	HF[3]	LF	HF
Ray theory	Bellhop [61]	$\times$[4]	$\checkmark$[5]	�checkmark[6]	$\checkmark$
Normal mode	Kraken [82]	$\checkmark$	✔	✔	$\times$
Wavenumber integration	Scooter [81]	$\checkmark$	$\checkmark$	$\checkmark$	✔
Parabolic equation	RAMGeo [81]	$\checkmark$	✔	$\checkmark$	$\times$

[1] We only list one example of available models in each method. Work [76] provides a full list of available models and software.
[2] LF: low frequency (<500 Hz)
[3] HF: high frequency (>500 Hz)
[4] $\times$: neither suitable nor applicable
[5] $\checkmark$: suitable
[6] ✔: applicable with limitations

finite-difference methods [79] and finite-element methods [80], are also publicly available. Their practical uses are fairly limited due to extensive computational costs. Thus, we only discuss the four major techniques in this section.

The choice of appropriate method to use mainly depends on the environment and frequency. Table 3.1 briefly summarizes the applicability of the four types of physics-based modeling methods. Although our proposed modeling recipe can be applied to any viable physics-based model, we specifically focus on the ray methods and the normal mode methods in this thesis because they have a good balance between model applicability and computational complexity. We demonstrate our proposed modeling recipe based on the ray theory and normal mode theory in later chapters.

3.2.1.1 Ray methods

The ray methods solve the acoustic wave equation by applying a high-frequency approximation to track trajectories of a set of *rays* (paths that acoustic energy travels) originating from a source as they propagate in water [30], [83], [84]. They can be seen as an intuitive way to interpret solutions to the wave equation at high frequencies. A few rays might be enough to determine acoustic fields in distant regions, while more rays are required to rigorously model acoustic propagation in near regions. The ray methods can accommodate the directionality of the source and receiver easily by controlling weights in launch and arrival angles of rays.

Trajectories of rays are sensitive to environmental information, such as SSP, bathymetry, bottom reflective characteristics and channel geometry, especially for long-range ray tracing. The high-frequency approximation used to solve the wave equation inherently leads to poor modeling accuracy at low frequencies. Classical ray theory has flaws in acoustic field predictions involving diffractions and caustics [30]. Rays can reflect and refract, but not diffract. The classical ray theory assumes that no sound propagates in shadow zones. Diffractions make acoustic waves leak into the shadow zones near boundaries, violating the assumption made by the ray theory. The caustics are ray artifacts that several adjacent rays converge in close proximity, resulting in unusual high-intensity regions. There are some modified ray-based models to correct these flaws. For example, as a variant of ray tracing, beam tracing methods are developed by replacing rays (has no thickness) with beams (e.g., Gaussian beams, hat-shaped

beams) [85], [86].

The ray-based models handle SSP variation fairly well and can be extended to range-dependent environments. They are computationally efficient and suitable for high-frequency modeling problems.

3.2.1.2   Normal mode methods

An alternative decomposition of solution to the acoustic wave equation leads to the concept of modes. The normal mode methods compute all contributing modes and sum up the collection of modes to estimate the acoustic field at a point [31], [87]. The number of modes required for a good approximation grows rapidly with frequency and depth, but is independent of propagation range. Normal mode models are best suited for low-frequency applications in shallow water and efficient for long-range propagation modeling. Unlike the ray methods, the normal mode models can compute acoustic fields anywhere in between the source and receiver once all modes are found. Modes that can propagate long distances from a source are propagating modes, whereas modes that decay rapidly are leaky modes or evanescent modes. A major challenge in normal mode models is to accurately find all contributing modes in a short time. Only considering propagating modes makes normal mode programs efficient, but loses modeling accuracy at close ranges where leaky modes and evanescent modes matter [31].

The normal mode theory uses the separation of variables to divide solutions into a range-dependent term and a depth-dependent term. Classical normal mode models solve the acoustic wave equation trivially for range-independent

oceanic environments. For mildly range-dependent environments where environmental parameters vary slowly in range, the adiabatic mode theory can be utilized [88]. For highly range-dependent environments, the full coupled mode theory is often used to explicitly solve the horizontal term [89]. The coupled mode theory divides the range-dependent environment into several sections, each of which can be approximately seen as a range-independent environment. Hence, the full coupled mode method is extremely computationally intensive. The adiabatic mode theory is less computationally expensive than the full normal mode methods.

3.2.1.3 Wavenumber integration methods

The wavenumber integration methods, also called fast-field methods, separate the acoustic wave equation based on the normal mode approach and use the fast Fourier transform to evaluate an infinite integral term to explicitly solve the acoustic wave equation [77], [90]. The wavenumber integration methods find all propagating modes, leaky modes and evanescent modes to form an exact solution in range-independent environments [7]. They are often used as a benchmark solution and can be extended to range-dependent environments. The practical use of the wavenumber integration methods is very limited due to high computational complexity.

3.2.1.4 Parabolic equation methods

The parabolic equation methods solve the wave equation by considering outgoing waves and ignoring the back-scattered energy [78], [91]. With the simplification, the propagation modeling problem reduces to an initial-value problem in terms

45

of range [92]. As their computational complexity scales poorly with frequency, the parabolic equation methods are best supported at low frequencies [7].

3.2.1.5 Practical limitations

Physics-based models take source location, environmental parameters and boundary conditions that affect acoustic propagation in oceans as model inputs to predict received signals at particular receiver locations. Some common environmental parameters include SSP, volume absorption coefficient, sea state, sediment characteristics and bathymetry [7]. Therefore, conventional physics-based models require full and accurate environmental knowledge beforehand. Their prediction performance heavily relies on the accuracy of the environmental knowledge provided. In [93], sensitivities of physics-based model parameters are studied and the geo-acoustic parameters are shown to have significant influences on modeling accuracy.

While these models are commonly applied in 2D environments, full 3D modeling of large-scale environments is often computationally infeasible using conventional models. As computational capacity has advanced over the years, there have been advances to solve 3D problems [94]–[96]. Yet, a common approach today is to approximate 3D propagation effects by applying 2D models to N azimuths. This idea is often referred to as 2.5D models or $N{\times}2$D models in literature [97], [98]. The 2.5D models can only be applied in environments where the out-of-plane arrival energy is insignificant.

Although the acoustic wave equation holds true in any underwater environment, conventional propagation models are designed for typical ocean

waveguides (open water environments) where out-of-plane arrival energy is negligible. Modeling acoustic propagation in confined water environments that are structurally different from ocean waveguides using conventional models is challenging, especially for irregular confined waters with unknown boundary reflective characteristics.

3.2.2 Data-driven models

3.2.2.1 Related works

The emergence of data-driven ML algorithms has had a profound impact on many fields [23]. ML algorithms allow computers to automatically learn from data [24]. Many underwater applications also benefit from ML [25]. For example, ocean acoustic fields may be modeled using classical data-driven ML techniques such as GPR and DNN, assuming sufficient acoustic field measurements and network capacity are provided for the models. The Gaussian process model is a probabilistic model. It is widely used for regression and classification problems. The GPR is capable of capturing relations between inputs and outputs through non-parametric Bayesian inference [26]. Given a set of acoustic measurements and the corresponding measurement locations, the GPR can interpolate and extrapolate acoustic predictions with uncertainty distributions at unvisited locations. The computational cost of traditional GPR models scale poorly with the training data size, but sparse GPR models have been proposed to counter such a limitation [99]. The availability of a large number of accessible datasets has driven the rapid growth in the development of ML algorithms over the past years. DNN is a popular technique in ML models. The universal function

approximation theorem establishes that multilayer feed-forward networks have the capability to approximate any continuous function given a sufficient number of hidden units [100]. This suggests that a DNN should be able to approximate the solution to the acoustic wave equation by learning appropriate weights from training data.

To the best of our knowledge, the use of data-driven techniques in acoustic modeling for forward problems is very limited. In [101], the authors explore the feasibilities of modeling underwater acoustic communication channels through DNN and long short term memory techniques using real acoustic data collected from a tank and a lake. They find that the deep learning technique demonstrates better modeling performance than classical ML methods. The use of GPR for sound field reconstruction is examined in [102]. Although Table 3.1 summarizes the applicability of the physics-based modeling technique based on frequency and water depth, the choice of the appropriate modeling technique to use is often determined by experience and may be heuristic and non-optimal. In [103], the authors utilize various classification algorithms, such as naive Bayes, support vector machines, decision trees and random forest, to find the optimal model threshold limits in water depth and frequency. Similarly, in [104], the authors employ a convolutional neural network classifier to select the most appropriate modeling technique based on SSP. ML techniques have been widely applied in underwater inverse problems [105]–[109]

3.2.2.2   Practical limitations

Since data-driven approaches only require acoustic measurements for training, they eliminate the need of having full and accurate prior environmental knowledge. However, there are very limited attempts in literature to model acoustic propagation using data-driven techniques [101]. The two key problems that limit their use in acoustic propagation modeling are the necessity of a large representative training dataset and the inability to extrapolate well [110]. For example, in [101], the authors train the designed ML networks to estimate an acoustic communication channel between a transmitter and a receiver using 57,800,000 training data. The cost of acoustic data acquisition is high, as the ocean environments are expensive to operate in. Most of ML studies in underwater acoustics tackle the data hungriness either by using data augmentation for image processing models [111], [112] or by generating synthetic training data from surrogate models [51], [104], [109], [113]. Unfortunately, such techniques can not solve data hungriness in propagation modeling problems. While data-driven ML techniques demonstrate great potential in modeling underwater acoustic propagation, we still need to explore other feasible alternatives to address these challenges.

3.2.3   Physics-informed data-driven models

3.2.3.1   Related works

Combining physics-based modeling techniques and data-driven techniques to leverage the complementary strengths of both of them could potentially solve the dichotomy. The need to combine knowledge of physics with data-driven
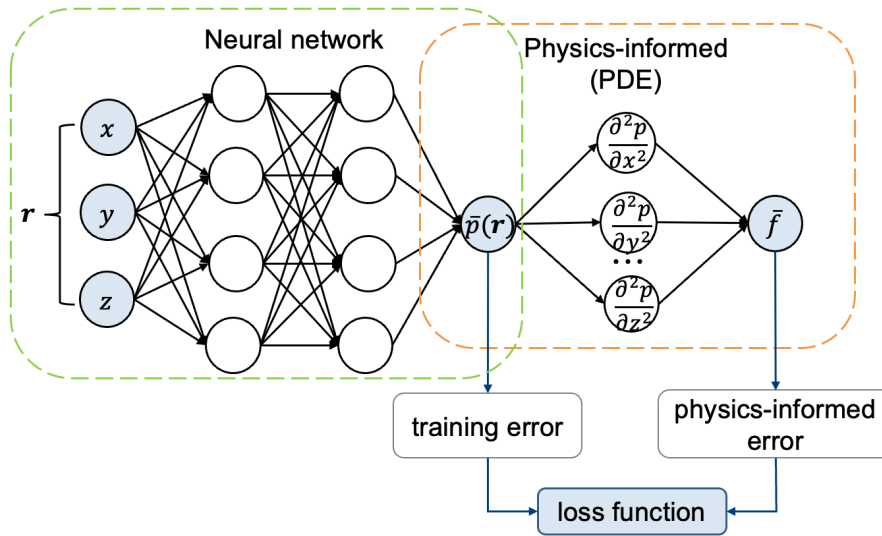
Figure 3.8: A typical model structure in PINNs.

ML is not limited to ocean acoustic modeling, and is in fact the focus of an upcoming area called SciML [114]. Researchers have explored synergistic ways that use scientific domain knowledge to aid data-driven ML [115]–[120]. Data-driven models are trained to learn from scientific data while respecting certain constraints imposed by our domain knowledge, therefore requiring much fewer training data than standard data-driven models. A popular SciML strategy, named physics-informed neural networks (PINNs), imposes physics constraints in the form of partial differential equations (PDEs) to act as regularizers in the loss function of a standard neural network (NN) [121]. Such an augmentation in the loss function helps to alleviate the problems of requiring a large amount of data and the inability to extrapolate. Fig. 3.8 shows a typical structure of PINNs.

In the context of acoustic propagation, NNs can be informed by the acoustic wave equation to generate data-efficient solution approximations. In [122], the

authors apply PINNs to predict sound propagation in an atmospheric boundary layer. The proper orthogonal decomposition based ML model is capable to model rough transmission loss fairly well, but fails to provide accurate estimations of complex pressure fields. This work concludes that it is challenging for both classical ML techniques and PINN-based models to handle spatially complicated complex acoustic pressure fields. In [123], the authors successfully apply PINNs to predict 1D sound fields with parameterized moving Gaussian sources and impedance boundaries. In the field of medical ultrasound, simulation results in [124] demonstrate that 2D acoustic field predictions made by PINN-based methods can be roughly two times faster as compared to finite difference methods. The authors of [125] adopt PINNs to solve the 2D wave equation and propose a curriculum learning based strategy to improve the convergence rate. Their model generalizes over initial source locations to eliminate the need of retraining the network. PINNs not only can solve forward problems, but also inverse problems [126].

The works reviewed above are not specific to ocean acoustics, and as far as we are aware, there are limited attempts at exploring the use of SciML for ocean modeling. One of the few works that assess the effectiveness of PINNs in solving simple ocean-related modeling problems is [127]. Although there are many studies showing that imposing physics knowledge improves model training, the authors of [127] find that adding extra physics-informed constraints in the loss function does not benefit overall performance and generalizability of NNs in their case studies. We implement a basic PINN model to predict acoustic fields in a simulated 2D underwater environment for validation. Our simulation

result supports this observation as well. The authors of [128] investigate benefits of using PINNs to solve three ocean modeling-related PDEs, including the wave equation. They also study how weightings of data error and physical constraints in loss functions affect training performance. The authors conclude that additional physical constraints in augmented loss functions bring more benefits to small datasets.

3.2.3.2 Discussion

PINNs encode underlying physics in the form of PDEs to have augmented loss functions, and strike a balance between data-driven and physics-informed through hyper-parameters that control weights of various loss terms. However, optimally tuning all hyper-parameters in PINN models and always having strong PDE constraints are difficult. On the other hand, PINNs are fundamentally NNs. Augmenting loss functions do not reduce the number of NN parameters to be trained. These possibly limit the practical success of PINN-based acoustic propagation modeling approaches in literature.

Each of the PINN technique and the proposed hybrid modeling recipe has its strong points. We do not intend to claim that the modeling recipe proposed in this thesis has an overwhelming superiority over PINN models. Instead, we aim to come up with a feasible modeling alternative and show its applicability through various scenarios in detail, providing users a new SciML strategy and allowing them to choose the one that fits their applications the most.

3.3 Underwater acoustic path planning of AUVs

AUVs are increasingly popular over the years to probe underwater environments. They can operate in harsh environments, reach deep depths and provide good long-term durability which human divers are incapable of [129]. The AUVs can do path planning through sonar detections (we name them as *sonar-based problems*) for missions such as obstacle & collision avoidance [130]–[133] and target tracking & classification [134],[135]. However, it is more common today to plan their paths in light of underwater acoustic propagation (we name them as *modeling-based problems*) due to the fact that underwater navigation and communication performance are highly variable and depend on acoustic propagation modeling. State-of-the-art underwater path planning algorithms are extensively reviewed in [136]–[138].

The modeling-based path planning is valuable for various purposes, including adaptive sampling [139]–[141], communication & navigation [142],[143] and acoustic search [144]. The adaptive sampling of acoustic fields or environments is to find the most informative locations that are worth measuring the next. Underwater communication and navigation performance of AUVs is highly variable due to complicated acoustic propagation phenomena. Planning paths to maintain reliable communication and navigation performance is practically useful. Path planning for acoustic search aims to optimally plan AUVs' paths to timely and accurately locate acoustic targets. This is important in underwater search & rescue missions.

The sonar-based online path planning in unknown underwater environments

for collision & obstacle avoidance has many successful attempts [145]–[148]. However, significant environmental uncertainties make modeling-based path planning problems extremely challenging. Environmental modeling and path search are two main steps in modeling-based path planning problems [136]. If operating environments are well understood, it is straightforward to plan trajectories of AUVs through methods such as data assimilation [149] (e.g., genetic algorithm [144]) with the aid of conventional propagation models [150]. In practice, the requirement of having accurate environmental knowledge in order to use conventional propagation models is often impractical. As a feasible alternative, GPR can estimate acoustic fields in unknown environments for modeling-based problems [102]. It is especially useful in adaptive sampling problems to determine optimal sampling locations using information theory metrics such as maximum entropy [151] and mutual information [152]. GPR models can also be applied to cooperatively plan optimal trajectories among multiple AUVs [153]. As discussed in Section 3.2.2, modeling acoustic fields through data-driven techniques requires a large number of acoustic observations across operating environments, making the modeling-based path planning extremely inefficient in terms of time and implementation complexity.

As far as we are aware, effective environmental modeling for modeling-based problems in unknown environments remains challenging. Our proposed modeling recipe is data-aided, thus capable of incorporating new observations to fine-tune the trained model to continuously improve prediction accuracy. It offers a promising and data-efficient modeling alternative in fully or partially unknown underwater environments for modeling-based path planning problems.

3.4 Summary

We briefly explained some preliminary concepts in underwater acoustics and surveyed underwater acoustic path planning, implicitly showing how challenging it is to model acoustic propagation in practical underwater environments. We also reviewed state-of-the-art acoustic propagation modeling techniques and outlined their practical limitations. Physics-based models require accurate environmental knowledge beforehand. Such a requirement can be eliminated by data-driven techniques at the cost of using extensive acoustic observations. The emergence of SciML offers a new perspective to address the limitations that are inherent to physics-based models and data-driven models. Modeling underwater acoustic propagation using SciML through PINNs, while showing great potential, has very limited success in practice. This research gap in the domain of underwater acoustic propagation modeling motivates us to bridge the gap in this thesis. We will come up with a new SciML strategy that is structurally different from PINNs to effectively model acoustic propagation in an underwater environment in later chapters. We will demonstrate the proposed modeling recipe based on the ray theory and the normal mode theory in Chapter 4 and Chapter 6 respectively.

Chapter 4

Ray-based Data-aided Propagation Modeling

The idea of embedding scientific domain knowledge of acoustic propagation into data-driven ML leverages the complementary strengths of data-driven ML and underlying physics. It thus has the potential to yield a data-efficient and well-generalized propagation modeling recipe. As reviewed in Chapter 3, PINNs encode physics to augment loss functions. However, there are limited attempts in practically modeling underwater acoustic propagation using PINNs.

How to effectively model high-frequency acoustic propagation in underwater environments under partial environmental information using limited acoustic measurements is the focus of this chapter. Instead of using PINNs, we employ a new approach to design a class of ML algorithms where the physics is encoded in the structure of the algorithms. The functions these algorithms learn are automatically solutions to the acoustic wave equation. We give up the universal approximation property of NNs, and constrain our algorithms to only learn physically realistic functions. This constraint enables us to learn from very little data, and to extrapolate beyond the region where the data are collected. The work presented in this chapter is published in [154] and [155].

4.1 Problem formulation

We assume that an acoustic source locates at $\boldsymbol{r}_s$ and transmits a continuous wave (CW) signal at frequency f in an underwater environment. The acoustic signals emitted from the source interact with the water surface, bottom and other surrounding boundaries as they propagate in an underwater acoustic channel. The pressure amplitude $\bar{p}(\boldsymbol{r})$ received at location $\boldsymbol{r}$ is composed of a set of multipath arrivals, each of them has an associated intensity, phase and arrival time. The multipath arrivals interfere with each other constructively and destructively, leading to spatial variation of acoustic fields across the underwater environment. Considering a high-frequency point source, we aim to effectively model acoustic propagation (or equivalently predict received acoustic signals) in the desired number of dimensions using limited environmental knowledge and a small amount of acoustic data collected within an area of interest (AOI).

4.2 Ray basis neural network framework

The acoustic wave equation determines the propagation of acoustic energy from the source, and is expressed as [29]:

$$\frac{\partial^2 p}{\partial t^2} = c^2 \nabla^2 p, \tag{4.1}$$

where p represents acoustic pressure, t denotes time and c is the sound speed, ∇^2 is the Laplace operator. Assuming a harmonic wave field, a solution to (4.1) can be written as:

$$p(\boldsymbol{r}, t) = \bar{p}(\boldsymbol{r})e^{i\omega t}, \tag{4.2}$$

where $\boldsymbol{r}$ is the spatial coordinate, $\bar{p}(\boldsymbol{r})$ represents complex pressure amplitude, and $\omega = 2\pi f$ denotes angular frequency. Substituting (4.2) back into (4.1) and rearranging, we get the Helmholtz equation [29]:

$$k^2 \bar{p}(\boldsymbol{r}) + \nabla^2 \bar{p}(\boldsymbol{r}) = 0, \tag{4.3}$$

where $k = \frac{\omega}{c}$ is called the wavenumber. Equation (4.3) can be solved by:

$$\bar{p}(\boldsymbol{r}) = A e^{i\phi} e^{i\boldsymbol{k}\cdot\boldsymbol{r}}, \tag{4.4}$$

where A and ϕ represent the amplitude and phase of a wave, and $\boldsymbol{k}$ is wave propagation vector that satisfies:

$$\|\boldsymbol{k}\|_2 = k. \tag{4.5}$$

Any function of the form (4.4) solves the acoustic wave equation. Due to the linearity of the acoustic wave equation, the superposition of n_{ray} such functions must also be a solution to the acoustic wave equation. Thus, the field at a location $\boldsymbol{r}$ can be expressed as the sum of terms given by (4.4):

$$\bar{p}(\boldsymbol{r}) = \sum_{m=1}^{n_{\mathrm{ray}}} A_m e^{i\phi_m} e^{i\boldsymbol{k}_m\cdot\boldsymbol{r}}, \tag{4.6}$$

where A_m denotes the amplitude of mth arrival, ϕ_m refers to the corresponding phase term, and $\boldsymbol{k}_m = k\hat{\boldsymbol{k}}_m$ for some unit vector $\hat{\boldsymbol{k}}_m$.

This is the well-known ray solution to the acoustic wave equation [30], with
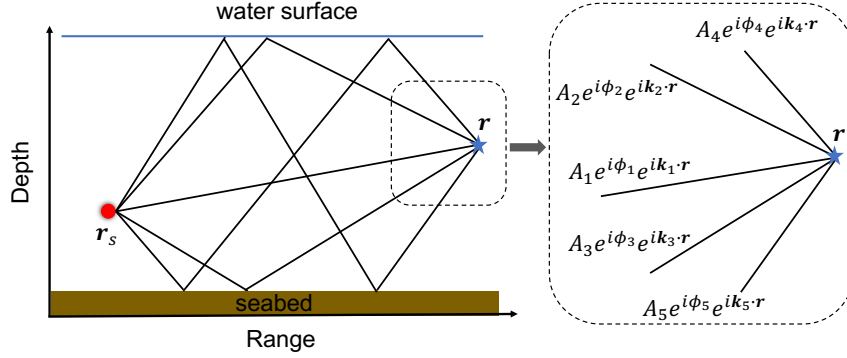
Figure 4.1: An example showing the superposition of 5 multipath arrivals at a receiver location in a typical ocean environment.

$A_m e^{i\phi_m}$ being the complex amplitude of the mth ray and $\hat{\boldsymbol{k}}_m$ being the direction of travel of that ray. Fig. 4.1 elaborates the intuition behind (4.6) from a receiver point of view. The acoustic field at a receiver location $\boldsymbol{r}$ can be visualized as the superposition of n_{ray} multipath arrivals. Conventional ray models determine A_m, ϕ_m and $\boldsymbol{k}_m$ for all m, given detailed environmental knowledge. It is not generally possible to compute A_m, ϕ_m and $\boldsymbol{k}_m$ if partial or no environmental knowledge is available. Fortunately, ML provides us the necessary tools to learn the unknown parameters or functions from data. We can think of (4.6) as a function to be modeled using a specialized NN with each term in the summation playing the role of a neuron (with parameters closely related to A_m, ϕ_m and $\boldsymbol{k}_m$). The values of the parameters can be learnt from data using a generalized *backpropagation* algorithm [156] with automatic differentiation [157] applied to this NN, such as ADAM [158].

The functions that this NN can learn are guaranteed to solve the acoustic wave equation (4.1) by construction, hence incorporating the acoustic domain knowledge in the structure of the NN. We term this specialized NN as a *ray basis*
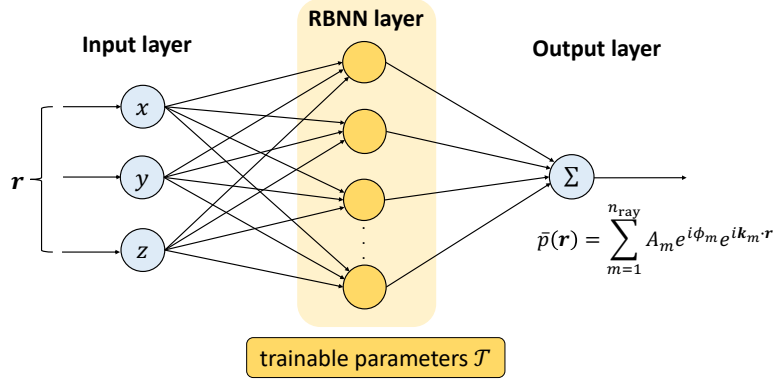
Figure 4.2: The computation graph for (4.6) illustrating the proposed RBNN framework. $\mathcal{T}$ contains unknown model parameters whose values are learnt during the training.

neural network (RBNN), as the neurons in the network can be interpreted as acoustic rays arriving at a given receiver location as shown in Fig. 4.2.

It is worth noting that our model structure is determined based on the governing physics and is conceptually different from a conventional PINN. Instead of imposing physical constraints in the loss function of a standard NN, we embed the constraints in the structure of the NN by making each neuron individually obey the governing physics. We then borrow the training strategies from a standard NN to find the best-fitting values of the unknown parameters of the resulting model by continuously minimizing a loss function that measures the error between the model output and observed data. The dataset used in model training stage is comprised of a set of measurement locations $\boldsymbol{r}_{\text{train}} = \left[\boldsymbol{r}_{\text{train}}^1, \boldsymbol{r}_{\text{train}}^2, \boldsymbol{r}_{\text{train}}^3, ...\right]$ and corresponding acoustic field measurements $\boldsymbol{y}_{\text{train}} = \left[y_{\text{train}}^1, y_{\text{train}}^2, y_{\text{train}}^3, ...\right]$. Furthermore, one can construct more sophisticated NNs with a mix of standard neurons and RBNN-neurons, as we shall show later. Such NNs can be useful in solving problems with partial environmental knowledge.

The formulation presented above forms a basic recipe to model high-frequency acoustic propagation using the SciML methodology. The exact calculations of A_m, ϕ_m and $\boldsymbol{k}_m$ of each ray are application-dependent, since some of these terms may be calculated based on environmental knowledge, and others determined from parameters learned from data. In Sections 4.2.1 and 4.2.2, we apply the recipe to generate models to handle three different application scenarios: plane wave (far-field propagation), spherical wave (near-field propagation) without knowledge of geometry, and spherical wave with knowledge of geometry. In each scenario, the exact details of RBNN-neurons change, but the overall RBNN structure and the training process remain the same.

4.2.1 Plane wave RBNN

In the far-field of a point source, a ray arrival can be well approximated by a planar wavefront. So, if the AOI is sufficiently far from the source, we can use a plane wave formulation for the unknowns in (4.6). This formulation does not require any prior environmental knowledge, and is particularly helpful to model practical scenarios where the environment is largely unknown. The unknown terms A_m and ϕ_m are treated as unknown model parameters to be determined during training. If the sound speed or frequency is unknown, k may also be treated as an unknown parameter. The 3D unit vector $\hat{\boldsymbol{k}}_m$ is parametrized in terms of azimuthal angle θ_m and elevation angle ψ_m:

$$
\hat{\boldsymbol{k}}_m = \begin{bmatrix} \cos(\theta_m) \, \sin(\psi_m) \\ \sin(\theta_m) \, \sin(\psi_m) \\ \cos(\psi_m) \end{bmatrix}.
\tag{4.7}
$$

The set of trainable RBNN model parameters in the plane wave formulation therefore is:

$$\mathcal{T}_{\mathrm{p}} \equiv \left(\boldsymbol{A}, \boldsymbol{\phi}, k, \boldsymbol{\theta}, \boldsymbol{\psi}\right), \tag{4.8}$$

where $\boldsymbol{A} = \left[A_1, A_2, \ldots, A_{n_{\mathrm{ray}}}\right]$, $\boldsymbol{\phi} = \left[\phi_1, \phi_2, \ldots, \phi_{n_{\mathrm{ray}}}\right]$, $\boldsymbol{\theta} = \left[\theta_1, \theta_2, \ldots, \theta_{n_{\mathrm{ray}}}\right]$ and $\boldsymbol{\psi} = \left[\psi_1, \psi_2, \ldots, \psi_{n_{\mathrm{ray}}}\right]$. The absolute pressure amplitude $\hat{p}$ predicted at location $\boldsymbol{r}$ can be expressed as:

$$\hat{p}(\boldsymbol{r}) = \left| \sum_{m=1}^{n_{\mathrm{ray}}} A_m e^{i\phi_m} e^{i\boldsymbol{k}_m \cdot \boldsymbol{r}} \right|. \tag{4.9}$$

Since we do not assume detailed environmental information, the number of rays n_{ray} is unknown, but a conservative upper bound can often be estimated. Nevertheless, we find it better to think of n_{ray} as a model hyper-parameter to be tuned during training, with the tuning guided by an estimate, if available. Due to the strongly non-linear effect of parameters θ_m and ψ_m, the RBNN may get trapped in local minima or saddle points during training if n_{ray} is small. A large n_{ray} and uniformly distributed random initialization of $\boldsymbol{\theta}$ and $\boldsymbol{\psi}$ ensure better convergence, but create potential for overfitting. A L_1-norm regularization on parameters $\boldsymbol{A}$ encourages sparsity, i.e., a trained model with only a small number of rays, and therefore avoids overfitting.

The loss function we minimize during the training is therefore the sum-square difference between predicted and measured pressure amplitudes at given receiver locations, combined with the L_1-norm regularization term to encourage sparsity:

$$L_{\mathrm{p}}(\boldsymbol{r}, y; \mathcal{T}_{\mathrm{p}}) = |\hat{p}(\boldsymbol{r}; \mathcal{T}_{\mathrm{p}}) - y|^2 + \alpha \left\| \boldsymbol{A} \right\|_1, \tag{4.10}$$

where $\hat{p}(\boldsymbol{r}; \mathcal{T}_{\mathrm{p}})$ is the absolute pressure amplitude predicted by our model using the set of trainable parameters $\mathcal{T}_{\mathrm{p}}$, y is the observed pressure amplitude at location $\boldsymbol{r}$, and α is a hyper-parameter that controls the regularization. While we write (4.10) for a single training data point, it is usually summed over a training mini-batch as per the standard practice in ML [159]. During validation and model evaluation, α is set to 0.

4.2.2   Spherical wave RBNN

The acoustic propagation near a point source is best modeled using spherical waves. In a typical ocean environment, there are three key factors that contribute to the overall transmission loss: geometric spreading loss l_{g}, volume absorption loss l_{a} and reflection loss l_{rc} (net effect from all reflecting boundaries). In contrast to the plane wave formulation, the amplitude A and phase ϕ of an arrival ray in our spherical wave formulation are functions of both source location $\boldsymbol{r}_{\mathrm{s}}$ and receiver location $\boldsymbol{r}$. Therefore, (4.6) is re-written as:

$$\bar{p}(\boldsymbol{r}) = \sum_{m=1}^{n_{\mathrm{ray}}} A_m(\boldsymbol{r}_{\mathrm{s}}, \boldsymbol{r}) e^{i\phi_m(\boldsymbol{r}_{\mathrm{s}}, \boldsymbol{r})}, \tag{4.11}$$

where

$$A_m(\boldsymbol{r}_{\mathrm{s}}, \boldsymbol{r}) = l_{\mathrm{g}}^m(\boldsymbol{r}_{\mathrm{s}}, \boldsymbol{r}) l_{\mathrm{rc}}^m(\boldsymbol{r}_{\mathrm{s}}, \boldsymbol{r}) l_{\mathrm{a}}^m(\boldsymbol{r}_{\mathrm{s}}, \boldsymbol{r}), \tag{4.12a}$$

$$\phi_m(\boldsymbol{r}_{\mathrm{s}}, \boldsymbol{r}) = \phi_{\mathrm{rc}}^m(\boldsymbol{r}_{\mathrm{s}}, \boldsymbol{r}) + k\bar{d}_m(\boldsymbol{r}_{\mathrm{s}}, \boldsymbol{r}). \tag{4.12b}$$

Here, $\phi_{\mathrm{rc}}^m(\boldsymbol{r}_{\mathrm{s}}, \boldsymbol{r})$ is the overall reflection phase shift along the trajectory of the mth ray, and $k\bar{d}_m(\boldsymbol{r}_{\mathrm{s}}, \boldsymbol{r})$ corresponds to the phase change for a propagation distance

of $\bar{d}_m(\boldsymbol{r}_\mathrm{s}, \boldsymbol{r})$. The spherical geometric spreading loss is [64]:

$$l_\mathrm{g}^m(\boldsymbol{r}_\mathrm{s}, \boldsymbol{r}) = \frac{1}{\bar{d}_m(\boldsymbol{r}_\mathrm{s}, \boldsymbol{r})}. \qquad (4.13)$$

The volume absorption loss generally depends on the operating frequency, propagation distance and characteristics of the propagating medium. The widely used simplified expression of the attenuation per unit distance due to volume absorption is given in [160]. The attenuation and phase shift when sound interacts with scattering boundaries (e.g., seabed) can also be calculated if we know the angle of interaction and the properties and structure of the boundary [68].

The spherical wave formulation can incorporate varying degrees of environmental knowledge. The model parameters involved in the field prediction can be found through either data-driven learning strategies or numerical calculations, depending on the environmental knowledge provided. We next illustrate two examples that correspond to the scenarios with and without knowledge of the channel geometry.

4.2.2.1 Without knowledge of channel geometry

For scenarios where the channel geometry is largely unknown, trajectories of rays from the source to the receiver are unknown. However, by applying the image source method (ISM) [161] to the problem, we can replace the unknown source location and channel geometry with a set of unknown image sources as illustrated in Fig. 4.3. The problem is then transformed into finding the parameters of the unknown image sources to match with the training data.
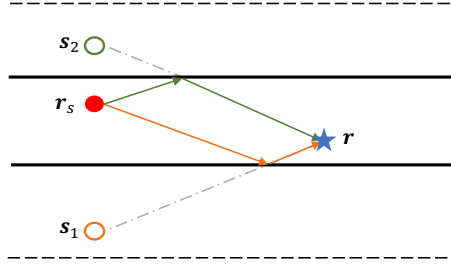
Figure 4.3: An illustration showing two image sources corresponding to two reflected ray paths between the source and the receiver.

Let $\boldsymbol{r}_o$ be an arbitrary reference position within the environment. We can parametrize each image source by a pressure amplitude A_m, phase ϕ_m, a direction vector (corresponding to azimuthal angle θ_m and elevation angle ψ_m) and distance d_m from this reference position. In the case of an isovelocity environment, the absolute pressure amplitude at a receiver $\boldsymbol{r}$ is then given by:

$$\hat{p}(\boldsymbol{r}) = \left| \sum_{m=1}^{n_{\mathrm{ray}}} A_m \frac{l_{\mathrm{a}}(\|\boldsymbol{s}_m - \boldsymbol{r}\|_2)}{\|\boldsymbol{s}_m - \boldsymbol{r}\|_2} e^{i(\phi_m + k\|\boldsymbol{s}_m - \boldsymbol{r}\|_2)} \right|, \tag{4.14}$$

where

$$\boldsymbol{s}_m = \boldsymbol{r}_o - d_m \begin{bmatrix} \cos(\theta_m) \, \sin(\psi_m) \\ \sin(\theta_m) \, \sin(\psi_m) \\ \cos(\psi_m) \end{bmatrix}, \tag{4.15}$$

and $l_{\mathrm{a}}(\cdot)$ is attenuation due to volume absorption as given in [160]. The complete set of trainable parameters for this model are:

$$\mathcal{T}_{\mathrm{s}} \equiv (k, \boldsymbol{\theta}, \boldsymbol{\psi}, \boldsymbol{d}, \boldsymbol{A}, \boldsymbol{\phi}), \tag{4.16}$$

where $\boldsymbol{d} = [d_1, d_2, \ldots, d_{n_{\mathrm{ray}}}]$ contains distances between reference location and image sources. The loss function to be minimized is identical to (4.10).

4.2.2.2 With knowledge of channel geometry

If the channel geometry and associated reflecting boundaries are partially or completely known, we can incorporate available knowledge into our model. To illustrate the idea, let us assume that we know the source location and the channel geometry. We also assume that the sea surface is modeled well as a pressure-release boundary, but that we do not know the reflection coefficient for the seabed.

We can model the acoustic waves scattered from boundaries as reflection coefficients. Given the source location and channel geometry, we can compute the incidence angle γ_m for each ray at the seabed. The reflection coefficient of the seabed is an unknown function of incidence angle, and may be modeled using a simple 1-input 2-output (magnitude and phase) feedforward NN with a single hidden layer. We call this NN as the *reflection coefficient neural network* (RCNN). The same reflection coefficient function applies to all rays incident on the seabed, and hence the RCNN weights are shared across all the rays. The RCNN is implemented as an additional layer in the RBNN framework with shared weights, as illustrated in Fig. 4.4.

A ray may experience more than one reflections at the seabed. The overall reflection coefficient for m^{th} arrival ray is:

$$l_{\text{rc}}^m(\boldsymbol{r}) = \prod_{j=1}^{n_{\text{b}}^m} \text{RCNN}_\epsilon(\gamma_j^m(\boldsymbol{r})), \tag{4.17}$$

where n_{b}^m is the number of seabed reflections for ray m, $\gamma_j^m(\cdot)$ is the incidence angle for j^{th} seabed reflection, and $\text{RCNN}_\epsilon(\cdot)$ is the predicted reflection
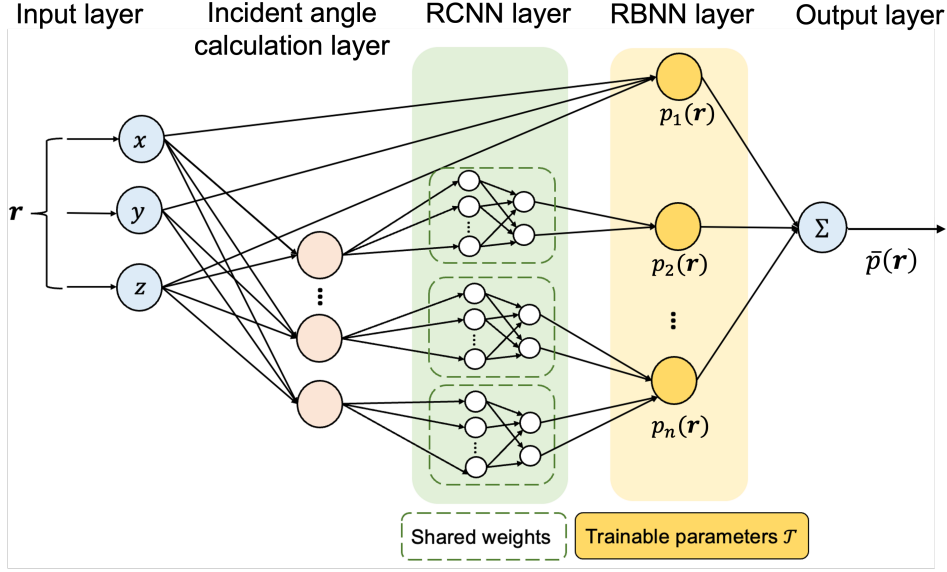
Figure 4.4: The computational graph for (4.19) can be modeled as an additional RCNN layer prior to the RBNN layer.

coefficient magnitude from the RCNN. The corresponding cumulative phase shift is:

$$\phi_{\text{rc}}^m(\boldsymbol{r}) = n_{\text{s}}^m \pi + \sum_{j=1}^{n_{\text{b}}^m} \text{RCNN}_\kappa(\gamma_j^m(\boldsymbol{r})), \qquad (4.18)$$

where $\text{RCNN}_\kappa(\cdot)$ is the reflection phase shift predicted by the RCNN, and n_{s}^m is the number of surface reflections for ray m. The phase change $n_{\text{s}}^m \pi$ is due to the pressure-release boundary assumption, and can easily be replaced by a more sophisticated surface reflection model, if desired.

As in the previous section, we choose to apply the ISM to replace the source with multiple image sources. This allows us to work with approximate knowledge of channel geometry and learn the exact locations of the image sources from data, as we illustrate later in this section. The resultant absolute pressure amplitude

can be expressed as:

$$\hat{p}(\boldsymbol{r}) = \left| \sum_{m=1}^{n_{\text{ray}}} \frac{l_{\text{rc}}^m(\boldsymbol{r}) l_{\text{a}}(\|\boldsymbol{s}_m - \boldsymbol{r}\|_2)}{\|\boldsymbol{s}_m - \boldsymbol{r}\|_2} e^{i(\phi_{\text{rc}}^m(\boldsymbol{r}) + k\|\boldsymbol{s}_m - \boldsymbol{r}\|_2)} \right|, \qquad (4.19)$$

where the ray trajectory necessary for the evaluation of $l_{\text{rc}}^m(\cdot)$ can be computed

by geometric ray tracing [162]. Since we are using a ray tracing model, the recipe

also works with non-isovelocity SSP by changing the euclidean distances term

$\|\boldsymbol{s}_m - \boldsymbol{r}\|_2$ in (4.19) to actual propagation distances along curved ray paths.

The overall computation graph for (4.19) can be viewed as a NN with

geometric ray tracer, RCNN layer, and RBNN layer as shown in Fig. 4.4. The

set of trainable RBNN parameters in this model are:

$$\mathcal{T}_{\text{sg}} \equiv (k, \boldsymbol{\theta}, \boldsymbol{\psi}, \boldsymbol{d}, \boldsymbol{R}), \qquad (4.20)$$

where $\boldsymbol{R}$ represents all trainable parameters in the RCNN layer.

The search spaces for $\boldsymbol{\theta}$ and $\boldsymbol{\psi}$ span $[0, 2\pi)$, and for $\boldsymbol{d}$ spans $[0, \infty)$. The

knowledge of geometry and the source location allows us to pre-calculate nominal

arrival ray directions $\boldsymbol{\theta}'$, $\boldsymbol{\psi}'$ and propagation distances $\boldsymbol{d}'$ prior to the model

training stage. The calculated nominal directions and distances may deviate

from reality due to limited knowledge or measurement error. We model this

with appropriate error terms $\boldsymbol{e}_\theta$, $\boldsymbol{e}_\psi$ and $\boldsymbol{e}_d$:

$$\boldsymbol{\theta} = \boldsymbol{\theta}' + \boldsymbol{e}_\theta, \tag{4.21a}$$

$$\boldsymbol{\psi} = \boldsymbol{\psi}' + \boldsymbol{e}_\psi, \tag{4.21b}$$

$$\boldsymbol{d} = \boldsymbol{d}' + \boldsymbol{e}_d. \tag{4.21c}$$

We then replace the trainable parameters $\boldsymbol{\theta}$, $\boldsymbol{\psi}$, and $\boldsymbol{d}$ with the corresponding error terms, thus replacing (4.20) with:

$$\mathcal{T}_{\text{sg}} \equiv (k, \boldsymbol{e}_\theta, \boldsymbol{e}_\psi, \boldsymbol{e}_d, \boldsymbol{R}) . \tag{4.22}$$

The amount of errors allowed in $\boldsymbol{e}_\theta$, $\boldsymbol{e}_\psi$ and $\boldsymbol{e}_d$ reflect how confident we are about our knowledge of the channel geometry and source location. We impose L_2-norm penalty terms in the loss function to constrain values of $\boldsymbol{e}_\theta$, $\boldsymbol{e}_\psi$ and $\boldsymbol{e}_d$ learnt during the training process. We also add a harsh penalty term to ensure that the reflection model learnt by the RCNN obeys energy conservation*. The resulting loss function is:

$$L_{\text{sg}}(\boldsymbol{r}, y; \mathcal{T}_{\text{sg}}) = |\hat{p}(\boldsymbol{r}; \mathcal{T}_{\text{sg}}) - y|^2 + \left\| \boldsymbol{\zeta} \sqrt{\boldsymbol{e}_\theta{}^2 + \boldsymbol{e}_\psi{}^2} \right\|_2$$
$$+ \beta \left\| \boldsymbol{e}_d \right\|_2 + \chi \max \left\{ 0, \int_0^{0.5\pi} \epsilon(\gamma)^2 d\gamma - 1 \right\}, \quad (4.23)$$

where $\boldsymbol{\zeta}$, β and χ are hyper-parameters related to the three penalty terms. All elements in the hyper-parameters are set to 0 during the validation and

---

*This is the upper bound for reflected energy in lossy environments.
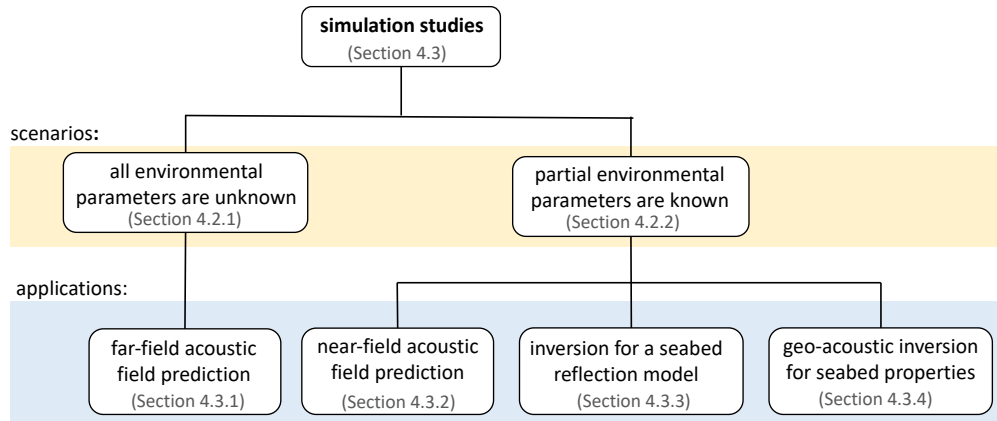
Figure 4.5: Summary of the application scenarios demonstrated via simulation studies.

model evaluation. In general, the image sources corresponding to higher-order reflections are assigned smaller penalty coefficients as angular errors are amplified with an increasing number of reflections.

4.3   Simulation studies

To study the effectiveness of our proposed method, we consider four common applications of ocean acoustic propagation models. These are summarized in Fig. 4.5.

All four applications consider using a profiling float equipped with a single hydrophone, collecting acoustic field measurements at a constant sampling rate. Such floats provide a cost-effective way of sparsely sampling acoustic fields. We assume that the profiling float can control its motion vertically, but not horizontally. The float freely drifts horizontally with ocean currents, thus following a zig-zag trajectory as it moves up and down through the water column.

TABLE 4.1: Simulated environmental setup for the far-field acoustic field prediction application.

Parameters	Value
Environmental model	2D
Frequency	10 kHz
Seabed	Sandy clay
Bathymetry	Range-dependent
Source depth	5 m
Sound speed	1,541 m/s
Distance between source and AOI	995 m
Dimensions of AOI	50 m × 30 m
Number of training data	688
Number of validation data	296
Number of test data	601,601
Number of rays in the RBNN layer	60

4.3.1 Far-field acoustic field prediction

The first application we shall consider is that of acoustic field prediction within an AOI at a long distance from an acoustic source. Suppose we have acoustic measurements from a profiling float along a zig-zag trajectory through the AOI, but no other environmental knowledge. Conventional propagation models cannot be used for this application, as they require environmental knowledge as input. As discussed in Section 4.2.1, RBNN parameters $\mathcal{T}_{\mathrm{p}}$ can be learnt without prior environmental knowledge, with acoustic field measurements at a few points as training data. With a sufficiently large distance between the acoustic source and the AOI, the plane wave RBNN formulation may be used to approximate the acoustic propagation in the AOI.

We simulate a profiling float performing 17 profiles through a 50 m × 30 m

71
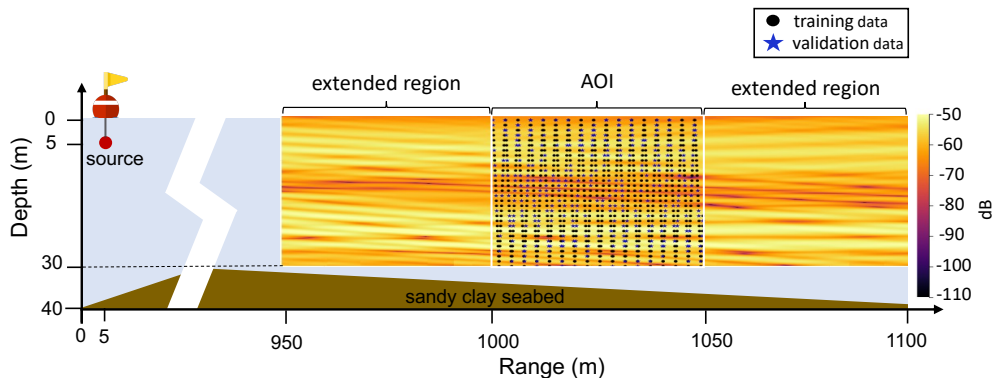
Figure 4.6: Simulated environment for the far-field acoustic field prediction application. The trajectory of the profiling float can be seen in terms of the training data points. The ground truth field pattern within the AOI is also shown.

AOI at a distance of 995 m from a 10 kHz source deployed at a depth of 5 m. The simulation setup is detailed in Table 4.1 and illustrated in Fig. 4.6. A total of 984 acoustic field measurements are collected along the trajectory of the float, of which 70% are used to train the RBNN model, and the remaining 30% are used for validation. The training data train trainable parameters $\mathcal{T}$, while the validation data are used to implement early stopping to avoid over-fitting. We wish to predict acoustic fields in the entire AOI.

We benchmark the field prediction performance of the RBNN against two popular data-driven techniques: GPR and DNN. We use a GPR with a composite kernel of a squared exponential isotropic kernel and a Matérn 5/2 ARD kernel, as this is a common choice for multi-dimensional regression problems. The DNN model used has three fully-connected hidden layers with rectified linear unit (ReLU) as the activate function.

We use the Bellhop propagation model [61] to generate 984 synthetic acoustic measurements along the profiler's trajectory for training and validation. The

(a) Ground truth field within the AOI

(b) Ground truth field in an extended region

(c) RBNN field estimate within the AOI

(d) GPR field estimate within the AOI

(e) DNN field estimate within the AOI

(f) RBNN extrapolated field estimate

(g) GPR extrapolated field estimate

(h) DNN extrapolated field estimate

(i) RBNN field estimate with position error

(j) GPR field estimate with position error

(k) DNN field estimate with position error

Figure 4.7: The estimated field patterns for the far-field acoustic field prediction application. Panel (a) shows the ground truth field pattern within the AOI, while panel (b) shows the ground truth field within a 50 m extended area on both sides of the AOI. Panels (c)–(e) show the estimated fields by RBNN, GPR and DNN. Panels (f)–(h) show the corresponding extrapolated field by RBNN, GPR and DNN in the extended region. Panels (i)–(k) show the estimated field when the training data has positional errors.

TABLE 4.2: Model complexity and RMS test error of the three models for field predictions within the AOI.

Method	Number of model parameters	RMS test error (dB)	
		Error-free data	Noisy data
RBNN[1]	60	3.082	4.258
GPR	1374[2]	3.211	3.167
DNN	6421	3.488	3.372

[1] Plane-wave RBNN.
[2] Dimensionality of each data point $\times$ training data size.

high-frequency source produces a complex interference pattern. To evaluate the field prediction performance in simulation, we generate a dense test dataset of 601,601 data points over a grid covering the AOI, with a resolution of 0.05 m in depth and range. The trainable model parameters in RBNN and DNN models are randomly initialized. We therefore carry out 10 Monte Carlo simulations for the RBNN and DNN models and present the results with the best validation error. The hyper-parameters in the GPR kernel are chosen to yield the best performance based on the validation data. We also add a random position error of up to 0.1 m on each dimension of the measurement locations of the training and validation data to evaluate model robustness.

The RMS test error and the model complexity (number of model parameters) of the three models are reported in Table 4.2. The acoustic field patterns estimated by the three approaches are shown in Fig. 4.7. All three methods are able to learn key features of the acoustic fields within the AOI. The RBNN model recovers most of the details in the AOI and extrapolates well in an *extended region* beyond the AOI. The GPR learns the field pattern well within the AOI where training data are available, but fails to extrapolate the field in the extended

region. The field pattern reconstructed by the DNN has the lowest fidelity among the three approaches. The extrapolated field by the DNN also deviates significantly from the ground truth. The extrapolated field patterns shown in Fig. 4.7 (f), (g) and (h) highlight the unique ability of the RBNN to not only interpolate well, but also to extrapolate.

The field prediction performance of the GPR and the DNN, as quantified by the RMS test error, is not significantly affected by position errors in the dataset. On the other hand, the field prediction accuracy of the plane wave RBNN is found to be vulnerable to position errors. Interestingly though, the qualitative field patterns seen in Fig. 4.7 (i), (j) and (k) show that the RBNN captures the overall field pattern the best, even in the case of position errors.

4.3.2 Near-field acoustic field prediction

We next consider an acoustic field prediction application within an AOI from a less distant source assuming that the channel geometry is known. Acoustic measurements are collected along a zig-zag trajectory within AOI using a profiling float. Since some of the environmental parameters (e.g., seabed properties) are unknown, we cannot employ conventional propagation models for field prediction. We can, however, use the spherical wave RBNN from Section 4.2.2.2 with the knowledge of channel geometry. We can calculate the nominal arrival ray directions $\boldsymbol{\theta}'$, $\boldsymbol{\psi}'$ and propagation distances $\boldsymbol{d}'$ prior to the training. This significantly improves the training effectiveness and accuracy.

For this application, we use a simple spherical wave RBNN model based on (4.19), without the RCNN layer. The overall effect of the reflections
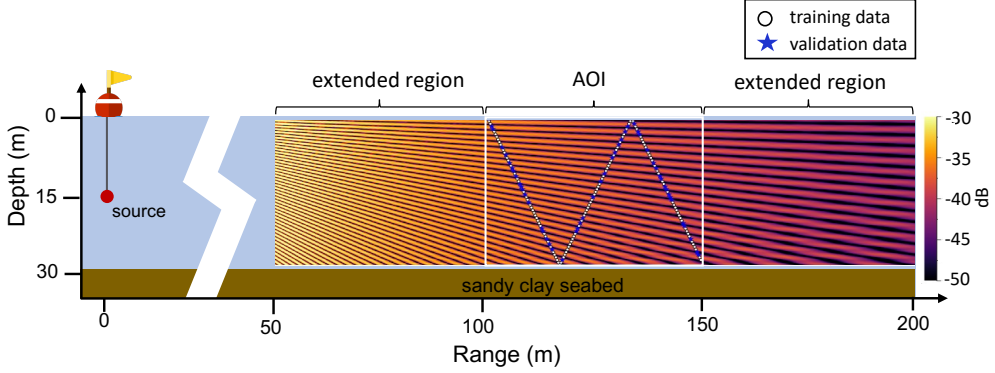
Figure 4.8: Simulated environment for the near-field acoustic field prediction application. The trajectory of the profiling float can be seen in terms of the training data points. The ground truth field pattern within the AOI is also shown.

and absorption is modeled with a set of trainable parameters $\boldsymbol{A}$, associated with the set of rays. To model geometrical measurement errors, we also add error parameters for nominal directions and propagation distances. The set of trainable parameters therefore is:

$$\mathcal{T}_{\mathrm{s}} \equiv (k, \boldsymbol{e}_{\theta}, \boldsymbol{e}_{\psi}, \boldsymbol{e}_d, \boldsymbol{A}, \boldsymbol{\phi}). \tag{4.24}$$

The setup of the simulated environment is shown in Fig. 4.8 and summarized in Table 4.3. A profiling float performs 2 profiles across a 50 m $\times$ 28 m AOI at a distance of 100 m from a 5 kHz source deployed at a depth of 15 m to collect 167 acoustic field measurements. We use 70% of the collected measurements to train the RBNN, and aim to estimate the acoustic field in the entire AOI. We benchmark the field prediction performance of the RBNN against GPR and DNN with the same model configurations as discussed in Section 4.3.1.

A dense test dataset of 561,561 data points on a 0.05 m spacing grid covering

TABLE 4.3: Simulated environmental setup for the near-field acoustic field prediction application.

Parameters	Value
Environmental model	3D
Frequency	5 kHz
Seabed	Sandy clay
Bathymetry	Range-independent
Water depth	30 m
Source depth	15 m
Sound speed	1,541 m/s
Distance between source and AOI	100 m
Dimension of AOI	50 m $\times$ 28 m $\times$ 0.1 m
Number of training data	116
Number of validation data	51
Number of test data	561,561
Number of rays in RBNN	60

the AOI is generated using Bellhop to evaluate the field prediction performance. As RBNN and DNN may be sensitive to random initialization, we carry out 10 Monte Carlo simulations for each, and present the results with the best validation error. The hyper-parameters in the GPR kernel are tuned to yield the best validation error. To evaluate model robustness, we added random measurement errors in the source location (0.3 m in horizontal directions, 0.1 m in depth), measurement locations (maximum of 0.4 m in all directions) and water depth (1 m) of AOI.

The RMS test errors of the estimated fields within the AOI by the three models are shown in Table 4.4. The acoustic field patterns within AOI estimated by the three approaches are shown in Fig. 4.9 (c), (d) and (e). Fig. 4.9 (f), (g) and (h) show extrapolated fields by the three models. The RBNN model is

(a) Ground truth field within AOI

(b) Ground truth field in an extended region

(c) RBNN field estimate within the AOI

(d) GPR field estimate within the AOI

(e) DNN field estimate within the AOI

(f) RBNN extrapolated field estimate

(g) GPR extrapolated field estimate

(h) DNN extrapolated field estimate

(i) RBNN field estimate with measurement error

(j) GPR field estimate with measurement error

(k) DNN field estimate with measurement error

Figure 4.9: The estimated field patterns for the near-field acoustic field prediction application. Panel (a) shows the ground truth field pattern within the AOI, while panel (b) shows the ground truth field within a 50 m extended area on both sides of the AOI. Panels (c)–(e) show the estimated fields by RBNN, GPR and DNN. Panels (f)–(h) show the corresponding extrapolated field by RBNN, GPR and DNN in the extended region. Panels (i)–(k) show the estimated field when the position and geometry measurements have random errors.

TABLE 4.4: RMS test error for the near-field acoustic field prediction application.

Method	RMS test error (dB)	
	Error-free data	Noisy data
RBNN	1.688	6.519
GPR	7.011	7.056
DNN	7.118	7.142

able to predict and extrapolate the spatially fast-varying field patterns well, even with a much smaller training data set as compared to the far-field acoustic field prediction application in the previous section. However, the GPR and DNN show poor performance in terms of the estimated field pattern and RMS test error, for both interpolation and extrapolation of the acoustic field. The results highlight the data-efficiency of the RBNN model–the model can effectively incorporate knowledge of channel geometry and therefore train with very little data. Conventional GPR and DNN models, on the other hand, fail to predict field patterns as they do not benefit from partial environmental knowledge.

As one would expect, measurement noise worsens the prediction accuracy for the RBNN model. The sensitivity of field prediction to position errors is summarized in Table 4.5. However, the qualitative field pattern can still be recovered even with large measurement errors as seen in Fig. 4.9 (i).

4.3.3 Inversion for a seabed reflection model

The third application we demonstrate is to extract a seabed reflection model from acoustic measurements. Seabed reflection depends on the seabed structure and material properties, which are often unknown. In applications where multipath

TABLE 4.5: Sensitivity of RMS test error of field prediction to random position error, for the near-field acoustic field prediction application.

Maximum position error[1](m)	RMS test error (dB)
0.0	1.688
$0.1\sqrt{3}$	3.696
$0.2\sqrt{3}$	4.900
$0.3\sqrt{3}$	5.139
$0.4\sqrt{3}$	6.519

[1] Maximum position error per dimension $\times\sqrt{3}$.
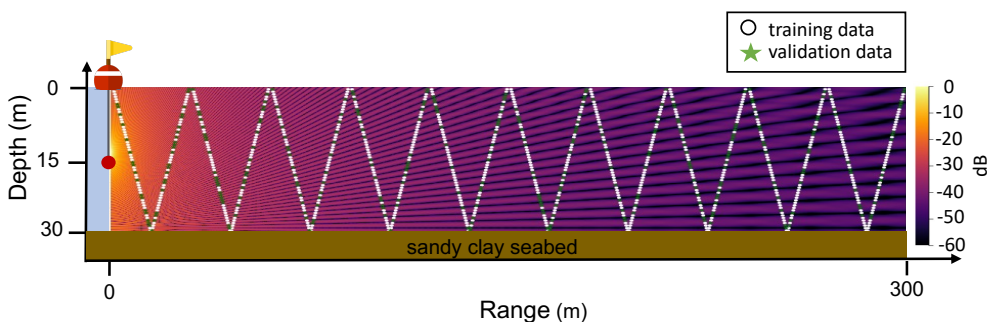
Figure 4.10: Simulated environment for inversion of seabed reflection model. The trajectory of the profiling float can be seen in terms of the training data points. The ground truth field pattern within the AOI is also shown.

arrivals overlap and cannot be separated, we cannot measure the reflection coefficient directly. Our proposed recipe can, however, learn a reflection model from observed total transmission loss at a number of observation points. We use the RBNN model from Section 4.2.2.2 together with the RCNN layer, where the RCNN models the unknown reflection coefficient (as a function of reflection incident angle). By training the composite spherical wave model described in (4.19), we can recover a trained RCNN as a model for the seabed reflection.

We assume that the channel geometry and source location are known. A 5 kHz source is deployed at a depth of 15 m and a profiling float is employed

TABLE 4.6: Effect of measurement position error on the learnt seabed reflection model.

Maximum position error (m)	Reflection coefficient	Reflection phase shift
0.00		
$0.01\sqrt{3}$		
$0.05\sqrt{3}$		
$0.10\sqrt{3}$		
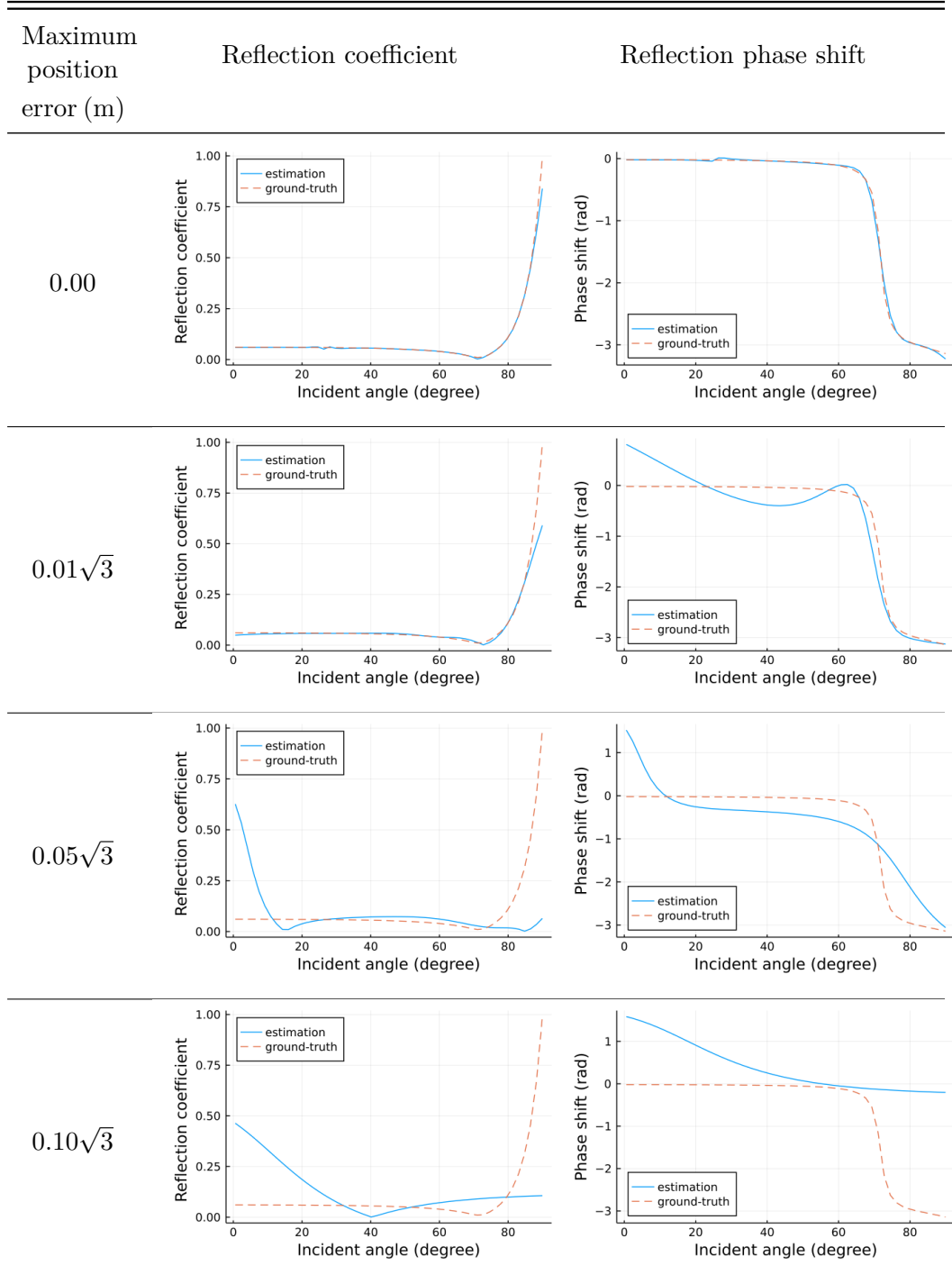
to perform 10 profiles through a 300 m × 30 m AOI. The simulation setup is illustrated in Fig. 4.10. A total of 1,150 acoustic field measurements are collected along the trajectory, and 70% of them are used to train the composite RBNN model. The environmental setup is similar to the near-field acoustic field prediction application in Section 4.3.2, and the synthetic data are generated using Bellhop. We pre-calculate the nominal arrival directions and propagation distances and use acoustic data to optimize the trainable model parameters $\mathcal{T}_{\mathrm{sg}}$ given in (4.22).

In Table 4.6, we present the inferred reflection coefficient curves and phase shift curves for various amounts of position measurement error. In an ideal scenario with no measurement errors, we can accurately recover the seabed reflection model. The modeling errors increase with the amount of position measurement errors, as one would expect. The effect of measurement errors can be partially mitigated by increasing the size of the training dataset.

4.3.4 Geo-acoustic inversion for seabed properties

The last application we shall consider is a geo-acoustic inversion problem, where we wish to determine geo-acoustic seabed properties from acoustical field measurements. We consider a simple Rayleigh reflection model to illustrate the idea. The complex Rayleigh reflection coefficient is given by [68]:

$$\Gamma = \frac{\rho_{\mathrm{r}} \cos \gamma - \sqrt{(\frac{\bar{\bar{\delta}}}{c_{\mathrm{r}}})^2 - \sin \gamma^2}}{\rho_{\mathrm{r}} \cos \gamma + \sqrt{(\frac{\bar{\bar{\delta}}}{c_{\mathrm{r}}})^2 - \sin \gamma^2}}, \tag{4.25}$$
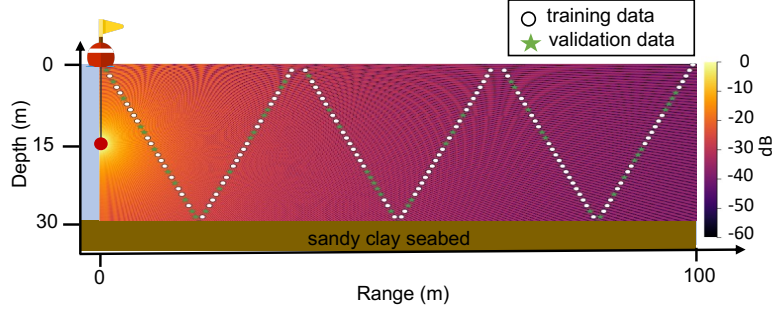
Figure 4.11: Simulated environment for the geo-acoustic inversion of seabed properties. The trajectory of the profiling float can be seen in terms of the training data points. The ground truth field pattern within the AOI is also shown.

where

$$\bar{\delta} = 1 + i\delta, \tag{4.26a}$$

$$\rho_{\mathrm{r}} = \frac{\rho_{\mathrm{seabed}}}{\rho_{\mathrm{seawater}}}, \tag{4.26b}$$

$$c_{\mathrm{r}} = \frac{c_{\mathrm{seabed}}}{c_{\mathrm{seawater}}}, \tag{4.26c}$$

where δ denotes dimensionless seabed absorption coefficient, ρ_{r} denotes relative density, c_{r} represents relative sound speed. We assume ρ_{r}, c_{r} and δ are unknown and to be determined from acoustic field measurements.

We assume that the source and receiver locations, as well as the channel geometry, are known. An acoustic float is employed to take 166 acoustic measurements over 100 m $\times$ 30 m AOI along a zig-zag trajectory from a 5 kHz acoustic source deployed at a depth of 15 m. Same as previous applications, 70% of the measurements are used to train the RBNN model, while the balance 30% is used for validation. Fig. 4.11 depicts the simulated environment and the sampling trajectory of the acoustic float.

TABLE 4.7: Estimated seabed parameters as a function of maximum position measurement error.

Maximum position error (m)	Training dataset	ρ_r [% error]	c_r [% error]	$\log(\delta)$ (dB) [% error]
0.00	166	1.147 [0.0%]	0.985 [0.0%]	-2.616 [0.0%]
$0.01\sqrt{3}$	166	1.221 [1.2%]	0.998 [-0.7%]	-2.910 [-11.2%]
$0.05\sqrt{3}$	252	1.055 [-8.0%]	0.988 [0.3%]	-2.222 [15.1%]
$0.10\sqrt{3}$	335	1.153 [0.5%]	0.994 [0.9%]	-3.810 [-45.6%]
$0.20\sqrt{3}$	335	1.204 [5.0%]	0.948 [-3.7%]	-3.342 [-27.8%]
$0.50\sqrt{3}$	421	1.257 [8.1%]	0.992 [0.8%]	-4.211 [-61.0%]

In Section 4.3.3, we model the angle-dependent complex reflection coefficient using a RCNN. While this is useful for acoustic propagation modeling, this approach does not yield estimates of geo-acoustic properties such as ρ_r, c_r and δ. We therefore replace the RCNN layer in (4.19) with the expression for complex reflection coefficient from (4.25), and train the resultant composite RBNN. The set of trainable parameters for this RBNN is:

$$\mathcal{T}_{\text{sg}} \equiv (k, \boldsymbol{e}_\theta, \boldsymbol{e}_\psi, \boldsymbol{e}_d, \rho_r, c_r, \delta). \tag{4.27}$$

Table 4.7 summarizes the estimated values and percentage error for the three unknown geo-acoustic parameters for various levels of position measurement errors. With accurate measurements, the model is effective in accurately

determining the geo-acoustic parameters. In the presence of position errors, we need to increase the training data size to improve model robustness. The robustness of geo-acoustic inversion depends on the sensitivity of the acoustic field to each geo-acoustic parameter. In this example, ρ_r and c_r affect the acoustic field more strongly than δ. Increasing training dataset size improves the robustness of the estimates of ρ_r and c_r, but much less for δ.

4.4 Discussion

The numerical studies evaluated in this chapter assume single-frequency CW acoustic signals. To exploit received signals in the frequency domain, we can apply the RBNN framework to model multi-frequency acoustic propagation. The frequency-aided RBNN framework utilizes multi-frequency acoustic field measurements at various locations to learn common model unknowns over a frequency band. This idea potentially gives us advantages in data efficiency. We have primarily explored this idea in [163].

As our proposed modeling recipe is structurally constrained to only predict physically realistic results, it may have problems escaping from local minima and jumping from one location in the solution space to another where paths in between pass through regions with no physical solution during the training. We purposely initialize a lot more rays to tackle such an issue. PINNs handle local minima by controlling the hyper-parameters of physical PDE constraints in the loss functions. We can make physics-informed loss terms weaker in order to allow PINNs jump over such regions, after which we can put more weights on the PDE constraints to make PINN predictions obey physics. This

allows us to put different emphases on obeying physics and being data-driven at different training stages to aid the learning of PINNs. However, optimally tuning all hyper-parameters in PINNs is hard. The PDE constraints in PINNs are mathematically weaker than the structural constraint used in our proposed modeling recipe. The PINNs are fundamentally NN models which potentially introduce a lot more trainable parameters than our physics-based model. These explain why our proposed physics-based data-aided modeling recipe performs well in the propagation modeling problems evaluated in this thesis.

4.5 Summary

In this chapter, we proposed a data-efficient acoustic propagation modeling framework based on the ray theory for high-frequency underwater applications. It can incorporate any known environmental information and be trained with observed data, making it suitable for solving both forward and inverse propagation modeling problems using limited data. We demonstrated a few applications of the proposed RBNN framework to highlight its flexibility and capability in various acoustic propagation modeling scenarios. Our approach is not only data-efficient, but also avoids the need for additional hyper-parameter tuning†. Moreover, the algorithm is computationally simple and we can fully model 3D acoustic environments easily.

The proposed RBNN framework can model acoustic propagation in any underwater environment under partial environmental knowledge. It bridges the gap in the state-of-the-art modeling techniques, and thus can solve some

---

†The hyper-parameters in our proposed recipe are much more robust than hyper-parameters in PINNs

practical modeling problems that used to be considered challenging or infeasible. In the next chapter, we will apply the proposed RBNN modeling framework to effectively model acoustic propagation in a partially unknown confined water environment where neither modeling it analytically nor geometrically using the state-of-the-art modeling techniques works.

Chapter 5

Propagation Modeling in Confined Waters

Small confined water environments, such as water tanks and pools, are strongly reverberant and surprisingly complicated to model. Conventional acoustic propagation models are typically designed for open water environments where out-of-plane arrival energy is negligible. Modeling acoustic propagation in confined water environments is extremely hard using state-of-the-art modeling techniques, especially for irregular and less known environments. Fortunately, the acoustic propagation modeling recipe proposed in Chapter 4 generalizes well in any underwater environment, providing us a new modeling alternative for problems that cannot be addressed by conventional models. In this chapter, we utilize the proposed RBNN modeling framework to model acoustic propagation in an acoustically complicated confined water environment, specifically a small water tank, under partial environmental knowledge. The work presented in this chapter is published in [155].

5.1 Problem formulation

We aim to model acoustic propagation in a 3D cubic water tank using a small number of acoustic measurements collected within an AOI by means of the proposed RBNN modeling framework. While acoustic rays in the rectangular geometry can be modeled with a 3D ray tracer, multiple reflections lead to strong
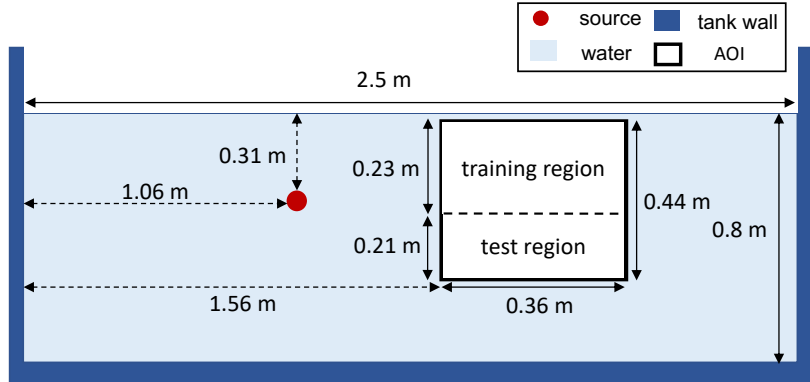
(a) Side view
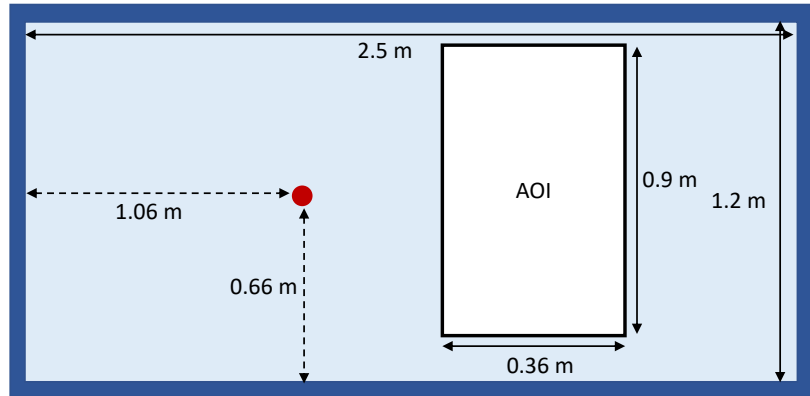
(b) Top view

Figure 5.1: Water tank setup.

sensitivity to minor geometrical irregularities of the tank wall. The tank walls are made of an inhomogeneous composite material (fibre-reinforcement plastic) with complicated reflection properties that are not directly measurable. This provides us a challenging acoustic propagation modeling problem.

The water tank has a dimension of 2.5 m × 1.2 m × 0.8 m with a 10 kHz CW acoustic signal source deployed, as illustrated in Fig. 5.1. A 0.36 m × 0.9 m × 0.44 m AOI is located 0.5 m from the source. The sound speed is assumed to be 1,505 m/s, in accordance with conductivity and temperature measurements in our tank. We split the AOI into non-overlapping training and

test regions to test the extrapolation capability of the models. The training and validation data (250 and 28 data points respectively) are obtained from the training region, whereas the test data (222 data points) are obtained in test region.

Before undertaking modeling using experimental data, we develop a simplified simulation model of the tank to establish the feasibility of applying our method to the tank environment. The simulation results are presented in Section 5.3. Once we have established the feasibility and developed an understanding of what performance we might expect, we experimentally model the acoustic propagation in the tank in Section 5.4.

5.2 State-of-the-art modeling approaches

To the bests of our knowledge, there are only few attempts addressing acoustic propagation modeling in confined waters in literature. For regular confined water environments, such as cubic swimming pools and water tanks, using ISM to geometrically model the acoustic propagation is straightforward assuming channel geometry and boundary conditions are accurately provided. In [164], the authors characterize an ultrasonic communication channel in a swimming pool and show that the swimming pool is a rich multipath environment. However, this work focuses on characterizing acoustic communication instead of modeling acoustic propagation. It assumes that the swimming pool can be modeled as water surrounded by air. Such an assumption greatly simplifies the acoustic modeling problem as the reflection loss is negligible for flat water-air interfaces. The swimming pool can then be readily modeled using ISM. In [165], the authors

model a swimming pool geometrically using ISM by assuming constant reflection losses regardless of the incident angles.

Accurately locating all contributing image sources is one of the key steps to geometrically modeling acoustic propagation in confined waters using ISM. This is challenging for irregular environments, such as water tanks and pools with slops and curved walls. On the other hand, the knowledge of reflective characteristics of surrounding boundaries is also critical. The reflection coefficient and phase shift are incident angle dependent and hard to be rigorously measured in most practical scenarios. This is true for both confined water environments and open water environments. Although the Rayleigh reflection coefficient is commonly used in the context of underwater acoustics to estimate the complex reflection coefficient of boundaries given geo-acoustic parameters (e.g., sound speed, density) of two mediums [166], accurately measuring the required parameters is still practically difficult.

The water tank modeled in this chapter is cubic with a known dimension. The reflective characteristics of all sidewalls are unknown and difficult to measure. The current propagation modeling methods cannot tackle such a confined water environment with partial environmental and physical knowledge.

5.3 Simulation study

We carry out a simulation study to establish the feasibility of the measurement locations, the exact amount of acoustic data used and the designed experiment setup. This simulation study shows us what is theoretically possible before practically implementing the experiment and collecting lots of acoustic

observations.

We use the spherical wave formulation with the knowledge of geometry based on (4.19) to predict the field in the AOI. We minimize the loss function defined in (4.23) to find optimal trainable parameters $\mathcal{T}$ defined as (4.22). We adopt a geometrical ray model to simulate the acoustic propagation in the tank environment, and generate synthetic acoustic measurements[*] within the AOI. We assume the water-air interface to be a perfect reflector with a reflection coefficient of -1. We adopt a simple tank sidewalls and bottom reflection model, and assume the reflection coefficient to be given by (4.25), with $\rho_\mathrm{r} = 1.5$, $c_\mathrm{r} = 0.9$ and $\delta = 0.0$. For benchmarking, we use GPR and DNN similar to those described in Section 4.3.1.

We generate a dense test dataset of $30,303$ points over the entire AOI with a resolution of 0.01 m in range and width, and 0.05 m in depth. It is not practical to collect such a dense dataset during the later experiment. So we also generate a sparse test dataset of 222 points in the test region for later benchmarking of the experimental results.

Since the measurement accuracy of tank dimensions and hydrophone locations in the tank is limited, we introduce measurement errors in the tank size, source location and measurement locations in the simulation too. The simulated tank dimensions are mismatched from the geometrical knowledge available to our algorithm by 0.010 m, 0.015 m and 0.020 m in the three dimensions. The source location deviates by 0.02 m from the location provided to the algorithm.

---

[*]The acoustic measurements are shown in Volts, as we measure the pre-amplified output from the hydrophones in Volts during the experiment. These can be converted to μPa by multiplying by the gain-corrected acoustic sensitivity of the hydrophone.

Due to practical considerations, the measurement errors in shallower hydrophone locations in our tank are expected to be less than that for deeper locations. We therefore introduce a random error of up to 0.02 m per dimension for acoustic measurements with depths shallower than 0.36 m, and 0.04 m per dimension for deeper locations. We calculate the nominal incoming ray directions and propagation distances prior to the training. We allow our RBNN model to train the error to the nominal directions and propagation distances to cope with the erroneous source location and tank size measurements, as discussed in Section 4.2.2.2. To allow for a few measurement outliers during the experiment, we opt to minimize the mean absolute error in the training process, rather than the RMS error. This encourages the model to focus on fitting the majority of the training data well, and ignore a few outliers.

The rich multipath in the simulated water tank environment yields a complicated field pattern. Cross-sections of the ground truth field and the estimated field at four different depths within the AOI are shown in Fig. 5.2. Do note that the estimated field at the depth of 0.45 m is extrapolated as none of the training data or validation data falls in this test region. We see that the RBNN model can recover and extrapolate the field reasonably well, whereas the GPR and RBNN methods fail to do so. The mean absolute test error (MATE) of the sparse and dense test datasets is shown in Table 5.1.

The sparse test error and dense test error are based on error-free measurements. The two types of test errors are in a similar range for all of the three models. This suggests that the sparse test error is a representable measure of field prediction performance. We also extrapolate the field to the entire water

(a) Ground truth field within the AOI

(b) RBNN field estimates within AOI

(c) GPR field estimates within AOI

(d) DNN field estimates within AOI
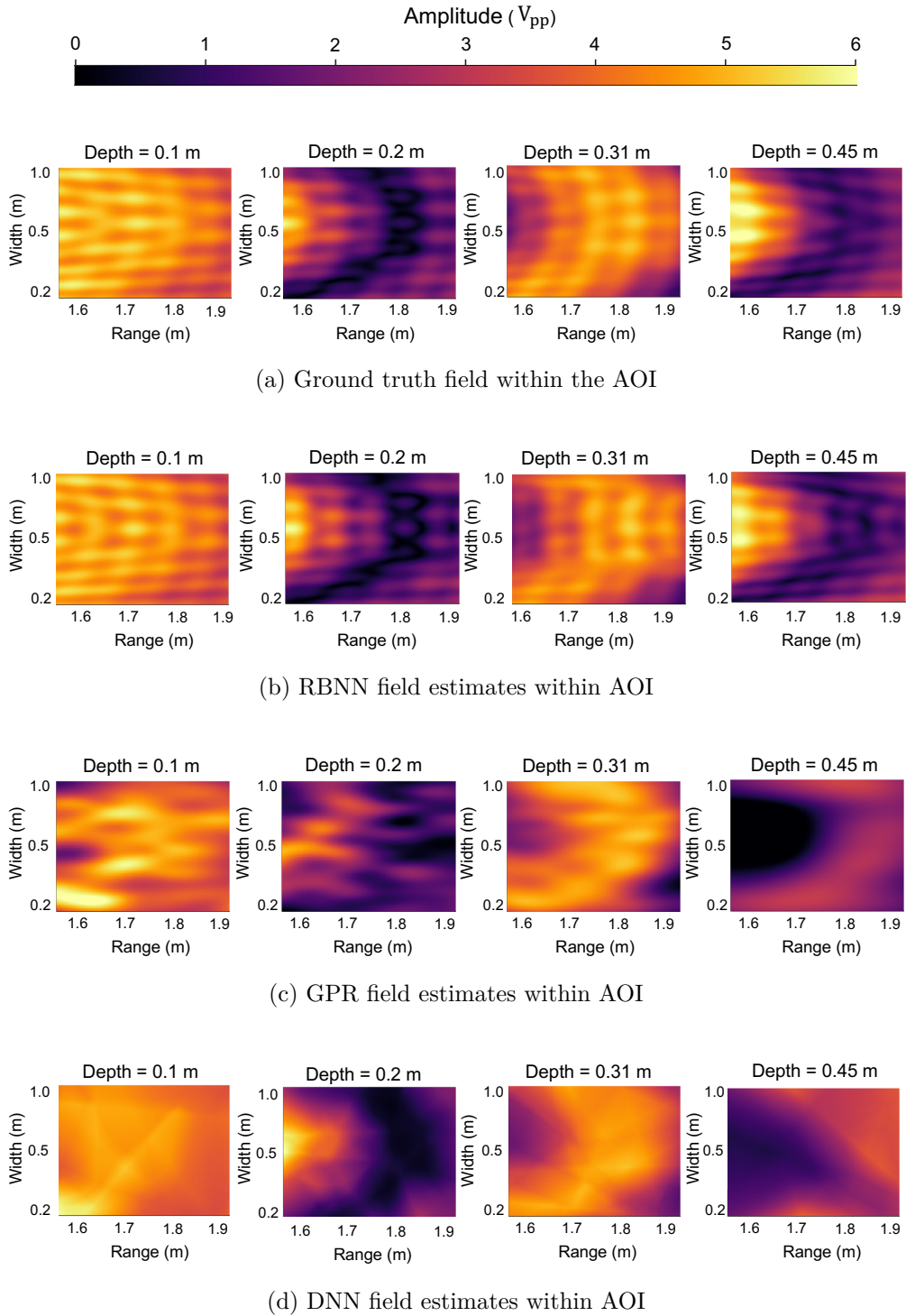
Figure 5.2: Ground truth and estimated acoustic fields at four different depths. The depth of 0.45 m is in the test region, where no training data is made available to the three models. The other three depths are in the training region.

(a) Ground truth field in an extended region

(b) RBNN extrapolated field estimates

(c) GPR extrapolated field estimates

(d) DNN extrapolated field estimates
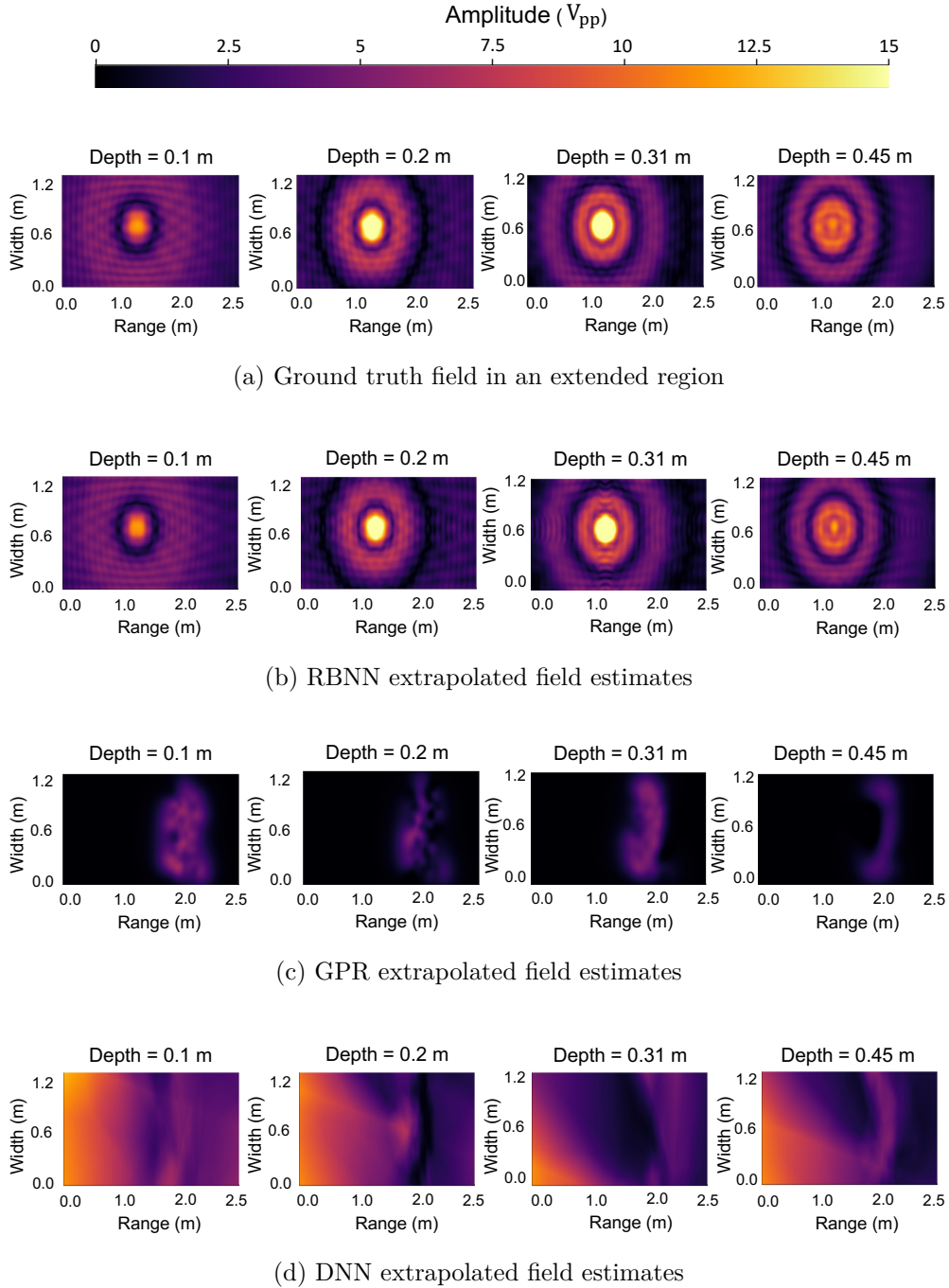
Figure 5.3: Ground truth and extrapolated fields within the entire tank at four different depths.

TABLE 5.1:   MATE of the estimated acoustic field in the simulation study.

Method	MATE (V_{pp})	
	Sparse	Dense
RBNN	0.014	0.242
GPR	2.676	1.860
DNN	1.444	1.132

tank environment as shown in Fig. 5.3. Not surprisingly, the classical data-driven techniques fail to extrapolate the field in the region away from the AOI, whereas the RBNN model can generalize well and predict the field in the entire water tank.

5.4 Experimental modeling of a water tank

With the feasibility established via simulation, we can model the acoustic propagation in the water tank using the same setup described in Section 5.3. The equipment setup used in the experiment is shown in Fig. 5.4. We used a National
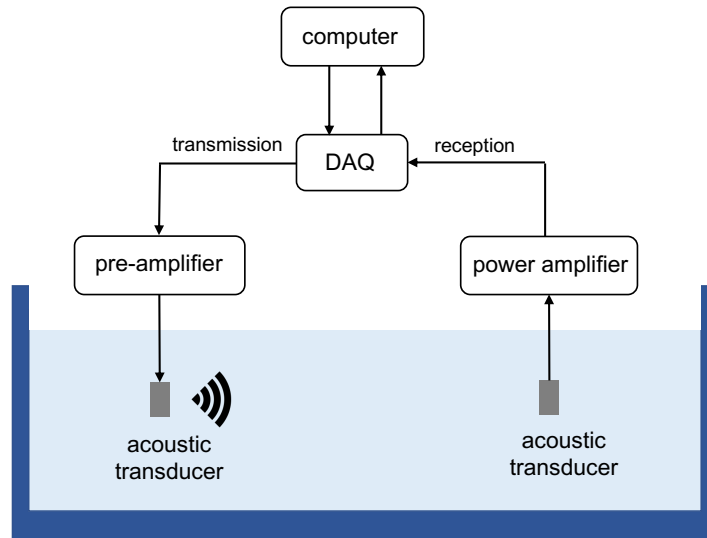
Figure 5.4: Equipment setup for the experiment.

Figure 5.5: The water tank with the fixtures.

Instruments Data Acquisition (NI-DAQ) system to transmit a CW signal at 10 kHz with an amplitude of 1 V_{pp}. A pair of TC4013 acoustic hydrophones [167] were used as the transmitter and receiver. 500 acoustic measurements were collected at the same locations as the data generated in the simulation study. Each hydrophone was attached to a fishing line, with a reel and sliding block mechanism to control the 3D position of the hydrophone as shown in Fig. 5.5.

The water tank was located outdoors and experienced a light breeze on occasion. This led to slight measurement errors due to small-scale oscillations of the source and receiver. The oscillations manifest themselves as fluctuations in the amplitude and phase of the recorded signal. We computed the average envelope over a 40 second period to reduce the impact of oscillations on the measurements. The RBNN model allows for errors in direction of arrival to be

estimated during the training.

In addition to angular errors, we also expect some errors (few centimeters) in measurements of location of the hydrophones. We design a two-stage training strategy to deal with such location measurement errors. The first stage aims to optimize the trainable parameters $\mathcal{T}$, specified in the designed RBNN model, using measured location data. We freeze the trained RBNN model at the end of this stage, and focus on estimating measurement errors in the second stage. We feed the corrected locations[†] into the RBNN model to predict acoustic fields in this stage. A L_2-norm penalty term of absolute position errors is added in the loss function to constrain the range of position errors. By minimizing the loss function, the second stage aims to estimate the most appropriate location errors using the RBNN model parameterized by the parameters trained in the first training stage.

To benchmark the RBNN performance, we use a GPR and DNN[‡] as in the simulation study. For each of the three methods, Figs. 5.6 and 5.7 show the estimated fields within the AOI and the extrapolated fields in the entire tank respectively. The field pattern extrapolated by the RBNN model looks reasonable in the sense that the region with the strongest pressure amplitude is consistent with the source location. The GPR and DNN fail to reconstruct any discernable field pattern in the tank. In line with this, the MATE of the RBNN model is significantly lower than that of the GPR and DNN models, as shown

---

[†]The corrected locations are the measured locations offset by the estimated location errors in all dimensions

[‡]We found that the DNN performed better with experimental data if we replaced the ReLU activation function with a hyperbolic tangent (tanh) activation function, and therefore we present results for the tanh-activated DNN in this section.

(a) RBNN field estimates within AOI

(b) GPR field estimates within AOI

(c) DNN field estimates within AOI
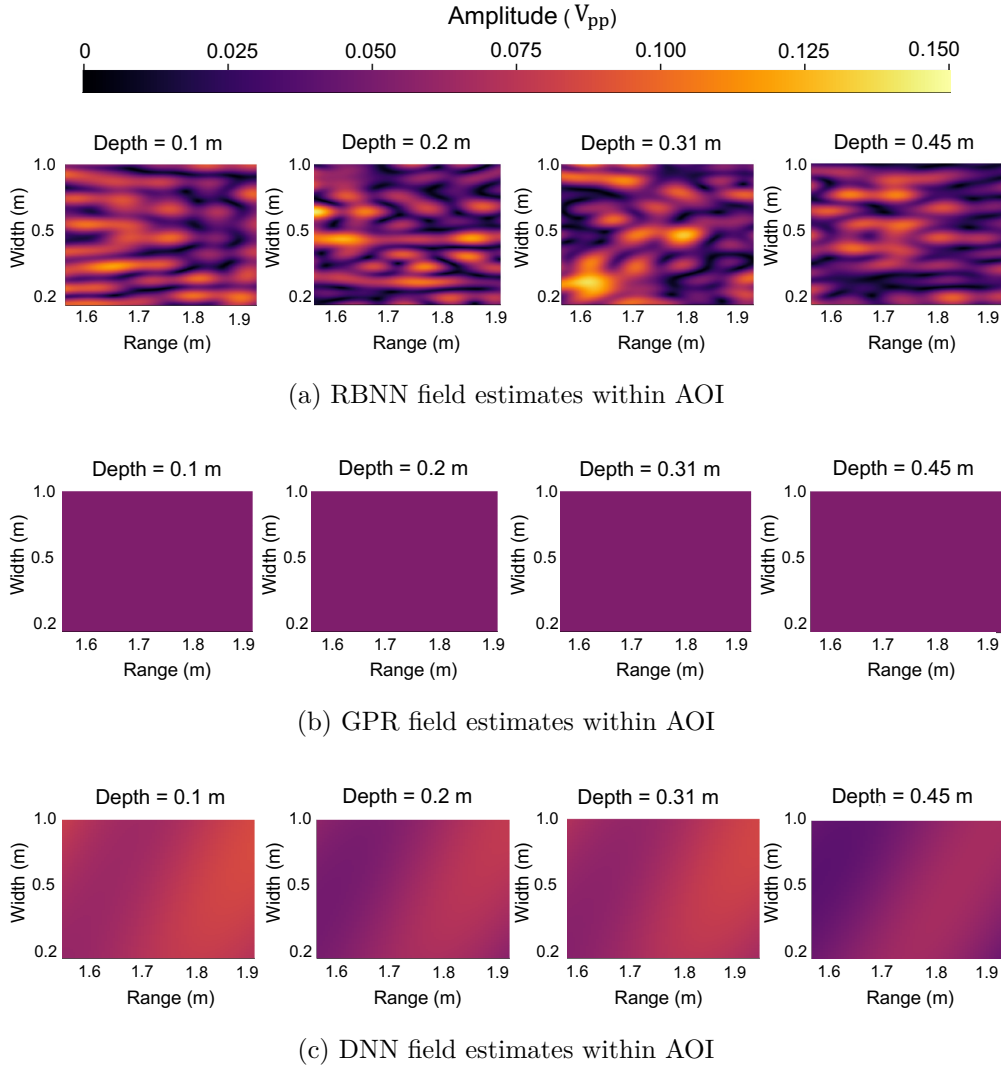
Figure 5.6: Estimated field patterns within AOI using the experimental data by the three models.

in Table 5.2. The absolute trained position errors for the 222 sparse test data points are shown in Fig. 5.8. Most errors are below 4 cm, as we would expect from our measurement procedure.

Fig. 5.9 shows the learnt reflection coefficient and phase shift for the water tank walls. While we do not have ground truth to validate the reflection coefficient curves, the learnt model works well to estimate the acoustic field

Amplitude (V_{pp})

(a) RBNN extrapolated field estimates

(b) GPR extrapolated field estimates

(c) DNN extrapolated field estimates
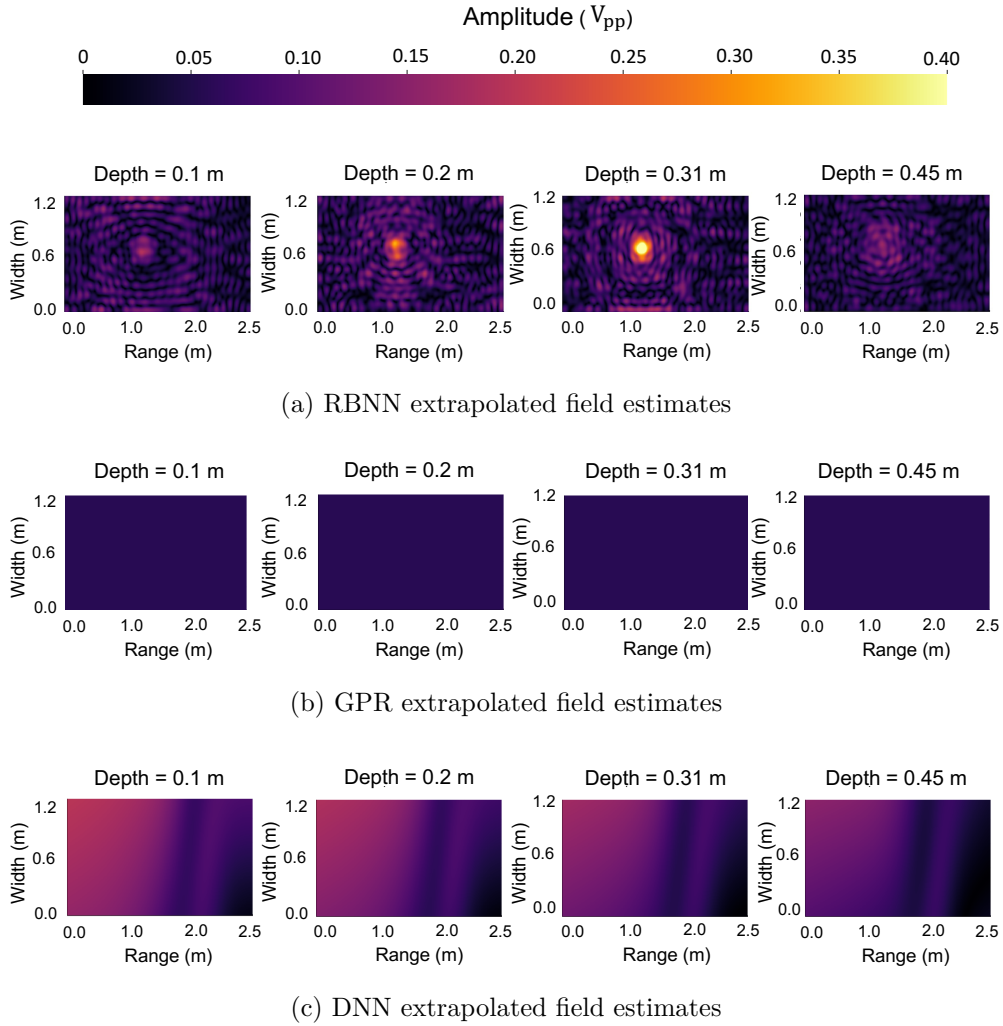
Figure 5.7: Extrapolated field patterns of the entire tank environment using the experimental data by the three models.

TABLE 5.2:   Performance evaluation of the estimated acoustic field from the controlled experiment.

Method	MATE (V_{pp})	MATE (dB)	Spearman's correlation coefficient
RBNN	0.003	0.381	0.971
GPR	0.021	3.675	-0.064
DNN	0.024	4.147	-0.139
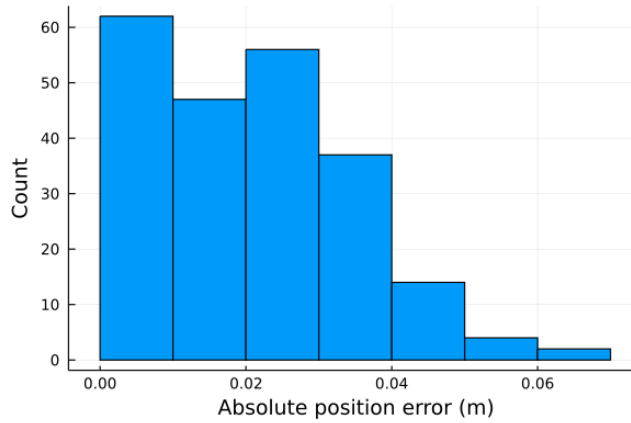
Figure 5.8: Trained absolute position error of the sparse test data using the RBNN model.

(a) Reflection coefficient   (b) Reflection phase shift
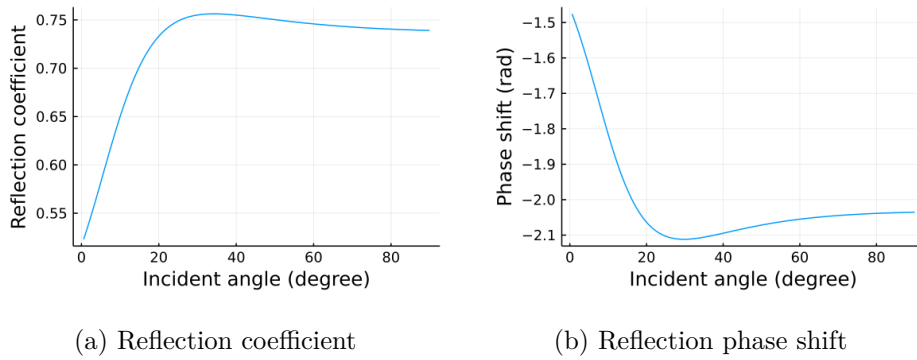
Figure 5.9: Estimated reflection model based on the trained RCNN layer of the composite RBNN.

in the tank. We observe this in the good agreement between RBNN predictions and measured data in Fig. 5.10, and also as a Spearman's correlation coefficient of 0.971 between the predictions and observations in Table 5.2. On the other hand, the GPR and DNN simply learn to predict average values regardless of the measurement location. The results obtained from the experiment thus validate the efficacy of our proposed RBNN framework to model acoustically complicated confined water environments under partial environmental knowledge.

101
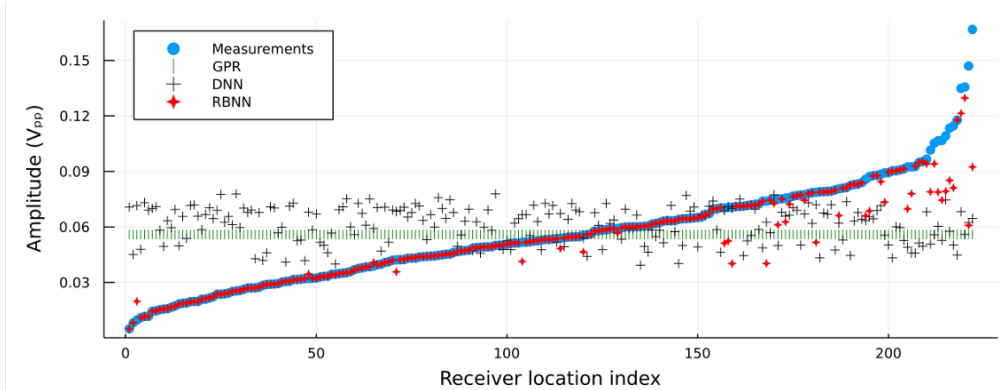
Figure 5.10: Comparison between test data and model predictions.

5.5 Summary

In this chapter, we applied the high-frequency modeling framework proposed in Chapter 4 to model acoustic propagation in a highly reverberant water tank. Such an acoustically complicated confined water environment with unknown sidewall characteristics cannot be modeled using conventional methods. We implemented a simulation study to primarily validate the feasibility of the proposed modeling framework in handling such a challenging modeling problem. With the satisfying results obtained, we trained our RBNN modeling framework using a limited number of acoustic measurements collected in a small section of the tank. The proposed ray-based modeling framework significantly outperforms the two classical ML models in terms of interpolation and extrapolation performance of acoustic fields.

The discussion and evaluations presented in Chapter 4 and Chapter 5 used the proposed high-frequency modeling framework derived from the ray theory. However, this formulation is not accurate at low frequencies when the

high-frequency approximation used in the ray theory breaks down. In the next chapter, we will tailor the proposed hybrid modeling recipe for low-frequency oceanic applications based on the normal mode theory.

Chapter 6

Mode-based Data-aided Propagation Modeling

In Chapter 4, we proposed the RBNN framework based on the ray theory for high-frequency acoustic propagation modeling. We practically utilized the RBNN framework to model acoustic propagation in a highly reverberant water tank in Chapter 5. While the ray theory is widely used for high-frequency underwater applications, its accuracy is inherently limited at low frequencies because of the high-frequency approximation applied. The normal mode theory is an accurate and computationally efficient alternative to model acoustic propagation at low frequencies. The proposed modeling recipe can be applied to any physics-based model. In this chapter, we tailor the proposed recipe based on the normal mode theory to model low-frequency acoustic propagation. The work presented in this chapter is published in [168].

6.1 Problem formulation

In a 2D ocean waveguide, a low-frequency acoustic source transmits CW signals at frequency f omnidirectionally. In accordance with the normal mode theory, the pressure amplitude $\bar{p}(r, z)$ received at a location with range r and depth d is composed of a set of modes. We aim to effectively find all contributing mode solutions to model acoustic propagation of a low-frequency source using limited environmental knowledge and a small amount of acoustic data collected within

an area of measurement (AOM).

6.2 Normal mode theory

Similar to the ray theory, the normal mode theory is also derived from the acoustic wave equation. Classical normal mode models apply the separation of variables [169] to express acoustic field at location (r, z) as a combination of a depth-dependent term and a range-dependent term:

$$\bar{p}(r, z) = \Psi(z)\Phi(r). \tag{6.1}$$

We substitute (6.1) into the Helmholtz equation derived in (4.3). After rearranging and simplification, we obtain the modal equation [31]:

$$\rho(z)\frac{\mathrm{d}}{\mathrm{d}z}\left(\frac{1}{\rho(z)}\frac{\mathrm{d}\Psi(z)}{\mathrm{d}z}\right) + k_{\mathrm{z}}^2(z)\Psi(z) = 0, \tag{6.2}$$

where

$$k_{\mathrm{z}}^2(z) = k^2(z) - k_{\mathrm{r}}^2, \tag{6.3}$$

where $\rho(z)$ is density at depth z, $k(z) = \frac{\omega}{c(z)}$, k_{z} denotes vertical wavenumber and k_{r} represents horizontal wavenumber.

The modal equation derived in (6.2) is in the form of a classical Sturm-Liouville eigenvalue problem [170]. Theoretically, there are an infinite number of distinct mode solutions ($\Psi(z)$ and k_{r}) to the modal equation (6.2). Normalized mode solutions form a complete set so that solutions to the wave

equation can be represented as an infinite sum of the normal modes:

$$\bar{p}(r, z) = \sum_{m=1}^{\infty} \Psi_m(z)\Phi_m(r),$$
(6.4)

where m denotes m^{th} mode.

The range-dependent term $\Phi_m(r)$ has a standard form in terms of the Hankel function [31]:

$$\Phi_m(r) = \frac{i}{4\rho(z_s)} \Psi_m(z_s) H_0^{(1,2)}(k_{\mathrm{r}m}r),$$
(6.5)

where z_{s} denotes source depth and $H_0^{(1,2)}$ refers to the Hankel function of first or second kind. The choice of the Hankel function depends on radiation conditions. We adopt the Hankel function of the first kind since we assume energy is radiating outwards as r approaches ∞. The asymptotic approximation to the Hankel function of the first kind is often used in literature and (6.5) is approximated by:

$$\Phi_m(r) \approx \frac{i}{\rho(z_{\mathrm{s}})\sqrt{8\pi r}} e^{-i\frac{\pi}{4}} \Psi_m(z_{\mathrm{s}}) \frac{e^{ik_{\mathrm{r}m}r}}{\sqrt{k_{\mathrm{r}m}}}.$$
(6.6)

Popular normal mode models, such as Kraken [82], seek all contributing eigenfunction solutions $\Psi_m(z)$ and corresponding eigenvalues $k_{\mathrm{r}m}$ to the modal equation (6.2) while satisfying boundary conditions and environment setup.

6.3 Mode basis neural network framework

An imaginary $k_{\mathrm{r}m}$ makes $e^{ik_{\mathrm{r}m}r}$ in (6.6) an exponentially decay term with respect to range r. A real $k_{\mathrm{r}m}$ leads to a propagating mode that oscillates instead. In far-field where propagating modes are dominating, the infinite sum in (6.4) can be approximated as a n_{mode}-element finite sum and the absolute pressure

amplitude received at location (r, z) is:

$$\hat{p}(r, z) \approx \left| \frac{i}{\rho(z_\mathrm{s})\sqrt{8\pi r}} e^{-i\frac{\pi}{4}} \sum_{m=1}^{n_\mathrm{mode}} \Psi_m(z)\Psi_m(z_\mathrm{s}) \frac{e^{ik_{\mathrm{r}m}r}}{\sqrt{k_{\mathrm{r}m}}} \right|. \tag{6.7}$$

Although analytical solutions to (6.2) are not always available, general field solutions based on the normal mode theory approximately follow [31]:

$$\hat{p}(r, z) \approx \left| \sum_{m=1}^{n_\mathrm{mode}} \left(\bar{A}_m e^{ik_{\mathrm{z}m}z} + \bar{B}_m e^{-ik_{\mathrm{z}m}z} \right) \Phi_m(r) \right|, \tag{6.8}$$

where $\bar{A}_m$ and $\bar{B}_m$ are scaling factors to make sure boundary conditions and environment setup are satisfied.

Even though the approximated field expression is provided in (6.8), the parameters $\bar{A}_m$, $\bar{B}_m$, $k_{\mathrm{r}m}$ and $k_{\mathrm{z}m}$ associated with each mode are calculable only if boundary conditions and all required environmental parameters are accurately known. Any missing environmental parameter makes conventional normal mode models fail to operate. Such a requirement greatly limits practical uses of normal mode models as operating environments are not always well understood.

We propose a specialized NN model–*mode basis neural network* (MBNN) framework to tackle such situations motivated by the ideas of SciML. Similar to the RBNN framework, we encode the domain knowledge of acoustic propagation based on the normal mode theory into the structure of a NN to model low-frequency acoustic propagation. The MBNN framework retains the capabilities of the RBNN model demonstrated in Chapter 4. The proposed MBNN framework makes physical-based normal mode models data-driven to

tackle various scenarios. In Section 6.3.1 and Section 6.3.2, we illustrate three MBNN formulations in 2D ocean waveguides with isovelocity SSP and non-isovelocity SSP respectively.

6.3.1 Isovelocity ocean waveguides

We consider an isovelocity ocean waveguide that has a constant sound speed c and density ρ across a water depth D. A general eigenfunction solution to (6.2) in this isovelocity ocean waveguide follows [31]:

$$\Psi_m(z) = \bar{A}_m \sin(k_{\mathrm{z}m}z) + \bar{B}_m \cos(k_{\mathrm{z}m}z). \tag{6.9}$$

We assume a pressure-release surface:

$$\Psi_m(0) = 0, \tag{6.10}$$

and a rigid bottom:

$$\left. \frac{\mathrm{d}\Psi}{\mathrm{d}z} \right|_{z=D} = 0. \tag{6.11}$$

Such boundary conditions further simplify (6.9) to:

$$\Psi_m(z) = \sqrt{\frac{2\rho}{D}} \sin(k_{\mathrm{z}m}z). \tag{6.12}$$

The corresponding eigenvalue $k_{\mathrm{r}m}$ is derived as:

$$k_{\mathrm{r}m} = \sqrt{\left(\frac{\omega}{c}\right)^2 - \left((m+0.5)\frac{\pi}{D}\right)^2}, \quad m = 1, 2, \cdots, n_{\mathrm{mode}}. \tag{6.13}$$

We assume that we do not know the exact values of c, ρ and D. Due to missing environmental knowledge, conventional normal mode models can not predict acoustic fields. Fortunately, our proposed MBNN model can automatically learn the best-fitted values of the unknown mode parameters from acoustic data. We train a minimal set of unknown mode parameters and numerically calculate other unknowns using underlying physics to make our model generalize well.

We denote the minimal set of unknown mode parameters whose values are yet to learn from acoustic observations as MBNN model trainable parameters:

$$\mathcal{T}_i \equiv (c, \rho, D).$$
(6.14)

We minimize the square difference between the estimated absolute pressure amplitude $\hat{p}(r, z; \mathcal{T}_i)$ and the acoustic field measurement y at a measurement location (r, z) by tuning $\mathcal{T}_i$. The loss function is defined as:

$$L_i(r, z, y; \mathcal{T}_i) = |\hat{p}(r, z; \mathcal{T}_i) - y|^2.$$
(6.15)

Equation (6.15) often sums over a mini-batch of training data in each iteration as per the standard practice in ML. With the optimal trainable parameters $\mathcal{T}_i^*$ learnt from training data, we can readily predict acoustic fields using (6.3), (6.7), (6.12) and (6.13).

6.3.2 Non-isovelocity ocean waveguides

6.3.2.1 With knowledge of SSP

The MBNN framework is capable of modeling non-isovelocity ocean waveguides as well. As the modal equation can not be analytically solved for ocean waveguides with non-isovelocity SSPs, approximated solutions are necessary. We use the Wentzel–Kramers–Brillouin (WKB) approximation [171], one of the most widely used approximation techniques in normal mode literature, to approximate the depth-dependent term:

$$\Psi_m(z) \approx \bar{A}_m \frac{e^{i \int_0^z k_{zm}(s)ds}}{\sqrt{k_{zm}(z)}} + \bar{B}_m \frac{e^{-i \int_0^z k_{zm}(s)ds}}{\sqrt{k_{zm}(z)}}, \qquad (6.16)$$

where

$$k_{zm}(z) = \sqrt{\left(\frac{\omega}{c(z)}\right)^2 - k_{rm}^2}. \qquad (6.17)$$

We assume boundary conditions are unknown. This missing information introduces more unknown mode parameters as compared to the isovelocity waveguide case in Section 6.3.1. When SSP is provided, we can use acoustic observations to find optimal trainable parameters:

$$\mathcal{T}_{\mathrm{nk}} \equiv \left(\bar{\boldsymbol{A}}, \bar{\boldsymbol{B}}, \boldsymbol{k}_{\mathrm{r}}\right), \qquad (6.18)$$

where $\bar{\boldsymbol{A}} = \left[\bar{A}_1, \bar{A}_2, \ldots, \bar{A}_{n_{\mathrm{mode}}}\right]$, $\bar{\boldsymbol{B}} = \left[\bar{B}_1, \bar{B}_2, \ldots, \bar{B}_{n_{\mathrm{mode}}}\right]$ and $\boldsymbol{k}_{\mathrm{r}} = [k_{\mathrm{r}1}, k_{\mathrm{r}2}, \ldots, k_{\mathrm{r}n_{\mathrm{mode}}}]$.

The missing environmental knowledge makes it hard to estimate the number

of contributing modes n_{mode} precisely. When $\bar{\boldsymbol{A}}$ and $\bar{\boldsymbol{B}}$ are parts of the trainable parameters $\mathcal{T}$, we can conservatively set n_{mode} to an upper bound of its possible range and add L_1-norm regularization terms of $\bar{\boldsymbol{A}}$ and $\bar{\boldsymbol{B}}$ to encourage sparse solutions to aid model convergence. The loss function we used to train the trainable parameters is updated to:

$$L_{\mathrm{nk}}(r, z, y; \mathcal{T}_{\mathrm{nk}}) = |\hat{p}(r, z; \mathcal{T}_{\mathrm{nk}}) - y|^2 + \bar{\alpha} \left\| \bar{\boldsymbol{A}} \right\|_1 + \bar{\beta} \left\| \bar{\boldsymbol{B}} \right\|_1, \qquad (6.19)$$

where $\bar{\alpha}$ and $\bar{\beta}$ control the regularizations. With the trained optimal model parameters $\mathcal{T}_{\mathrm{nk}}^*$, we can predict acoustic fields in a non-isovelocity ocean waveguide with the knowledge of SSP using (6.7), (6.16) and (6.17).

6.3.2.2 Without knowledge of SSP

The detailed SSP across the water column is often unknown. The unknown SSP makes the calculation of $k_{\mathrm{z}m}(z)$ infeasible, even though the eigenvalue $k_{\mathrm{r}m}$ is provided. The MBNN is flexible to incorporate with standard NNs to model unknown physics. For example, we can implement a 1-input 1-output NN to model the unknown SSP. We name the NN that learns the SSP as *sound speed neural network* (SSNN).

In order to train the SSNN, the trainable parameter $\mathcal{T}$ defined in (6.18) is modified to:

$$\mathcal{T}_{\mathrm{nu}} \equiv \left(\bar{\boldsymbol{A}}, \bar{\boldsymbol{B}}, \boldsymbol{k}_{\mathrm{r}}, \boldsymbol{S} \right), \qquad (6.20)$$

where $\boldsymbol{S}$ contains all parameters (weights and bias) in the SSNN layer.
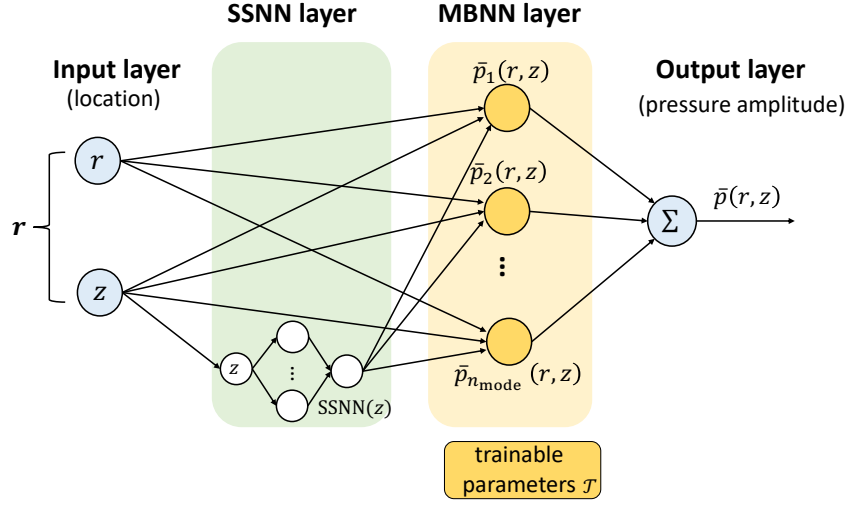
Figure 6.1: The computational graph for (6.7), (6.16) and (6.21) to estimate acoustic fields with unknown SSP.

Calculating $k_{zm}(z)$ is feasible now using the trained SSNN:

$$k_{zm}(z) = \sqrt{\left(\frac{\omega}{\text{SSNN}(z)}\right)^2 - k_{rm}^2}, \tag{6.21}$$

where $\text{SSNN}(z)$ is the estimated sound speed at depth z.

Fig. 6.1 illustrates the overall computation graph for (6.7), (6.16) and (6.21). We employ the same loss function defined in (6.19) to learn optimal $\mathcal{T}_{\text{nu}}^*$. With $\mathcal{T}_{\text{nu}}^*$, we can use (6.7) and (6.16) with (6.21) to predict acoustic fields in a non-isovelocity ocean waveguide without knowledge of SSP.

6.3.3 Generalization to other mode models

We have illustrated three MBNN formulations in range-independent ocean waveguides and demonstrated how flexible the proposed modeling framework is in different scenarios. It is worth noting that the exact formulations of normal mode models are application and environment specific. The idea of
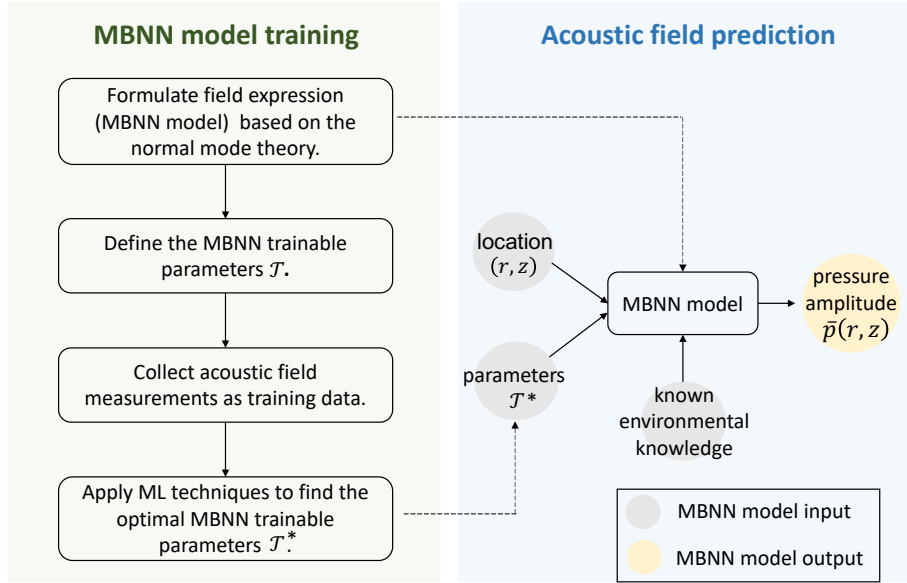
Figure 6.2: Key steps in the proposed MBNN framework in model training stage and field prediction stage.

our MBNN modeling framework can be applied to any variant of classical normal mode models. For example, the MBNN framework can incorporate the adiabatic mode methods or the coupled mode methods to model range-dependent environments [88], [172], [173].

Fig. 6.2 describes steps involved in the MBNN model training stage and field prediction stage. For any ocean waveguide, the key is to have an analytical field solution or an approximated field solution based on the normal mode theory, and use a small number of acoustic measurements as training data to find the optimal MBNN trainable parameters $\mathcal{T}^*$. We can calculate other necessary physical quantities based on the trained MBNN parameters so as to predict acoustic fields at locations of interest.
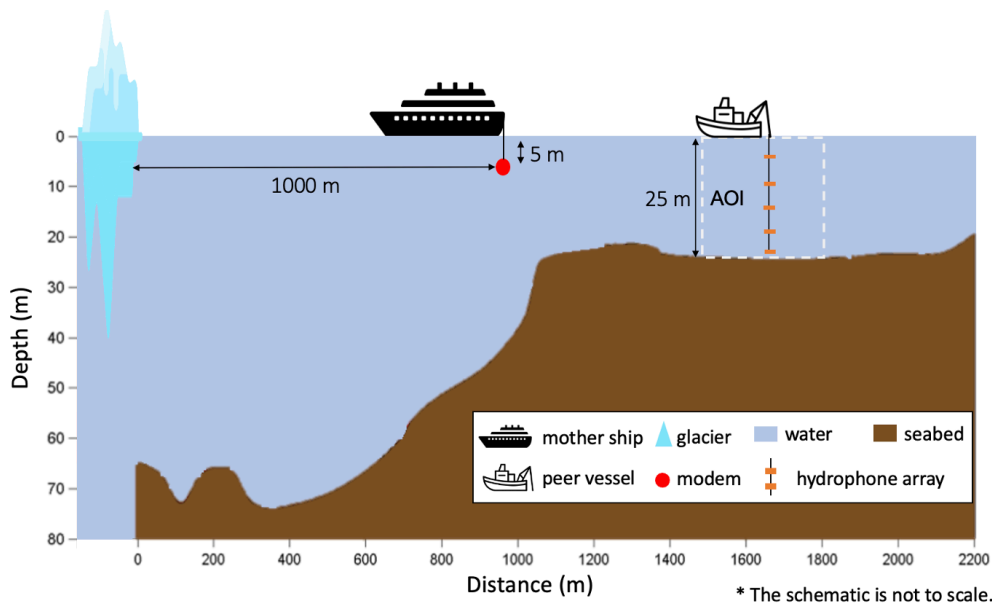
Figure 6.3: Schematic of the simulated environment at Hans Glacier.

6.4 Simulation studies

We simulate a real 2D ocean environment according to [174]. Work [174] provides a preliminary analysis of temporal variations of acoustic ray paths and the relationship between acoustic propagation and hydrological conditions at Hans Glacier front. This pilot study lays a foundation for a few follow-up studies at the Hans Glacier [175]–[177].

We assume that a mother ship anchors at a location 1,000 m from the glacier. It carries an acoustic modem that emits 500 Hz CW signals for acoustic communication and environmental monitoring. A peer survey vessel executes exploration tasks in a region that is much further away from the glacier. The bathymetry is approximately flat with a constant water depth of 25 m in the region in which the peer vessel operates. Fig. 6.3 depicts a schematic of the simulated environment at Hans Glacier. We use the Kraken normal

114

mode model [178] to generate synthetic acoustic measurements in the simulated environment. We randomly split the acoustic measurements* into a training dataset and a validation dataset based on a 70% : 30% ratio. We set the number of contributing modes n_{mode} as 30.

We consider a scenario where the bottom properties and boundary conditions are unknown. We aim to model acoustic field in the AOI in Section 6.4.1 and infer SSP using acoustic measurements collected at a nearly constant depth in Section 6.4.2. Such problems are not solvable using conventional normal mode models in partially unknown ocean waveguides.

6.4.1 Far-field acoustic field prediction

We consider two acoustic field prediction problems, one with known SSP and one with unknown SSP. We affix a hydrophone array to the peer survey vessel to collect acoustic field measurements in the AOM. It is preferred that we can accurately estimate nearby field patterns in which the vessel has not physically been. Therefore, we define 100 m regions on both sides of the AOM as the extended region to demonstrate field extrapolation performance. The AOM and the extended region form the AOI.

We benchmark the field prediction performance of the proposed MBNN framework against two classical data-driven ML techniques: GPR and DNN. We design a composite kernel of a squared exponential isotropic kernel and a Matérn 5/2 ARD kernel for GPR, and implement a 2-input 1-output DNN with three hidden layers and ReLU activation function. We randomly initialize the

---

*The synthetic acoustic measurements used in simulation studies are peak-to-peak values from hydrophone output in millivolts.

MBNN and the DNN model parameters in each run. The hyper-parameters of the GPR model are fine-tuned by minimizing validation error. We carry out 10 Monte Carlo simulations for MBNN and DNN models, and present the field prediction results with the smallest validation error.

6.4.1.1 Field prediction with knowledge of SSP

We consider an ocean waveguide with a known non-isovelocity SSP, unknown seabed properties and unknown boundary conditions. We use the WKB approximation to formulate the MBNN model based on (6.7), (6.16) and (6.17). We use acoustic measurements to find optimal trainable parameters $\mathcal{T}_{\mathrm{nk}}^*$ defined in (6.18).

The survey vessel performs three profiles, each spaced by a 1 m range in between, to collect acoustic measurements in a 2 m $\times$ 23 m AOM. Fig. 6.4 shows the ground truth field pattern in the AOI and locations of the three profiles where we collect the measurements. In order to investigate the field prediction performance, we use the Kraken model to generate 464,600 test data with a resolution of 0.1 m in range and depth within the AOI. We investigate the data efficiency of the three models by estimating the field patterns in the AOI using measurements collected at one profile (24 measurements), two profiles (48 measurements) and three profiles (72 measurements) in the AOM.

Table 6.1 shows the estimated field patterns and corresponding RMS test errors in the AOI when different amounts of acoustic measurements are given as training data. Field patterns extrapolated using one profile measurements and two profiles measurements are not satisfactory due to insufficient training

116
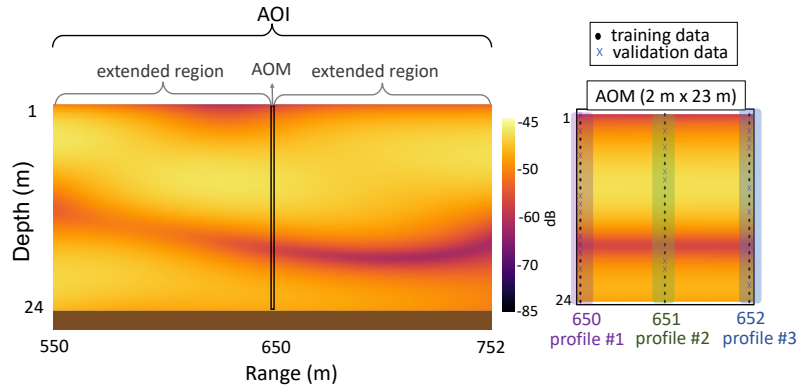
Figure 6.4: Ground truth field pattern in the AOI for field prediction application with known SSP.

TABLE 6.1: Acoustic field prediction performance of the three models using a different number of profile measurements in the field prediction application with known SSP.

Model	Estimated field pattern [RMS test error (mV_{pp})]		
	Profile #1[1]	Profile #1 & #2	Profile #1–#3
MBNN	[4.67]	[4.80]	[1.19]
GPR	[8.12]	[7.50]	[2.10]
DNN	[8.89]	[6.51]	[4.59]
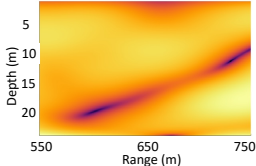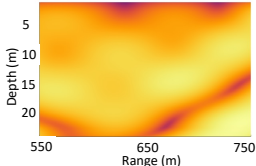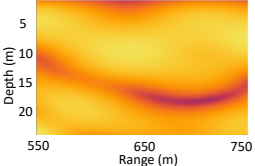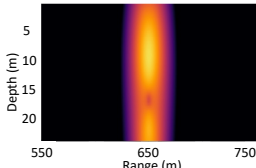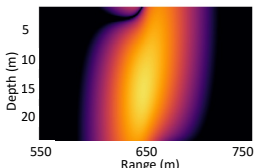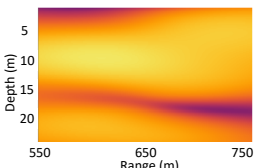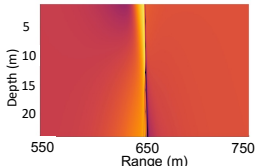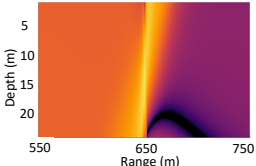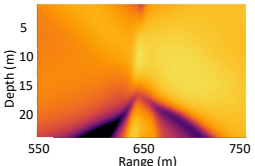
[1] Models are trained using acoustic measurements made at profile #1 (24 measurements).

data, especially for data-driven models. When the measurements made at three profiles are provided, the field estimated by the MBNN model aligns well with the ground truth field pattern. The GPR can extrapolate more details in the extended region. The DNN still performs poorly in extrapolation. The corresponding RMS test errors presented also justify our observations that the MBNN model outperforms the GPR and DNN models in terms of data efficiency and extrapolation performance.

6.4.1.2 Field prediction without knowledge of SSP

Sound speed in an ocean waveguide is measured by sending a CTD sensor at various depths. When either the CTD sensor or equipment to survey sound speed at various depths is lacking, we do not know the exact SSP. In this case, we assume that no sound speed measurement is available due to the lack of a CTD sensor. We only have a rough understanding of a reasonable range that the SSP may fall in. Our conservative initial guess of the SSP is that it falls in a 100 m/s range between 1,400 m/s and 1,500 m/s and SSP variation should not exceed 35 m/s over the 25 m water depth. We assume the detailed SSP and seabed properties are unknown. We use a simple 1-input 1-output NN (SSNN) with 1 hidden layer and ReLU activation function to learn the SSP in the water column. We formulate the MBNN model based on the WKB approximation according to (6.7), (6.16) and (6.21).

Intuitively, more acoustic data are required to train the MBNN framework as the size of trainable parameter $\mathcal{T}$ increases as compared to the previous scenario. As shown in Fig. 6.5, we uniformly collect 1,224 acoustic measurements
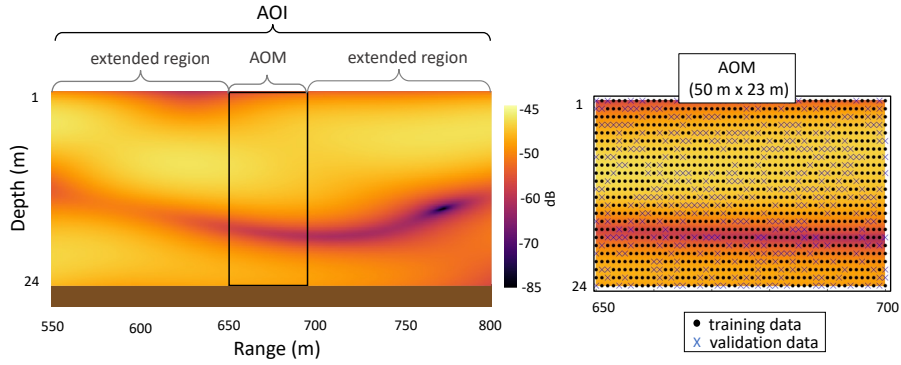
Figure 6.5: Ground truth field pattern in the AOI for field prediction application with unknown SSP.

(a) Ground truth

(b) Prediction by MBNN

(c) Prediction by GPR

(d) Prediction by DNN
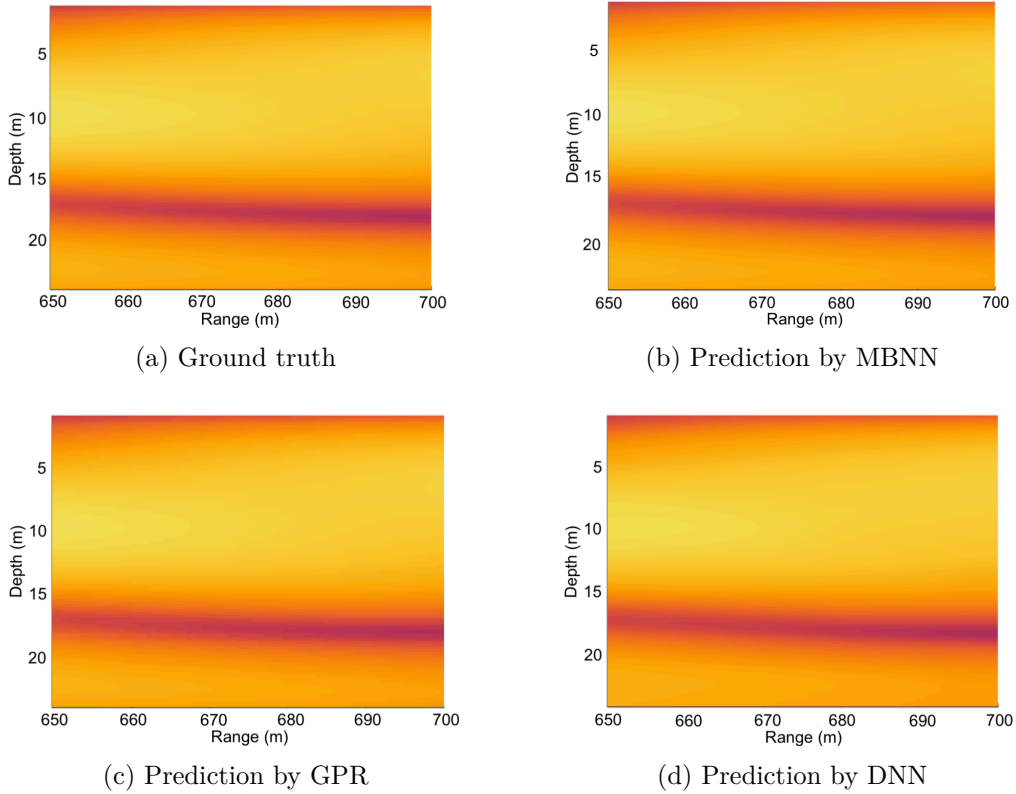
Figure 6.6: The estimated field patterns in the AOM when SSP is unknown. Panel (a) shows the ground truth field pattern. Panels (b)–(d) show the estimated fields by the MBNN, GPR and DNN models.

(24 measurements/profile × 51 profiles) within a 50 m × 23 m AOM. We aim to estimate the acoustic field pattern in the AOI by learning the optimal trainable

119

(a) Ground truth

(b) Extrapolation by MBNN

(c) Extrapolation by GPR

(d) Extrapolation by DNN
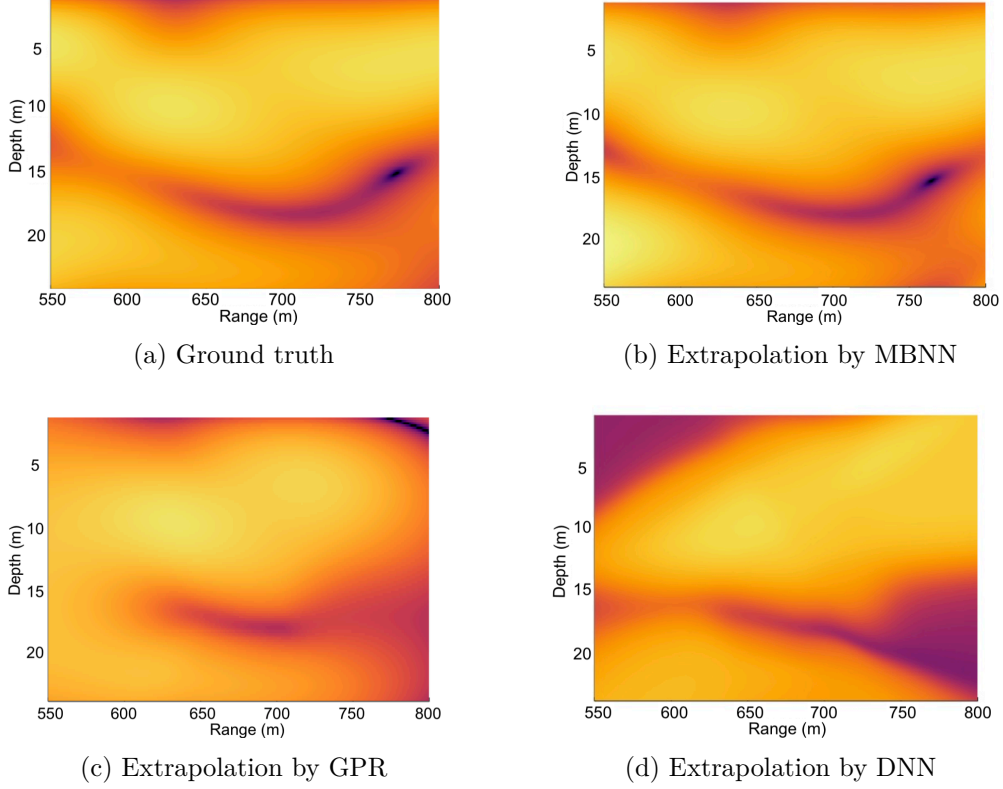
Figure 6.7: The estimated field patterns in the AOI when SSP is unknown. Panel (a) shows the ground truth field pattern. Panels (b)–(d) show the extrapolated fields by the MBNN, GPR and DNN models.

parameters $\mathcal{T}_{\mathrm{nu}}^*$ defined in (6.20) using 856 acoustic measurements as training data. We generate 575,000 acoustic measurements, with a resolution of 0.1 m in range and depth, as the test dataset over the AOI to rigorously quantify the field prediction performance.

As shown in Fig. 6.6, all of the three models can interpolate acoustic fields in the AOM well. Field patterns extrapolated in the extended region shown in Fig. 6.7 highlight the superiority of our proposed MBNN framework over the GPR and DNN models. The test errors listed in Table 6.2 support the observations we draw from Fig. 6.6 and Fig. 6.7. Although learning of the SSP

120

TABLE 6.2: Acoustic field prediction performance of the three models in the field prediction application with unknown SSP.

Model	RMS test error (mV_{pp})	
	In AOM	In AOI
MBNN	0.039	0.87
GPR	0.011	2.10
DNN	0.10	2.88
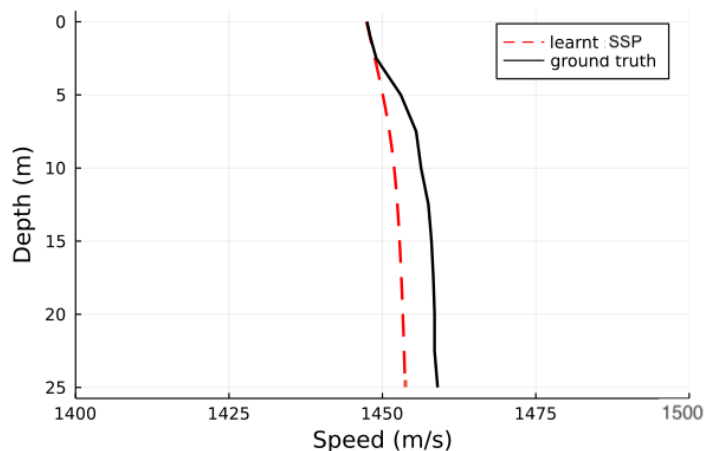
Figure 6.8: The learnt SSP with the ground truth SSP in the field prediction application. The SSNN is trained using profile measurements sampled across the water column in the AOM.

is of no interest to the field prediction problem, the SSP learnt by the SSNN is close to the ground truth SSP in the 100 m/s span as shown in Fig. 6.8. It demonstrates the flexibility of the MBNN model to incorporate with standard NNs to model unknown physics.

6.4.2 Inversion of SSP

In Section 6.4.1.2, we have demonstrated that our proposed MBNN model can learn the SSP reasonably well using the acoustic field measurements collected at 51 profiles when a CTD sensor is not provided. If a CTD sensor is available, we

can directly measure sound speeds at all depths while an AUV performs profiles across the water column. However, it is no longer doable if the AUV operates at a constant depth in missions. The AUV can only measure sound speeds at depths it operates. Can we inverse the entire SSP using acoustic field measurements collected at a nearly constant depth? Conventional normal mode models cannot address this interesting problem.

We assume an AUV, equipped with a hydrophone and a CTD sensor, is deployed from the water surface. It dives to an operating depth of 4 m in a 4 m range and operates at a constant depth of 4 m for the next 196 m. Fig. 6.9 indicates the AUV's trajectory on top of the ground truth field pattern in the AOM. The AUV uniformly makes acoustic field measurements as it operates in the AOM. The AUV uniformly makes five sound speed measurements at depths between the water surface and the operating depth. We aim to learn the entire SSP using the acoustic field measurements collected at a nearly constant depth with the aid of a few sound speed measurements made at shallow depths.
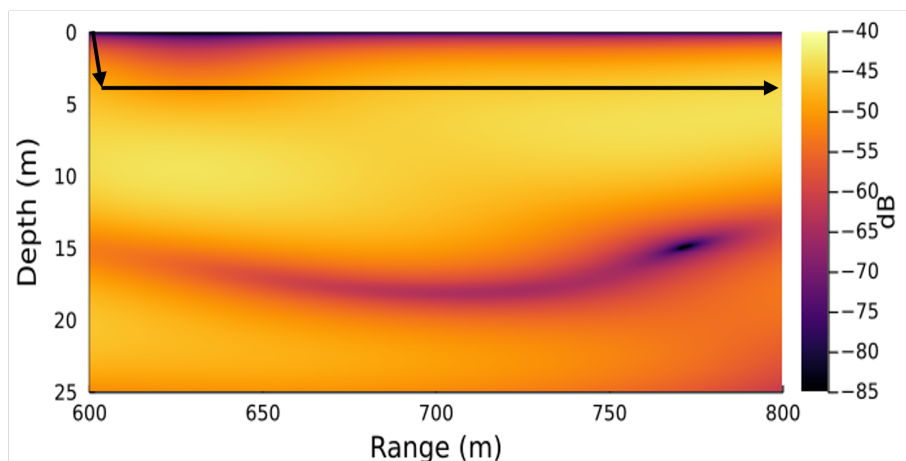
Figure 6.9: The trajectory of AUV labelled as an arrow on top of the ground truth field pattern in the AOM in the SSP inversion application.

122
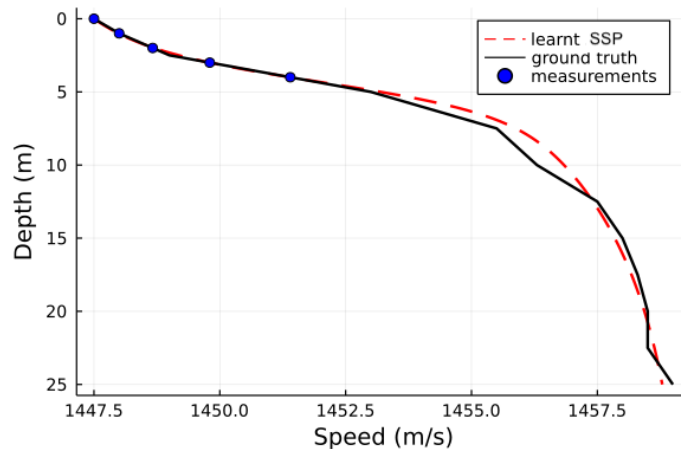
Figure 6.10: The learnt SSP with the ground truth SSP in the SSP inversion application using acoustic measurements made at a nearly constant depth and a few sound speed measurements.

We assume boundary conditions and seabed properties are unknown. We use the same model formulation, trainable parameters and initial guess of the SSP defined in Section 6.4.1.2. The lack of strong spatial diversity in the collected field measurements makes this inversion problem particularly challenging.

The learnt SSP, benchmarked against the ground truth SSP, is shown in Fig. 6.10. We constrain the SSNN using the sound speed measurements made at the water surface, 1 m, 2 m, 3 m and 4 m in the loss function. The learnt SSP over 25 m depth is very close to the ground truth SSP, even for depths where no acoustic field measurement and sound speed measurement are provided. Training the MBNN model using acoustic measurements with stronger field variation can potentially reduce the number of training data required and improve the inversion accuracy.

6.5 Summary

In this chapter, we formulated the proposed modeling recipe based on the normal mode theory to address low-frequency modeling problems in ocean waveguides. We demonstrated the superiority of the proposed MBNN framework through field prediction problems by benchmarking against two classical ML techniques and illustrated its feasibility in a SSP inversion problem using acoustic measurements collected along a path with a nearly constant depth. The proposed RBNN and MBNN modeling frameworks can handle a wide range of underwater applications. In the next chapter, we will demonstrate an application example of the proposed hybrid modeling framework, showing how capable it is of solving practical problems that cannot be addressed by conventional models.

Chapter 7

Experimental Validation for Source Localization

In Chapter 1, we identified that the requirement of having accurate environmental knowledge in conventional propagation models poses practical challenges to modeling-related underwater applications. We specifically dived into the single-hydrophone source localization application as an example in Chapter 2. While the proposed adaptive path planning policy was shown to be effective for source localization in simulation, experimentally validating its performance remains necessary. Although we can demonstrate the algorithm in large underwater environments (e.g., oceans), making repeatable acoustic measurements is difficult in such environments because of time variability. As discussed in Chapter 5, the water tank provides us a well-controlled confined underwater environment and is suitable for small-scale experimental validation. The unknown tank wall reflection model makes it infeasible to implement the algorithm using conventional models. Fortunately, our proposed modeling recipe yields an effective modeling alternative for less understood underwater environments. To close the loop, we demonstrate the applicability of our RBNN modeling framework by experimentally validating the proposed source localization algorithm in the water tank using partial environmental knowledge.

(a) Side view

(b) Top view
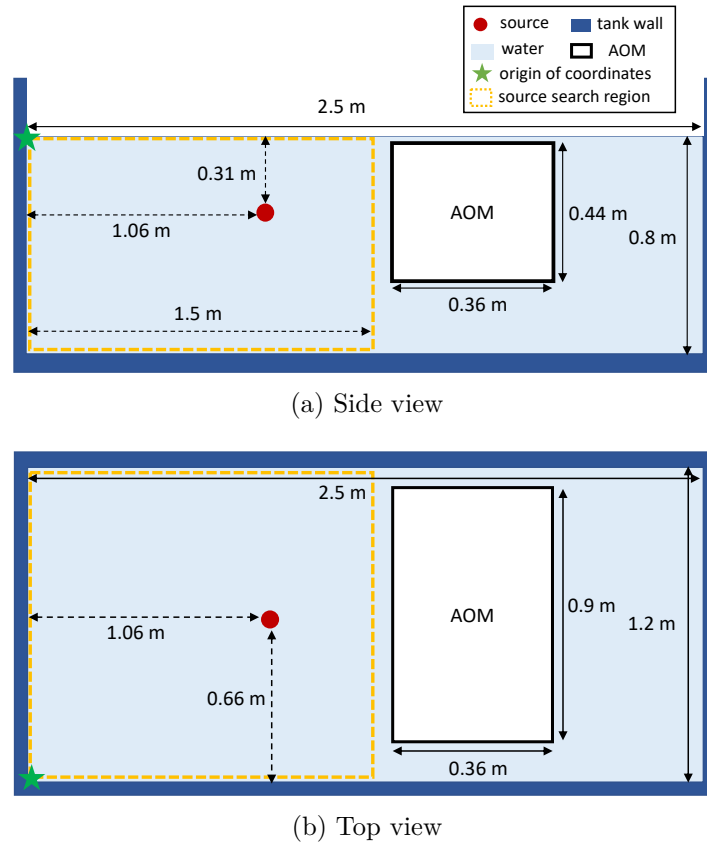
Figure 7.1: Schematic of the source localization validation experiment in the water tank.

7.1 Problem formulation

We aim to locate a static acoustic source in the cubic water tank within the shortest possible time. We use a moving hydrophone* to spatially sample acoustic fields at different locations within an AOM for source search. We know the tank geometry, but have no knowledge of the reflection model of all tank sidewalls. We employ the same tank setup described in Chapter 5 with the detailed schematic shown in Fig. 7.1. A 10 kHz acoustic source is located on

---

*For large underwater environments, the source localization algorithm should be validated by using a moving AUV equipped with a single hydrophone. In this small-scale tank, we use a moving hydrophone as a surrogate of an AUV.

the left-hand side of the water tank. Our prior knowledge of the source location confines a 1.5 m × 1.2 m × 0.8 m source search region that is highlighted as a yellow dashed box in Fig. 7.1.

We reuse the experimental acoustic measurements collected at the 500 locations within the 0.36 m × 0.9 m × 0.44 m AOM. These acoustic measurements constitute the training, validation and test dataset for modeling acoustic propagation in the tank in Section 5.4. Fig. 7.2 shows the 500 measurement locations in three plan views over the AOM to aid the visualization. The measurement locations form a full action space $\mathcal{A}'$ that contains all possible measurement locations which the hydrophone can move to throughout the source localization mission:

$$\mathcal{A}' = \{\boldsymbol{r}'_1, \boldsymbol{r}'_2, \cdots, \boldsymbol{r}'_{500}\}, \tag{7.1}$$

where $\boldsymbol{r}'_m$ represents the mth location.

As the proposed single-hydrophone source localization algorithm does not consider position mismatches, we correct the experimental measurement location $\boldsymbol{r}$ by the position error $\boldsymbol{r}_{\text{error}}$ trained in Section 5.4 to generate $\boldsymbol{r}'$:

$$\boldsymbol{r}'_m = \boldsymbol{r}_m + \boldsymbol{r}^m_{\text{error}}. \tag{7.2}$$

7.2 Method

7.2.1 Challenges in using conventional models

The proposed single-hydrophone source localization algorithm uses the MFP technique to locate an acoustic source. The MFP compares measurements with
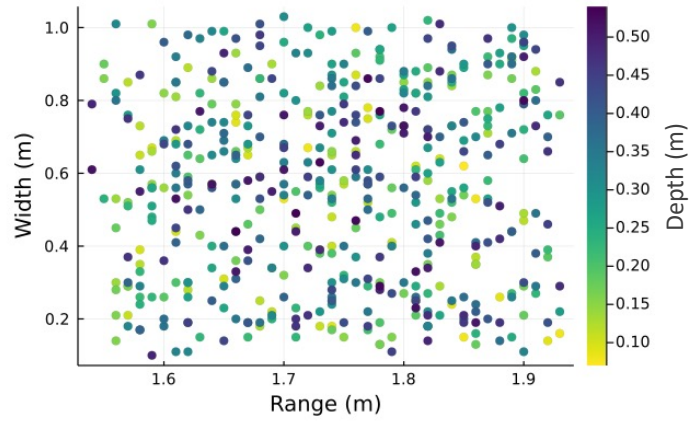
(a) Range-width plane (top view of tank)
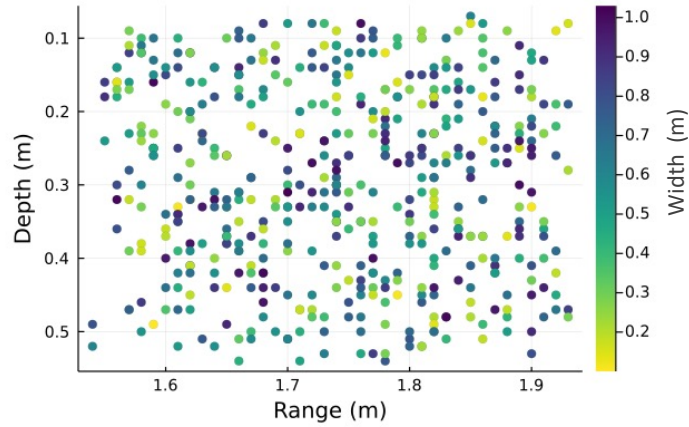
(b) Range-depth plane (side view of tank)
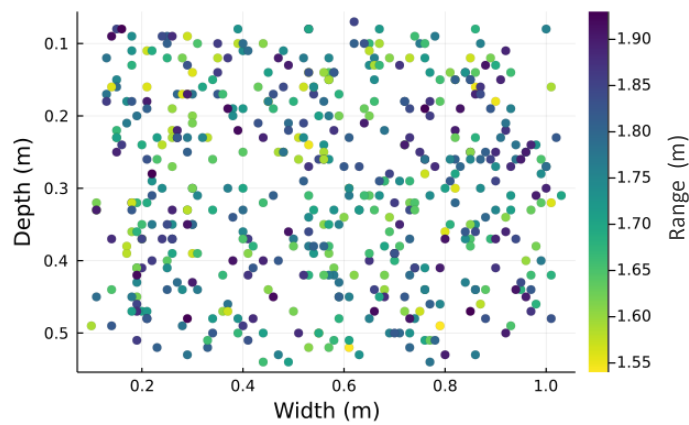
(c) Width-depth plane (side view of tank)

Figure 7.2: The 500 measurement locations in three plane views within the AOM.
The marker color indicates the location coordinate of the other dimension.

modeled replicas that are associated with all candidate source locations. As discussed in Chapter 3, conventional propagation models take environmental parameters and source location as model inputs and output estimated acoustic fields at locations of interest. Having completed and accurate environmental knowledge is the key to correctly generating modeled replicas in MFP using conventional propagation models. However, the tank is not well understood as the reflection model (reflection coefficient and phase shift) of tank sidewalls with respect to all possible incident angles is unknown and difficult to measure. A reflection coefficient at an incident angle can be calculated by measuring total transmission loss of an arrival that reflects on the reflecting surface once, and subtracting the absorption loss and geometric spreading loss out of the measured transmission loss. One can physically measure reflection coefficients at many incident angles and interpolate reflection coefficients at other angles to have a completed reflection model. Unfortunately, the tank is highly reverberant and the multipath arrivals overlap. It is therefore extremely difficult to separate the multipath arrivals to measure transmission loss of particular reflected paths, especially for a high frequency source in a small tank. This missing information stops us from practically validating the MFP-based source localization algorithm in the tank by means of conventional propagation models.

Although the robust source localization algorithm proposed in Section 2.3 copes with the effect of environmental mismatch, it focuses on individual physical parameters, rather than a physics model. If we know the physical form that governs acoustic reflections on the tank sidewalls and some physical parameters involved in the reflection calculation are uncertain. Our robust source

localization algorithm can include these uncertain parameters in the distribution update process to handle the environmental uncertainties. Alternatively, we can use geo-acoustic inversion methods to estimate geo-acoustic parameters of interest. However, neither the robust source localization algorithm nor geo-acoustic inversion techniques can infer unknown physics (e.g., full reflection model).

7.2.2   Inversion of tank sidewall reflection model

As demonstrated in Section 4.3.3, our proposed modeling recipe is flexible to incorporate with standard NNs to model unknown physics, such as the reflection model. To locate an acoustic source in the water tank, we design a two-stage implementation for the proposed MFP-based localization algorithm. The first stage targets learning unknown physics with the aid of the proposed modeling framework. For a given source location, a small number of acoustic measurements collected at various locations are used to train the sidewall reflection model (RCNN) through the proposed RBNN framework based on (4.19) and (4.22). The second stage focuses on source localization using the proposed adaptive path planning policy with the learnt reflection model and the proposed RBNN model. In practice, the source can be placed anywhere in the underwater environment while learning unknown physics in the initial stage. For simplification, we assume the source is located at the ground truth source location to make use of the learnt reflection model shown in Fig. 5.9.

7.2.3 Single-hydrophone source localization

We employ the adaptive path planning policy proposed in Chapter 2 to effectively locate the underwater source using measurements made from a single hydrophone. With the learnt reflection model, there is no environmental mismatch presented. For a given prior distribution of the source location, we adopt (2.3) to continuously update its posterior distribution whenever a new acoustic measurement is made. We use (2.4) and (2.5) to yield the next waypoint to maximize information gain of the source location at the current step. For scenarios with environmental uncertainties, we can easily utilize (2.7), (2.8) and (2.9) to mitigate the effects of environmental mismatch.

We benchmark the localization performance (time efficiency and localization accuracy) of the proposed adaptive path planning policy against two naive policies: random policy and *heuristic* policy. As illustrated in Fig. 7.2, the measurement locations in the predefined full action space $\mathcal{A}'$ are not uniformly spaced. At i^{th} planning step, the three policies sort out locations in $\mathcal{A}'$ that locate 0.05 m to 0.10 m from the current measurement location $\boldsymbol{r}_i'$ to constitute the current action space $\mathcal{A}(\boldsymbol{r}_i')$. The $\mathcal{A}(\boldsymbol{r}_i')$ comprises nearby locations that the hydrophone can move to for the next measurement. This makes sure step sizes of all policies are in a similar range. The random policy chooses its next waypoint $\boldsymbol{r}_{i+1}'$ from $\mathcal{A}(\boldsymbol{r}_i')$ randomly. The heuristic policy is designed based on heuristics that we want acoustic measurements to cover a large area in the AOM. It collects measurements along a path that is close to a zig-zag trajectory within the AOM.

For a fair compression, we perform five source localization missions and each

TABLE 7.1: Coordinates of initial locations used in the five source localization missions.

Mission	Range (m)	Width (m)	Depth (m)
#1	1.58	0.29	0.33
#2	1.93	0.29	0.48
#3	1.77	0.57	0.42
#4	1.66	0.66	0.18
#5	1.88	0.90	0.25

of them has a different initial location in the AOM (as listed in Table 7.1) for the hydrophone to begin with. The random policy involves randomness in the generated paths throughout the mission. For each of the five missions, we carry out 10 Monte Carlo runs for the random policy and present the average performance among 10 runs. The adaptive policy and heuristic policy are deterministic instead. Thus, we carry out one run for these two policies in each mission.

7.3 Results

We discretize the source search region with a resolution of 0.05 m in range, width and depth to make the validation computationally feasible. The discretized locations in the source search region are denoted as candidate source locations. We said the source is finalized if the source location distribution has converged[†]. We assume a uniform prior distribution among all candidate source locations. The proposed source localization algorithm can readily incorporate any prior knowledge of the source location to speed up the convergence. The ground truth

---

[†]The distribution of source location is said to be converged if its entropy drops below a threshold η for 5 consecutive steps
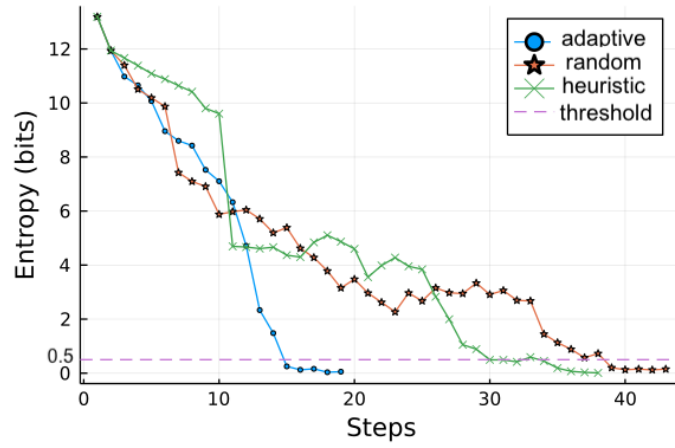
(a) Entropy history
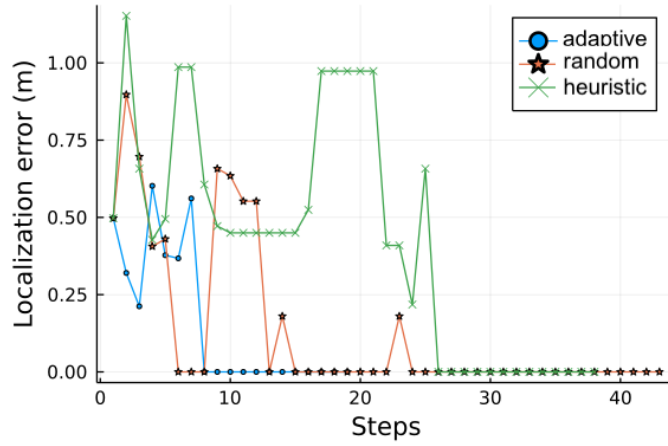
(b) Localization error history

Figure 7.3: Localization performance of the three policies in one run in the first mission. The threshold of convergence is set as 0.5 bits in this validation.

source location is at 1.06 m in range, 0.66 m in width and 0.31 m in depth. Due

to the discretization applied in the source search region, we said the source is

correctly located if the distribution of source location converges to the nearest

discretized candidate source location (1.05 m in range, 0.65 m in width and

0.30 m in depth) by the end of the search.

Fig. 7.3 shows the entropy history and localization error history from one run
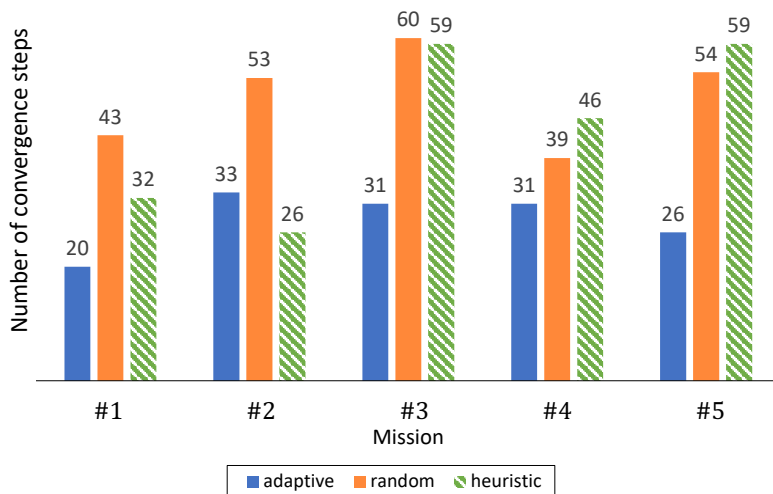
Figure 7.4: The average number of steps to make source location distribution converged in the five missions.

TABLE 7.2: The localization performance of the three path planning policies using experimental data in the five missions. The source coordinate we use to calculate the absolute localization error is based on 1.05 m in range, 0.65 in width and 0.30 m in depth due to the discretization of the candidate source locations.

Policy	Number of successes[1]					Absolute localization error[2](m)				
	#1	#2	#3	#4	#5	#1	#2	#3	#4	#5
Adaptive	1/1	1/1	1/1	1/1	1/1	0.00	0.00	0.00	0.00	0.00
Random	9/10	7/10	6/10	9/10	7/10	0.05	0.06	0.17	0.05	0.05
Heuristic	1/1	1/1	0/1	0/1	0/1	0.00	0.00	0.31	0.58	0.56

[1] Number of runs correctly locate the source / number of runs per mission.
[2] We calculate the mean absolute localization error over 10 runs for random policy.

in the first mission. We show the average number of convergence steps required

by the three policies in the five missions in Fig. 7.4. We also tabulate the number

of successes that a policy accurately locates the source by the end of the search

and the corresponding absolute localization error in Table 7.2. The adaptive

policy consistently outperforms the two naive policies in terms of time taken to

locate the source and the localization accuracy, except for the second mission.

7.4 Discussion

The heuristic policy has a higher chance to explore a wider horizon in the AOM where field variation may be stronger as compared to the other two policies. It potentially can converge faster than other naive policies (e.g., random policy). The result presented in Fig 7.4 agrees with this reasoning. As listed in Table 7.2, the random policy and the heuristic policy are inferior to the adaptive policy in terms of localization accuracy. The field measurements collected in the water tank contain random measurement errors. There could be multiple candidate source locations that produce very similar modeled replicas at the measurement locations. Such candidate source locations significantly confuse our MFP processor where the correct source is. The proposed adaptive policy avoids such a problem by planning its next move to the location with the most unique modeled replicas with respect to all candidate source locations. It thus can quickly reduce the ambiguity of source location and locate the source with high accuracy. In Fig 7.4, we observe that the heuristic policy locates the source faster than the adaptive policy in the second mission. This is because the current adaptive policy is yet greedy. Considering a few steps look-ahead while planning its next waypoint can mitigate this problem.

While we have successfully demonstrated the proposed adaptive policy through a controlled experiment in conjunction with the proposed RBNN framework, our RBNN framework itself has the potential to directly solve the underwater source localization problem in partially unknown environments. We briefly address this idea in Section 8.2.

7.5 Summary

The MFP-based source localization algorithm proposed in Chapter 2 employs propagation models to generate modeled replicas for comparison. Conventional propagation models fail to operate if any required environmental parameter is missing, making the experimental validation of the proposed source localization algorithm infeasible in a partially unknown environment. Such a practical limitation of conventional models motivates our research. Our proposed hybrid modeling recipe bridges the gap and provides us a feasible modeling alternative. With the aid of the proposed RBNN framework, in this chapter, we validated the effectiveness of the proposed adaptive path planning policy for single-hydrophone underwater source localization using the experimental data collected in a partially unknown water tank. The implications of our proposed modeling recipe are not limited to the specific underwater applications we have demonstrated in this thesis. Our modeling recipe can be easily customized to tackle a wide range of modeling-related underwater applications.

Chapter 8

Conclusions and Future Research

8.1 Conclusions

Modeling acoustic propagation in underwater environments is useful for numerous underwater applications. However, it is particularly challenging in partially unknown environments. Conventional physics-based propagation models use accurate environmental parameters to predict acoustic propagation in operating environments. Their practical uses are inherently limited by the availability of prior environmental knowledge. Data-driven ML techniques allow us to predict acoustic fields through acoustic observations. While they do not require any environmental information, they are data-hungry and extrapolate poorly. They can also make predictions that are physically unrealistic.

A recent advance, named SciML, embeds scientific domain knowledge into data-driven ML to leverage the complementary strengths of both of them. In this thesis, we proposed a physics-based data-aided hybrid propagation modeling recipe motivated by the idea of SciML. The proposed modeling recipe can learn from very little data, extrapolate well beyond the region where training data are available, and always make predictions that are consistent with physics. It also can easily incorporate environmental complexities such as non-isovelocity SSP and various geo-acoustic models. When the physics is fully or partially

known, explicit expressions can be included in the computational graph, with potentially some unknown parameters. On the other hand, when physics is unknown, NNs can be used as components of the computational graph to model arbitrary functions. The resulting computational graph can be automatically differentiated with respect to the model parameters, thus making it suitable for training with standard gradient-descent based NN training algorithms.

We employed the acoustic wave equation as underlying domain knowledge to structurally constrain the learning of model unknowns in the proposed modeling recipe. We specifically utilized the ray theory to formulate the RBNN framework that offers a high-frequency acoustic propagation modeling framework out of the proposed recipe. We also implemented the MBNN framework based on the normal mode theory for low-frequency oceanic applications. We demonstrated a few applications of the RBNN and MBNN frameworks, highlighting the flexibilities they can provide in modeling acoustic propagation scenarios with varying degrees of environmental complexity and knowledge. The proposed modeling recipe is capable to solve some practical problems that cannot be addressed by conventional models. For example, we applied the RBNN framework to successfully model acoustic propagation in a highly reverberant water tank with an unknown sidewall reflection model. The water tank is an acoustically complicated confined water environment that cannot be modeled by state of the arts easily. With the proposed RBNN framework, we experimentally demonstrated the proposed adaptive path planning policy for single-hydrophone source localization in the water tank under partial environmental knowledge.

8.2 Future research

This section lays out some future research directions we can pursue, which either relax assumptions made throughout the thesis or serve as natural extensions of current work.

- **Frequency-aided hybrid modeling recipe for field prediction:**

  The studies evaluated in this thesis consider an acoustic source that emits a single-frequency CW signal. For underwater applications that operate over a frequency band, we can make use of the physics information encoded in the received signals over the frequency band to effectively reduce the number of measurement locations required. This idea can be applied to all RBNN and MBNN formulations discussed in this thesis.

- **Path planning of AUVs under communication constraints:**

  The communication and navigation performance of a moving AUV is highly viable due to complicated constructive and destructive interference patterns in underwater environments. If the environment is well understood, we can plan AUVs' paths offline using conventional propagation models to make AUVs operate in regions with low transmission losses. However, this is not doable if any environmental parameter is missing. Our proposed modeling recipe solves such a problem. We can predict transmission losses at nearby locations of AUVs using the proposed modeling frameworks and adaptively plan their paths to maintain reliable communication and navigation performance throughout the mission.

- **Modeling effects of time variability:**

  Our current work assumes a static underwater environment. Environments may change over time (e.g., tidal variation). If environmental changes can be modeled as functions of time, we can include effects of time variability in operating environments in our modeling framework. This will broaden the applicability of our proposed modeling recipe to cope with real underwater environments.

- **Sensitivity analysis and error modeling:**

  Errors in model parameters directly affect the prediction accuracy of our hybrid propagation models. Systematically modeling error propagation in the proposed modeling frameworks and carrying out detailed model sensitivity analyses will be practically valuable for model design and implementation.

- **Inverse RBNN for source localization:**

  The proposed RBNN modeling framework can be transformed into a source localization method. Once the RBNN model is trained using a set of acoustic measurements, we can trace back along trajectories of contributing rays based on knowledge of channel geometry. The location that all trajectories pass through is the source location. This source localization method does not require full environmental knowledge.

Bibliography

[1] L. Whitcomb, D. R. Yoerger, H. Singh, and J. Howland, "Advances in underwater robot vehicles for deep ocean exploration: Navigation, control, and survey operations," in *Robotics Research*. Springer, 2000, pp. 439–448.

[2] G. Ferri, A. Munafò, A. Tesei, P. Braca, F. Meyer, K. Pelekanakis, R. Petroccia, J. Alves, C. Strode, and K. LePage, "Cooperative robotic networks for underwater surveillance: an overview," *IET Radar, Sonar & Navigation*, vol. 11, no. 12, pp. 1740–1761, 2017.

[3] S. Venkatesan, "AUV for search & rescue at sea-an innovative approach," in *2016 IEEE/OES Autonomous Underwater Vehicles (AUV)*. IEEE, 2016, pp. 1–9.

[4] Y. Sato, T. Maki, T. Matsuda, and T. Sakamaki, "Detailed 3D seafloor imaging of Kagoshima bay by AUV Tri-TON2," in *2015 IEEE Underwater Technology (UT)*. IEEE, 2015, pp. 1–6.

[5] K. Wang, H. Gao, X. Xu, J. Jiang, and D. Yue, "An energy-efficient reliable data transmission scheme for complex environmental monitoring in underwater acoustic sensor networks," *Sensors*, vol. 16, no. 11, pp. 4051–4062, 2015.

[6] E. Jimenez, G. Quintana, P. Mena, P. Dorta, I. Perez-Alvarez, S. Zazo, M. Perez, and E. Quevedo, "Investigation on radio wave propagation in shallow seawater: Simulations and measurements," in *2016 IEEE Third Underwater Communications and Networking Conference (UComms)*. IEEE, 2016, pp. 1–5.

[7] L. Wang, K. Heaney, T. Pangerc, P. Theobald, S. Robinson, and M. Ainslie, "Review of underwater acoustic propagation models." National Physical Laboratory, Tech. Rep., 2014.

[8] ARL. Acoustics toolbox. Accessed 2022-06-10. [Online]. Available: https://github.com/org-arl/AcousticsToolbox.jl

[9] K. R. James and D. R. Dowling, "A method for approximating acoustic-field-amplitude uncertainty caused by environmental uncertainties," *The Journal of the Acoustical Society of America*, vol. 124, no. 3, pp. 1465–1476, 2008.

[10] S. Gul, S. S. H. Zaidi, R. Khan, and A. B. Wala, "Underwater acoustic channel modeling using bellhop ray tracing method," in *2017 14th International Bhurban Conference on Applied Sciences and Technology (IBCAST)*. IEEE, 2017, pp. 665–670.

[11] J. Llor and M. P. Malumbres, "Underwater wireless sensor networks: how do acoustic propagation models impact the performance of higher-level protocols?" *Sensors*, vol. 12, no. 2, pp. 1312–1335, 2012.

[12] N. R. Chapman, "Inverse problems in underwater acoustics," in *Handbook of Signal Processing in Acoustics*. Springer New York, 2008, pp. 1723–1735.

[13] N. R. Chapman, S. Chin-Bing, D. King, and R. B. Evans, "Benchmarking geoacoustic inversion methods for range-dependent waveguides," *IEEE journal of oceanic engineering*, vol. 28, no. 3, pp. 320–330, 2003.

[14] S. Dosso, M. Yeremy, J. Ozard, and N. Chapman, "Estimation of ocean-bottom properties by matched-field inversion of acoustic field data," *IEEE Journal of Oceanic Engineering*, vol. 18, no. 3, pp. 232–239, 1993.

[15] J. Bonnel, B. Nicolas, J. I. Mars, and S. C. Walker, "Estimation of modal group velocities with a single receiver for geoacoustic inversion in shallow water," *The Journal of the Acoustical Society of America*, vol. 128, no. 2, pp. 719–727, 2010.

[16] M. Collins and W. Kuperman, "Inverse problems in ocean acoustics," *Inverse Problems*, vol. 10, no. 5, 1994.

[17] P. K. LeHardy and C. Moore, "Deep ocean search for Malaysia airlines flight 370," in *2014 Oceans-St. John's*. IEEE, 2014, pp. 1–4.

[18] T. de Castella. Malaysia plane: Why black boxes can't always provide the answers. Accessed 2022-06-10. [Online]. Available: https://www.bbc.com/news/magazine-26721975

[19] A. B. Baggeroer, W. Kuperman, and H. Schmidt, "Matched field processing: Source localization in correlated noise as an optimum parameter estimation problem," *The Journal of the Acoustical Society of America*, vol. 83, no. 2, pp. 571–587, 1988.

[20] N. R. Chapman and E. C. Shang, "Review of geoacoustic inversion in underwater acoustics," *Journal of Theoretical and Computational Acoustics*, vol. 29, no. 3, 2021.

[21] C. W. Holland, J. Dettmer, and S. E. Dosso, "Remote sensing of sediment density and velocity gradients in the transition layer," *The Journal of the Acoustical Society of America*, vol. 118, no. 1, pp. 163–177, 2005.

[22] M. R. Khan, B. Das, and B. B. Pati, "Channel estimation strategies for underwater acoustic (UWA) communication: An overview," *Journal of the Franklin Institute*, vol. 357, no. 11, pp. 7229–7265, 2020.

[23] M. I. Jordan and T. M. Mitchell, "Machine learning: Trends, perspectives, and prospects," *Science*, vol. 349, no. 6245, pp. 255–260, 2015.

[24] I. Goodfellow, Y. Bengio, and A. Courville, "Machine learning basics," *Deep learning*, vol. 1, no. 7, pp. 98–164, 2016.

[25] H. Yang, K. Lee, Y. Choo, and K. Kim, "Underwater acoustic research trends with machine learning: general background," *Journal of Ocean Engineering and Technology*, vol. 34, no. 2, pp. 147–154, 2020.

[26] J. Bernardo, J. Berger, A. Dawid, A. Smith *et al.*, "Regression and classification using Gaussian process priors," *Bayesian statistics*, vol. 6, pp. 475–486, 1998.

[27] W. Liu, Z. Wang, X. Liu, N. Zeng, Y. Liu, and F. E. Alsaadi, "A survey of deep neural network architectures and their applications," *Neurocomputing*, vol. 234, pp. 11–26, 2017.

[28] A. Karpatne, G. Atluri, J. H. Faghmous, M. Steinbach, A. Banerjee, A. Ganguly, S. Shekhar, N. Samatova, and V. Kumar, "Theory-guided data science: A new paradigm for scientific discovery from data," *IEEE Transactions on Knowledge and Data Engineering*, vol. 29, no. 10, p. 2318–2331, Oct 2017.

[29] F. B. Jensen, W. A. Kuperman, M. B. Porter, and H. Schmidt, "Wave propagation theory," in *Computational Ocean Acoustics.* Springer New York, 2011, pp. 65–153.

[30] F. B. Jensen, W. A. Kuperman, M. B. Porter, and H. Schmidt, "Ray methods," in *Computational Ocean Acoustics.* Springer New York, 2011, pp. 155–232.

[31] F. B. Jensen, W. A. Kuperman, M. B. Porter, and H. Schmidt, "Normal modes," in *Computational Ocean Acoustics.* Springer New York, 2011, pp. 337–455.

[32] K. Li and M. Chitre, "Informative path planning for source localization," in *International Conference on Robotics and Automation (ICRA) Workshop on Sound Source Localization and Its Applications for Robots*, 2019.

[33] K. Li and M. Chitre, "Informative path planning for acoustic source localization with environmental uncertainties," in *Global Oceans 2020: Singapore–US Gulf Coast.* IEEE, 2020, pp. 1–5.

[34] B. M. Worthmann, H. Song, and D. R. Dowling, "High frequency source localization in a shallow ocean sound channel using frequency difference matched field processing," *The Journal of the Acoustical Society of America*, vol. 138, no. 6, pp. 3549–3562, 2015.

[35] J. C. Chen, K. Yao, and R. E. Hudson, "Acoustic source localization and beamforming: theory and practice," *journal on advances in signal processing*, vol. 2003, no. 4, pp. 1–12, 2003.

[36] A. B. Baggeroer and W. A. Kuperman, "Matched field processing in ocean acoustics," in *Acoustic Signal Processing for Ocean Exploration.* Springer, 1993, pp. 79–114.

[37] J. Smith and J. Abel, "Closed-form least-squares source location estimation from range-difference measurements," *IEEE Transactions on Acoustics, Speech, and Signal Processing*, vol. 35, no. 12, pp. 1661–1669, 1987.

[38] G. Mellen, M. Pachter, and J. Raquet, "Closed-form solution for determining emitter location using time difference of arrival measurements," *IEEE Transactions on Aerospace and Electronic Systems*, vol. 39, no. 3, pp. 1056–1058, 2003.

[39] Y. Wang and H. Peng, "Underwater acoustic source localization using generalized regression neural network," *The Journal of the Acoustical Society of America*, vol. 143, no. 4, pp. 2321–2331, 2018.

[40] H. Krim and M. Viberg, "Two decades of array signal processing research: the parametric approach," *IEEE signal processing magazine*, vol. 13, no. 4, pp. 67–94, 1996.

[41] A. Xenaki, P. Gerstoft, and K. Mosegaard, "Compressive beamforming," *The Journal of the Acoustical Society of America*, vol. 136, no. 1, pp. 260–271, 2014.

[42] X. Wang, S. Khazaie, L. Margheri, and P. Sagaut, "Shallow water sound source localization using the iterative beamforming method in an image framework," *Journal of Sound and Vibration*, vol. 395, pp. 354–370, 2017.

[43] H. P. Bucker, "Use of calculated sound fields and matched-field detection to locate sound sources in shallow water," *The Journal of the Acoustical Society of America*, vol. 59, no. 2, pp. 368–373, 1976.

143

[44] A. Richardson and L. Nolte, "A posteriori probability source localization in an uncertain sound speed, deep ocean environment," *The Journal of the Acoustical Society of America*, vol. 89, no. 5, pp. 2280–2284, 1991.

[45] M. D. Collins and W. Kuperman, "Focalization: Environmental focusing and source localization," *The Journal of the Acoustical Society of America*, vol. 90, no. 3, pp. 1410–1422, 1991.

[46] K. V. Mackenzie, "Discussion of sea water sound-speed determinations," *The Journal of the Acoustical Society of America*, vol. 70, no. 3, pp. 801–806, 1981.

[47] C. R. Berger, S. Zhou, P. Willett, and L. Liu, "Stratification effect compensation for improved underwater acoustic ranging," *IEEE Transactions on Signal Processing*, vol. 56, no. 8, pp. 3779–3783, 2008.

[48] S. Poursheikhali and H. Zamiri-Jafarian, "TDOA based target localization in inhomogenous underwater wireless sensor network," in *2015 5th International Conference on Computer and Knowledge Engineering (ICCKE)*. IEEE, 2015, pp. 1–6.

[49] B. Z. Steinberg, M. J. Beran, S. H. Chin, and J. H. Howard Jr, "A neural network approach to source localization," *The Journal of the Acoustical Society of America*, vol. 90, no. 4, pp. 2081–2090, 1991.

[50] J. M. Ozard, P. Zakarauskas, and P. Ko, "An artificial neural network for range and depth discrimination in matched field processing," *The Journal of the Acoustical Society of America*, vol. 90, no. 5, pp. 2658–2663, 1991.

[51] H. Niu, E. Reeves, and P. Gerstoft, "Source localization in an ocean waveguide using supervised machine learning," *The Journal of the Acoustical Society of America*, vol. 142, no. 3, pp. 1176–1188, 2017.

[52] Z. Huang, J. Xu, Z. Gong, H. Wang, and Y. Yan, "Source localization using deep neural networks in a shallow water environment," *The Journal of the Acoustical Society of America*, vol. 143, no. 5, pp. 2922–2932, 2018.

[53] Y. Liu, H. Niu, and Z. Li, "A multi-task learning convolutional neural network for source localization in deep ocean," *The Journal of the Acoustical Society of America*, vol. 148, no. 2, pp. 873–883, 2020.

[54] S. Li and C. Clay, "Optimum time domain signal transmission and source location in a waveguide: Experiments in an ideal wedge waveguide," *The Journal of the Acoustical Society of America*, vol. 82, no. 4, pp. 1409–1417, 1987.

[55] L. N. Frazer and P. I. Pecholcs, "Single-hydrophone localization," *The Journal of the Acoustical Society of America*, vol. 88, no. 2, pp. 995–1002, 1990.

[56] S. M. Jesus, M. B. Porter, Y. Stéphan, X. Démoulin, O. C. Rodríguez, and E. M. F. Coelho, "Single hydrophone source localization," *IEEE Journal of Oceanic Engineering*, vol. 25, no. 3, pp. 337–346, 2000.

[57] J. B. Weng and Y. M. Yang, "Experimental demonstration of shadow zone localization using deep water interference patterns measured by a single hydrophone," *IEEE Journal of Oceanic Engineering*, vol. 43, no. 4, pp. 1171–1178, 2017.

[58] T. Zhang, G. Han, M. Guizani, L. Yan, and L. Shu, "Peak extraction passive source localization using a single hydrophone in shallow water," *IEEE Transactions on Vehicular Technology*, vol. 69, no. 3, pp. 3412–3423, 2020.

[59] H. Niu, Z. Gong, E. Ozanich, P. Gerstoft, H. Wang, and Z. Li, "Deep-learning source localization using multi-frequency magnitude-only data," *The Journal of the Acoustical Society of America*, vol. 146, no. 1, pp. 211–222, 2019.

[60] Y. Liu, H. Niu, Z. Li, and M. Wang, "Deep-learning source localization using autocorrelation functions from a single hydrophone in deep ocean," *Journal of the Acoustical Society of America*, vol. 1, no. 3, 2021.

[61] M. B. Porter, "The bellhop manual and user's guide: Preliminary draft," *Heat, Light, and Sound Research*, vol. 260, 2011.

[62] G. M. Wenz, "Acoustic ambient noise in the ocean: Spectra and sources," *The Journal of the Acoustical Society of America*, vol. 34, no. 12, pp. 1936–1956, 1962.

[63] K. V. Mackenzie, "Nine-term equation for sound speed in the oceans," *The Journal of the Acoustical Society of America*, vol. 70, no. 3, pp. 807–812, 1981.

[64] F. B. Jensen, W. A. Kuperman, M. B. Porter, and H. Schmidt, "Fundamentals of ocean acoustics," in *Computational Ocean Acoustics*. Springer New York, 2011, pp. 1–64.

[65] Minimate hydrophones. Accessed 2022-06-10. [Online]. Available: https://durhamgeo.com/product/minimate-hydrophones/

[66] Ultra maritime. Accessed 2022-06-10. [Online]. Available: https://www.ultra.group/our-business-units/maritime/sonar-systems/towed-sonar/

[67] J. Chen, F. Duan, J. Jiang, Y. Li, and X. Hua, "Offshore towed hydrophone linear array: principle, application, and data acquisition results," *Journal on Wireless Communications and Networking*, vol. 2013, no. 1, pp. 1–7, 2013.

[68] L. Brekhovskikh and Y. P. Lysanov, "Reflection of sound from the surface and bottom of the ocean: Plane waves," in *Fundamentals of Ocean Acoustics*. Springer New York, 2003, pp. 61–79.

[69] M. Stojanovic, "On the relationship between capacity and distance in an underwater acoustic communication channel," *ACM SIGMOBILE Mobile Computing and Communications Review*, vol. 11, no. 4, pp. 34–43, 2007.

[70] M. Schulkin and H. Marsh, "Sound absorption in sea water," *The Journal of the Acoustical Society of America*, vol. 34, no. 6, pp. 864–865, 1962.

[71] W. Thorp and D. Browning, "Attenuation of low frequency sound in the ocean," *Journal of Sound Vibration*, vol. 26, no. 4, pp. 576–578, 1973.

[72] D. A. Abraham, "Underwater acoustics," in *Underwater Acoustic Signal Processing: Modeling, Detection, and Estimation*. Springer, 2019, pp. 95–199.

[73] W. Kuperman, "Acoustics, deep ocean," in *Encyclopedia of Ocean Sciences*. Academic Press, 2001, pp. 61–72.

[74] K. H. Talib, M. Y. Othman, S. A. H. Sulaiman, M. A. M. Wazir, and A. Azizan, "Determination of speed of sound using empirical equations and svp," in *2011 IEEE 7th International Colloquium on Signal Processing and its Applications.* IEEE, 2011, pp. 252–256.

[75] M. Stojanovic and J. Preisig, "Underwater acoustic communication channels: Propagation models and statistical characterization," *IEEE communications magazine*, vol. 47, no. 1, pp. 84–89, 2009.

[76] P. C. Etter, "Introduction," in *Underwater acoustic modeling and simulation.* CRC press, 2003.

[77] F. B. Jensen, W. A. Kuperman, M. B. Porter, and H. Schmidt, "Wavenumber integration techniques," in *Computational Ocean Acoustics.* Springer New York, 2011, pp. 233–335.

[78] F. B. Jensen, W. A. Kuperman, M. B. Porter, and H. Schmidt, "Parabolic equations," in *Computational Ocean Acoustics.* Springer New York, 2011, pp. 457–529.

[79] F. B. Jensen, W. A. Kuperman, M. B. Porter, and H. Schmidt, "Finite differences and finite elements," in *Computational Ocean Acoustics.* Springer New York, 2011, pp. 531–610.

[80] A.-C. Hladky-Hennion, "Finite element analysis of the propagation of acoustic waves in waveguides," *Journal of Sound and Vibration*, vol. 194, no. 2, pp. 119–136, 1996.

[81] CMST. Underwater acoustic software. Accessed 2022-06-10. [Online]. Available: http://cmst.curtin.edu.au/products/underwater/

[82] M. B. Porter, "The kraken normal mode program," Naval Research Lab Washington DC, Tech. Rep., 1992.

[83] P. G. Bergmann and L. Spitzer, "The physics of sound in the sea," Office of Scientific Research and Development Washington DC, Tech. Rep., 1946.

[84] C. B. Officer, "Introduction to the theory of sound transmission," *Reflectivity*, vol. 12, no. 12, 1958.

[85] M. B. Porter and H. P. Bucker, "Gaussian beam tracing for computing ocean acoustic fields," *The Journal of the Acoustical Society of America*, vol. 82, no. 4, pp. 1349–1359, 1987.

[86] M. B. Porter, "Beam tracing for two-and three-dimensional problems in ocean acoustics," *The Journal of the Acoustical Society of America*, vol. 146, no. 3, pp. 2016–2029, 2019.

[87] C. L. Pekeris, "Theory of propagation of explosive sound in shallow water," in *Propagation of Sound in the Ocean.* Geological Society of America, 1948.

[88] A. Nagl, H. Überall, A. J. Haug, and G. Zarur, "Adiabatic mode theory of underwater sound propagation in a range-dependent environment," *The Journal of the Acoustical Society of America*, vol. 63, no. 3, pp. 739–749, 1978.

[89] R. B. Evans, "A coupled mode solution for acoustic propagation in a waveguide with stepwise depth variations of a penetrable bottom," *The Journal of the Acoustical Society of America*, vol. 74, no. 1, pp. 188–195, 1983.

[90] F. R. DiNapoli and R. L. Deavenport, "Theoretical and numerical green's function field solution in a plane multilayered medium," *The Journal of the Acoustical Society of America*, vol. 67, no. 1, pp. 92–105, 1980.

[91] H. Hardinr and D. Tappertf, "Application of the split-step fourier method to the numerical solution of nonlinear and variable coefficient wave equation," *Siam Rev*, vol. 15, p. 423, 1973.

[92] D. Lee and J. S. Papadkis, "Numerical solutions of underwater acoustic wave propagation problems." Naval Underwater Systems Center New London CT, Tech. Rep., 1979.

[93] V. Meyer and C. Audoly, "A comparison between experiments and simulation for shallow water short range acoustic propagation," in *ICSV 24th International Congress on Sound and Vibration*, Jul. 2017.

[94] J. T. Etgen and M. J. O'Brien, "Computational methods for large-scale 3D acoustic finite-difference modeling: A tutorial," *Geophysics*, vol. 72, no. 5, pp. 223–230, 2007.

[95] W. Liu, L. Zhang, W. Wang, Y. Wang, S. Ma, X. Cheng, and W. Xiao, "A three-dimensional finite difference model for ocean acoustic propagation and benchmarking for topographic effects," *The Journal of the Acoustical Society of America*, vol. 150, no. 2, pp. 1140–1156, 2021.

[96] M. S. Ballard, "Three-dimensional acoustic propagation under a rough sea surface," in *Proceedings of Meetings on Acoustics ICA2013*, vol. 19, no. 1. Acoustical Society of America, 2013.

[97] P. R. Williamson and R. G. Pratt, "A critical review of acoustic wave modeling procedures in 2.5 dimensions," *Geophysics*, vol. 60, no. 2, pp. 591–595, 1995.

[98] D. B. Reeder, L. Y. Chiu, and C. Chen, "Experimental evidence of horizontal refraction by nonlinear internal waves of elevation in shallow water in the south china sea: 3D versus Nx2D acoustic propagation modeling," *Journal of Computational Acoustics*, vol. 18, no. 03, pp. 267–278, 2010.

[99] H. Liu, Y. S. Ong, X. Shen, and J. Cai, "When Gaussian process meets big data: A review of scalable GPS," *IEEE transactions on neural networks and learning systems*, vol. 31, no. 11, pp. 4405–4423, 2020.

[100] K. Hornik, M. Stinchcombe, and H. White, "Multilayer feedforward networks are universal approximators," *Neural networks*, vol. 2, no. 5, pp. 359–366, 1989.

[101] O. Onasami, D. Adesina, and L. Qian, "Underwater acoustic communication channel modeling using deep learning," in *The 15th International Conference on Underwater Networks & Systems*, 2021, pp. 1–8.

[102] D. Caviedes-Nozal, N. A. Riis, F. M. Heuchel, J. Brunskog, P. Gerstoft, and E. Fernandez-Grande, "Gaussian processes for sound field reconstruction," *The Journal of the Acoustical Society of America*, vol. 149, no. 2, pp. 1107–1119, 2021.

[103] C. S. Ganesh, V. Jyothi, S. A. Barathwaj, and R. Azhagumurugan, "Machine learning based classification and modelling of underwater acoustic communication," in *OCEANS Chennai*. IEEE, 2022, pp. 1–7.

[104] H. Long, H. Chen, and T. Zhang, "Classification on underwater acoustic propagation model using convolutional neural network," in *International Conference on Signal Processing, Communications and Computing (ICSPCC)*. IEEE, 2021, pp. 1–6.

[105] A. B. R. Ahmed, M. Younis, and M. H. De Leon, "Machine learning based sound speed prediction for underwater networking applications," in *17th International Conference on Distributed Computing in Sensor Systems (DCOSS)*. IEEE, 2021, pp. 436–442.

[106] M. Liu, H. Niu, Z. Li, Y. Liu, and Q. Zhang, "Deep-learning geoacoustic inversion using multi-range vertical array data in shallow water," *The Journal of the Acoustical Society of America*, vol. 151, no. 3, pp. 2101–2116, 2022.

[107] Y. Shen, X. Pan, Z. Zheng, and P. Gerstoft, "Matched-field geoacoustic inversion based on radial basis function neural network," *The Journal of the Acoustical Society of America*, vol. 148, no. 5, pp. 3279–3290, 2020.

[108] L. Mao, X. Pan, and Y. Shen, "Geoacoustic inversion based on neural network," in *OCEANS 2021 San Diego–Porto*. IEEE, 2021, pp. 1–5.

[109] C. Frederick, S. Villar, and Z.-H. Michalopoulou, "Seabed classification using physics-based modeling and machine learning," *The Journal of the Acoustical Society of America*, vol. 148, no. 2, pp. 859–872, 2020.

[110] A. Karpatne, G. Atluri, J. H. Faghmous, M. Steinbach, A. Banerjee, A. Ganguly, S. Shekhar, N. Samatova, and V. Kumar, "Theory-guided data science: A new paradigm for scientific discovery from data," *IEEE Transactions on Knowledge and Data Engineering*, vol. 29, no. 10, p. 2318–2331, Oct 2017.

[111] P. Zhu, J. Isaacs, B. Fu, and S. Ferrari, "Deep learning feature extraction for target recognition and classification in underwater sonar images," in *56th annual conference on decision and control (CDC)*. IEEE, 2017, pp. 2724–2731.

[112] Y. Xu, Y. Zhang, H. Wang, and X. Liu, "Underwater image classification using deep convolutional neural networks and data augmentation," in *International conference on signal processing, communications and computing (ICSPCC)*. IEEE, 2017, pp. 1–5.

[113] H.-T. Nguyen, E.-H. Lee, and S. Lee, "Study on the classification performance of underwater sonar image classification based on convolutional neural networks for detecting a submerged human body," *Sensors*, vol. 20, no. 1, p. 94, 2019.

[114] N. Baker, F. Alexander, T. Bremer, A. Hagberg, Y. Kevrekidis, H. Najm, M. Parashar, A. Patra, J. Sethian, S. Wild *et al.*, "Workshop report on basic research needs for scientific machine learning: Core technologies for artificial intelligence," USDOE Office of Science, Washington, DC, Tech. Rep., 2019.

[115] M. Raissi and G. E. Karniadakis, "Hidden physics models: Machine learning of nonlinear partial differential equations," *Journal of Computational Physics*, vol. 357, pp. 125–141, 2018.

[116] L. P. Swiler, M. Gulian, A. L. Frankel, C. Safta, and J. D. Jakeman, "A survey of constrained Gaussian process regression: Approaches and implementation challenges," *Journal of Machine Learning for Modeling and Computing*, vol. 1, no. 2, pp. 119–156, 2020.

[117] J. Willard, X. Jia, S. Xu, M. Steinbach, and V. Kumar, "Integrating scientific knowledge with machine learning for engineering and environmental systems," 2021. [Online]. Available: https://arxiv.org/abs/2003.04919

[118] C. Rackauckas, Y. Ma, J. Martensen, C. Warner, K. Zubov, R. Supekar, D. Skinner, and A. J. Ramadhan, "Universal differential equations for scientific machine learning," *CoRR*, vol. abs/2001.04385, 2020.

[119] J. S. Read, X. Jia, J. Willard, A. P. Appling, J. A. Zwart, S. K. Oliver, A. Karpatne, G. J. Hansen, P. C. Hanson, W. Watkins *et al.*, "Process-guided deep learning predictions of lake water temperature," *Water Resources Research*, vol. 55, no. 11, pp. 9173–9190, 2019.

[120] J. Sun, Z. Niu, K. A. Innanen, J. Li, and D. O. Trad, "A theory-guided deep learning formulation of seismic waveform inversion," in *SEG Technical Program Expanded Abstracts.* Society of Exploration Geophysicists, 2019, pp. 2343–2347.

[121] M. Raissi, P. Perdikaris, and G. E. Karniadakis, "Physics-informed neural networks: A deep learning framework for solving forward and inverse problems involving nonlinear partial differential equations," *Journal of Computational Physics*, vol. 378, pp. 686–707, 2019.

[122] C. L. Pettit and D. K. Wilson, "A physics-informed neural network for sound propagation in the atmospheric boundary layer," in *Proceedings of Meetings on Acoustics*, vol. 42, no. 1. Acoustical Society of America, 2020.

[123] N. Borrel-Jensen, A. P. Engsig-Karup, and C.-H. Jeong, "Physics-informed neural networks for one-dimensional sound field predictions with parameterized sources and impedance boundaries," *Journal of the Acoustical Society of America*, vol. 1, no. 12, p. 122402, dec 2021.

[124] S. Alkhadhr, X. Liu, and M. Almekkawy, "Modeling of the forward wave propagation using physics-informed neural networks," in *2021 IEEE International Ultrasonics Symposium (IUS)*, 2021, pp. 1–4.

[125] B. Moseley, A. Markham, and T. Nissen-Meyer, "Solving the wave equation with physics-informed deep learning," 2020. [Online]. Available: https://arxiv.org/abs/2006.11894

[126] M. Rasht-Behesht, C. Huber, K. Shukla, and G. E. Karniadakis, "Physics-informed neural networks (PINNs) for wave propagation and full waveform inversions," *Journal of Geophysical Research: Solid Earth*, vol. 127, no. 5, 2021.

[127] T. de Wolff, H. Carrillo, L. Martí, and N. Sanchez-Pi, "Assessing physics informed neural networks in ocean modelling and climate change applications," in *AI: Modeling Oceans and Climate Change Workshop at ICLR*, 2021.

[128] T. de Wolff, H. Carrillo, L. Martí, and N. Sanchez-Pi, "Towards optimally weighted physics-informed neural networks in ocean modelling," 2021. [Online]. Available: https://arxiv.org/abs/2106.08747

[129] A. Sahoo, S. K. Dwivedy, and P. Robi, "Advancements in the field of autonomous underwater vehicle," *Ocean Engineering*, vol. 181, pp. 145–160, 2019.

[130] C. Cheng, Q. Sha, B. He, and G. Li, "Path planning and obstacle avoidance for AUV: A review," *Ocean Engineering*, vol. 235, no. 1, 2021.

[131] P. Yao and S. Qi, "Obstacle-avoiding path planning for multiple autonomous underwater vehicles with simultaneous arrival," *Science China Technological Sciences*, vol. 62, no. 1, pp. 121–132, 2019.

[132] F. Khorrami and P. Krishnamurthy, "A hierarchical path planning and obstacle avoidance system for an autonomous underwater vehicle," in *American Control Conference*. IEEE, 2009, pp. 3579–3584.

[133] M. P. Aghababa, "3D path planning for underwater vehicles using five evolutionary optimization algorithms avoiding static and energetic obstacles," *Applied Ocean Research*, vol. 38, pp. 48–62, 2012.

[134] Y. Wu, K. H. Low, and C. Lv, "Cooperative path planning for heterogeneous unmanned vehicles in a search-and-track mission aiming at an underwater target," *IEEE Transactions on Vehicular Technology*, vol. 69, no. 6, pp. 6782–6787, 2020.

[135] Y. Deng, P.-P. J. Beaujean, E. An, and E. A. Carlson, "A path planning control strategy for search-classify task using multiple cooperative underwater vehicles," in *OCEANS 2008*, 2008, pp. 1–9.

[136] D. Li, P. Wang, and L. Du, "Path planning technologies for autonomous underwater vehicles-a review," *Ieee Access*, vol. 7, pp. 9745–9768, 2018.

[137] M. Panda, B. Das, B. Subudhi, and B. B. Pati, "A comprehensive review of path planning algorithms for autonomous underwater vehicles," *International Journal of Automation and Computing*, vol. 17, no. 3, pp. 321–352, 2020.

[138] F. Jalal and F. Nasir, "Underwater navigation, localization and path planning for autonomous vehicles: A review," in *International Bhurban Conference on Applied Sciences and Technologies (IBCAST)*, 2021, pp. 817–828.

[139] N. K. Yilmaz, C. Evangelinos, N. M. Patrikalakis, P. F. Lermusiaux, P. J. Haley, W. G. Leslie, A. R. Robinson, D. Wang, and H. Schmidt, "Path planning methods for adaptive sampling of environmental and acoustical ocean fields," in *OCEANS 2006*. IEEE, 2006, pp. 1–6.

[140] C. Xiong, D. Chen, D. Lu, Z. Zeng, and L. Lian, "Path planning of multiple autonomous marine vehicles for adaptive sampling using voronoi-based ant colony optimization," *Robotics and Autonomous Systems*, vol. 115, pp. 90–103, 2019.

[141] R. Mishra, M. Chitre, and S. Swarup, "Informed sampling and adaptive monitoring using sparse Gaussian processes," in *IEEE/OES Autonomous Underwater Vehicle Workshop (AUV)*. IEEE, 2018, pp. 1–5.

[142] M. Chitre, "A holistic approach to underwater sensor network design," in *Proceedings of Naval Technology Seminar (NTS)*, vol. 2011, 2011.

[143] H. Schmidt and T. Schneider, "Acoustic communication and navigation in the new Arctic—A model case for environmental adaptation," in *IEEE third underwater communications and networking conference (UComms)*. IEEE, 2016, pp. 1–4.

[144] J.-H. Cho, J.-S. Kim, and S. Kim, "Benchmarking of optimal acoustic search path planning," in *The Nineteenth International Offshore and Polar Engineering Conference*. OnePetro, 2009.

[145] J. D. Hernández, E. Vidal, G. Vallicrosa, E. Galceran, and M. Carreras, "Online path planning for autonomous underwater vehicles in unknown environments," in *IEEE International Conference on Robotics and Automation (ICRA)*, 2015, pp. 1152–1157.

[146] J.-H. Li, H. Kang, G.-H. Park, and J.-H. Suh, "Real time path planning of underwater robots in unknown environment," in *International Conference on Control, Artificial Intelligence, Robotics Optimization (ICCAIRO)*, 2017, pp. 312–318.

[147] J. D. Hernández, E. Vidal, G. Vallicrosa, E. Galceran, and M. Carreras, "Online path planning for autonomous underwater vehicles in unknown environments," in *IEEE International Conference on Robotics and Automation (ICRA)*. IEEE, 2015, pp. 1152–1157.

[148] Z. Yan, J. Li, Y. Wu, and G. Zhang, "A real-time path planning algorithm for AUV in unknown underwater environment based on combining pso and waypoint guidance," *Sensors*, vol. 19, no. 1, p. 20, 2018.

[149] P. F. Lermusiaux, P. Malanotte-Rizzoli, D. Stammer, J. Carton, J. Cummings, and A. M. Moore, "Progress and prospects of us data assimilation in ocean research," *Oceanography*, vol. 19, no. 13, 2006.

[150] H. Schmidt and T. Schneider, "Acoustic communication and navigation in the new arctic — a model case for environmental adaptation," in *2016 IEEE Third Underwater Communications and Networking Conference (UComms)*, 2016, pp. 1–4.

[151] K. H. Low, J. Dolan, J. Schneider, and A. Elfes, "Multi-robot adaptive exploration and mapping for environmental sensing applications," *PhD thesis, CMU*, 2009.

[152] A. Krause, A. Singh, and C. Guestrin, "Near-optimal sensor placements in Gaussian processes: Theory, efficient algorithms and empirical studies." *Journal of Machine Learning Research*, vol. 9, no. 2, 2008.

[153] J. Zhang, M. Liu, S. Zhang, R. Zheng, and S. Dong, "Multi-AUV adaptive path planning and cooperative sampling for ocean scalar field estimation," *IEEE Transactions on Instrumentation and Measurement*, vol. 71, pp. 1–14, 2022.

[154] K. Li and M. Chitre, "Ocean acoustic propagation modeling using scientific machine learning," in *OCEANS: San Diego–Porto*. IEEE, 2021, pp. 1–5.

[155] K. Li and M. Chitre, "Data-aided underwater acoustic ray propagation modeling," 2022. [Online]. Available: https://arxiv.org/abs/2205.06066

[156] R. Hecht-Nielsen, "Theory of the backpropagation neural network," in *Neural networks for perception*. Elsevier, 1992, pp. 65–93.

[157] A. G. Baydin, B. A. Pearlmutter, A. A. Radul, and J. M. Siskind, "Automatic differentiation in machine learning: a survey," *Journal of Marchine Learning Research*, vol. 18, pp. 1–43, 2018.

[158] D. P. Kingma and J. Ba, "Adam: A method for stochastic optimization," in *3rd International Conference for Learning Representations*, 2015.

[159] M. Li, T. Zhang, Y. Chen, and A. J. Smola, "Efficient mini-batch training for stochastic optimization," in *Proceedings of the 20th ACM SIGKDD international conference on Knowledge discovery and data mining*, 2014, pp. 661–670.

[160] F. Fisher and V. Simmons, "Sound absorption in sea water," *The Journal of the Acoustical Society of America*, vol. 62, no. 3, pp. 558–564, 1977.

[161] J. B. Allen and D. A. Berkley, "Image method for efficiently simulating small-room acoustics," *The Journal of the Acoustical Society of America*, vol. 65, no. 4, pp. 943–950, 1979.

[162] J. M. Hovem, "Ray trace modeling of underwater sound propagation," in *Modeling and Measurement Methods for Acoustic Waves and for Acoustic Microdevices.* IntechOpen, 2013.

[163] M. Chitre and K. Li, "Physics-informed data-driven communication performance prediction for underwater vehicles," in *Underwater Communications and Networking Conference (UComms)*, 2022, pp. 1–5.

[164] K. Bruliński, A. Rudziński, and A. Stefani, "Characterization of ultrasonic communication channel in swimming pool," in *Signal Processing Symposium (SPSympo).* IEEE, 2019, pp. 167–172.

[165] J. Misiurewicz, K. Bruliński, W. Klembowski, and K. Kulpa, "Multipath propagation of acoustic signal in a swimming pool," in *Signal Processing Symposium (SPSympo).* IEEE, 2021, pp. 197–201.

[166] C. H. Harrison, "An approximate form of the rayleigh reflection loss and its phase: Application to reverberation calculation," *The journal of the acoustical society of America*, vol. 128, no. 1, pp. 50–57, 2010.

[167] T. RESON. Hydrophone TC4013 miniature reference hydrophone. Accessed 2022-06-10. [Online]. Available: https://www.m-b-t.com/fileadmin/redakteur/Ozeanographie/Hydrophone/Produktblaetter/TC4013.pdf

[168] K. Li and M. Chitre, "Physics-aided data-driven modal ocean acoustic propagation modeling," in *International Congress of Acoustics*, 2022.

[169] W. Miller, "The technique of variable separation for partial differential equations," in *Nonlinear Phenomena.* Springer Berlin Heidelberg, 1983, pp. 184–208.

[170] R. B. Guenther and J. W. Lee, "Preliminaries," in *Sturm-Liouville Problems: Theory and Numerical Implementation.* CRC Press, 2018.

[171] A. K. Ghatak, R. Gallawa, and I. Goyal, "Modified airy function and wkb solutions to the wave equation," *NASA STI/Recon Technical Report N*, vol. 92, 1991.

[172] B. J. DeCourcy and T. F. Duda, "A coupled mode model for omnidirectional three-dimensional underwater sound propagation," *The Journal of the Acoustical Society of America*, vol. 148, no. 1, pp. 51–62, 2020.

[173] G. Athanassoulis, K. Belibassakis, D. Mitsoudis, N. Kampanis, and V. Dougalis, "Coupled mode and finite element approximations of underwater sound propagation problems in general stratified environments," *Journal of Computational Acoustics*, vol. 16, no. 01, pp. 83–116, 2008.

[174] O. Glowacki, M. Moskalik, and A. Prominska, "Simulation of the sound propagation in an arctic fjord: general patterns and variability," in *Arctic Science Summit Week, Marine Processes and Variability*, 2013.

[175] O. Glowacki, G. B. Deane, M. Moskalik, P. Blondel, J. Tegowski, and M. Blaszczyk, "Underwater acoustic signatures of glacier calving," *Geophysical Research Letters*, vol. 42, no. 3, pp. 804–812, 2015.

[176] O. Głowacki, G. B. Deane, M. Moskalik, J. Tęgowski, and P. Blondel, "Two-element acoustic array gives insight into ice-ocean interactions in hornsund fjord, spitsbergen," *Polish Polar Research*, pp. 355–367, 2015.

[177] O. Glowacki, M. Moskalik, and G. B. Deane, "The impact of glacier meltwater on the underwater noise field in a glacial bay," *Journal of Geophysical Research: Oceans*, vol. 121, no. 12, pp. 8455–8470, 2016.

[178] Acousticstoolbox.jl. https://github.com/org-arl/AcousticsToolbox.jl. Accessed: 2022-06-12.